South Asian monsoon induced weathering and erosion inputs into the Bay of Bengal during the Miocene – Evidence from clay radiogenic isotope compositions

Dissertation

zur Erlangung des Doktorgrades
Dr. rer. nat.

der Mathematisch-Naturwissenschaftlichen Fakultät der
Christian-Albrechts-Universität zu Kiel

vorgelegt von
Lisa Bretschneider

Kiel, 2020

Erster Gutachter:	Prof. Dr. Martin Frank
Zweiter Gutachter:	Dr. Germain Bayon

Tag der mündlichen Prüfung: 17. Dezember 2020

Erklärung

Hiermit erkläre ich des Eides statt, dass ich die vorliegende Abhandlung, abgesehen von der Beratung durch meine Betreuer, nach Inhalt und Form selbstständig erarbeitet habe und keine anderen als die von mir aufgeführten Quellen und Hilfsmittel verwendet wurden.

Diese Arbeit ist unter Einhaltung der Regeln guter wissenschaftlicher Praxis der Deutschen Forschungsgemeinschaft entstanden und wurde weder in Auszügen noch in ganzer Form an einer anderen Stelle im Rahmen eines Prüfungsverfahrens eingereicht.

Teile dieser Arbeit wurden zur Veröffentlichung in einer Fachzeitschrift eingereicht oder sind in Vorbereitung eingereicht zu werden.

Es wurde kein akademischer Grad entzogen.

Kiel, 29. Oktober 2020

Lisa Bretschneider

Abstract

The South Asian monsoon (SAM) is a major component of the global climate system and influences the lives of more than a billion people. Despite its importance, it remains difficult to predict. Thus, it is crucial to understand how the monsoon behaved in the past under different boundary conditions such as a warmer world with reduced continental ice cover as we may experience in the near future and to apply this knowledge for the improvement of future projections. Furthermore, feedbacks which operate between the various forcing mechanisms of the monsoon, such as tectonics and climate as well as the associated changes in weathering and erosion regimes in the catchment areas of the SAM, need to be better understood on tectonic to orbital timescales.

To disentangle these different controls, geochemical records for International Ocean Discovery Program Site U1443 in the southern Bay of Bengal were produced that cover the middle to late Miocene (15.8-5 Ma). Radiogenic strontium, neodymium, hafnium and lead isotope compositions of detrital clays are used to infer changes in the provenance of the sediments supplied to the Ninetyeast Ridge and the prevailing weathering regime in the catchment of the Bay of Bengal. The study of orbital-resolution intervals of the middle Miocene (15.8-9.5 Ma) as well as of a 100 kyr resolution record of the late Miocene (9-5 Ma) allow tectonic and climatic forcing of changes recorded in the detrital clay radiogenic isotope record to be distinguished based on timing. The individual contributions from different erosional sources overall remained remarkably constant during the middle to late Miocene, despite major tectonic reorganizations in the Himalayas. The major contributing lithologies were the High Himalayan Crystalline, the Tethyan Sedimentary Series and the Indo-Burman Ranges. However, on orbital timescales, the high-resolution data from the five middle Miocene intervals show marked fluctuations of the radiogenic Sr, Nd and Pb isotope systems. Interestingly, their variability decreased markedly at 13.5 Ma right after the middle Miocene global cooling step. This change is attributed to a major restriction on the supply of High Himalayan erosion products due to climatically-induced migration of the peak precipitation area towards the frontal domains of the Himalayas and the Indo-Burman Ranges. These transient orbital-scale fluctuations of the radiogenic isotope signals were mainly triggered by climatically-driven changes in the balance of source contributions. The presence of a significant 30 kyr periodicity in the Nd isotope record, a common heterodyne associated with monsoon variability, suggests that changes of the location of peak monsoon precipitation between higher and lower elevations influencing weathering regimes on land exerted a major control on those short-term fluctuations.

At 7.3 Ma, Nd and Pb isotope compositions indicate a switch in provenance of the clays transported to the Ninetyeast Ridge. Contributions from the Irrawaddy River became more dominant while Himalayan contributions supplied by the Ganges and Brahmaputra Rivers decreased. This change

happened at the same time as the decline in global benthic $\delta^{13}C$ which was associated with the expansion of grasslands on land. Global cooling as well as increasing aridity likely resulted in a shift of the areas of highest precipitation to the Indo-Burman Ranges. An increase in Sr isotope compositions between 6 and 5 Ma was decoupled from Nd and Pb isotope signatures and likely indicates enhanced chemical weathering intensities in the catchments of the Ganges-Brahmaputra and Irrawaddy Rivers. A possible mechanism responsible for increased chemical weathering may have been the expansion of grassland which generated thick, easily weatherable soils as well as increased exposure of continental shelves due to a lowered sea level. The contemporaneous major late Miocene increase in seawater Sr isotope compositions may also have been affected by this change in detrital Sr isotope signatures of the Himalayan riverine inputs.

To better disentangle the silicate weathering intensity signal from changes in source provenance, coupled Nd and Hf isotope compositions across the whole middle to late Miocene were used to infer changes in silicate weathering intensities. Deviations of the Hf isotope compositions from the array defined by global clays ($\Delta\varepsilon_{Hf\ clay}$) exhibited some of the highest values measured to date suggesting the prevalence of extreme chemical weathering intensity under tropical warm and wet climate conditions during the Miocene. Authigenic clays incorporated highly radiogenic Hf from weathering solutions that obtained their signatures through the dissolution of labile mineral phases carrying those radiogenic Hf signatures. The extremely high $\Delta\varepsilon_{Hf\ clay}$ values were likely generated by a combination of highly weathered sediments and substantial erosion in tropical environments with intense seasonal precipitation, as is the case for seasonal monsoon rains on the floodplains surrounding the Bay of Bengal. The Hf isotope evolution shows a decrease towards the late Miocene, which likely was as a response to global cooling and aridification by decreasing monsoon seasonality and/or intensified erosion due to associated grassland expansion. Strong erosion may have prevented the formation of these very old and extremely weathered surfaces, which were likely a prerequisite for the occurrence of exceptionally high $\Delta\varepsilon_{Hf\ clay}$ values.

Kurzfassung

Der indische oder südasiatische Monsun ist ein wichtiger Bestandteil des globalen Klimasystems und beeinflusst das Leben von über einer Milliarde Menschen. Trotz seiner Bedeutung ist der Monsun noch immer schwer vorherzusagen. Daher ist es wichtig zu verstehen, wie sich der Monsun unter anderen Rahmenbedingungen in der Vergangenheit verhalten hat, wie zum Beispiel in einer wärmeren Welt mit geringerer kontinentaler Eisbedeckung. Dieses Szenario wird uns in naher Zukunft bevorstehen und die Erkenntnisse über die Vergangenheit werden der Verbesserung zukünftiger Vorhersagen dienen. Darüber hinaus müssen Rückkopplungssysteme der verschiedenen Antriebsmechanismen des Monsuns wie Tektonik und Klima sowie die damit verbundenen Änderungen des Verwitterungs- und Erosionsregimes der Monsun-Einzugsgebiete auf tektonischen bis orbitalen Zeitskalen besser verstanden werden.

Um die Einflüsse der verschiedenen Kontrollmechanismen zu entwirren, wurde ein geochemischer Datensatz für International Ocean Discovery Program Site U1443 im südlichen Golf von Bengalen erzeugt, der das mittlere bis späte Miozän (15.8 bis 5 Millionen Jahre vor heute (Ma)) umfasst. Radiogene Strontium-, Neodym-, Hafnium- und Blei-Isotopenzusammensetzungen der detritischen Tonfraktion wurden analysiert um die Herkunft der Sedimente, die zum Ninetyeast-Rücken geliefert wurden, und das vorherrschende Verwitterungsregime im Einzugsgebiet des Golfs von Bengalen zu bestimmen. Die Untersuchung von Zeitintervallen des mittleren Miozäns (15.8-9.5 Ma) in orbitaler Auflösung sowie eines Datensatzes mit niedrigerer 100.000-jähriger Auflösung des späten Miozäns (9-5 Ma) ermöglichte die Unterscheidung zwischen tektonischen und klimatischen Ursachen von Änderungen der radiogenen Isotopensignaturen der detritischen Tonfraktion. Trotz großer tektonischer Veränderungen im Himalaya blieben die Beiträge der verschiedenen Erosionsquellen im mittleren bis späten Miozän insgesamt erstaunlich konstant. Die wichtigsten Herkunftslithologien setzten sich aus dem High Himalayan Crystalline, der Tethyan Sedimentary Series und den Indo-Burman Ranges zusammen. Auf orbitaler Zeitskala zeigen die hochauflösenden Daten der fünf Intervalle aus dem mittleren Miozän jedoch deutliche Schwankungen der Sr-, Nd- und Pb-Isotopensysteme. Interessanterweise nahm deren Variabilität unmittelbar nach der globalen Abkühlung des mittleren Miozäns vor 13.5 Millionen Jahren deutlich ab. Diese Veränderung wird auf eine erhebliche Einschränkung der Lieferung von Erosionsprodukten des hohen Himalayas zurückgeführt, die durch die klimatisch bedingte Migration des Hauptniederschlagsgebiets in Richtung der südlichen Ränder des Himalayas und der Indo-Burman Ranges mit den höchsten Erhebungsgradienten ausgelöst wurde. Diese vorübergehenden Schwankungen der radiogenen Isotopensignale wurden hauptsächlich durch klimatisch verursachte Veränderungen in der Bilanz der Anteile der Herkunftslithologien ausgelöst. Signifikante 30.000-Jahres-Periodizitäten im Nd-Isotopendatensatz, die typischerweise mit der

Monsunvariabilität in Zusammenhang gebracht werden, legen nahe, dass Änderungen der Höhenlage der Lokationen der Hauptmonsunniederläge in den Himalayas und damit des Verwitterungsregimes an Land ein Hauptgrund für die kurzzeitigen Schwankungen waren.

Vor 7.3 Millionen Jahren zeigen Nd- und Pb-Isotopenzusammensetzungen einen Wechsel der Herkunft der zum Ninetyeast-Rücken transportierten Tone an. Die relativen Beiträge des Irrawaddy-Flusses stiegen, während die Beiträge aus den Himalayas, die durch den Ganges und Brahmaputra geliefert wurden, zurückgingen. Diese Änderung erfolgte zeitgleich mit der globalen Erniedrigung des benthischen $\delta^{13}C$-Signals, das mit der Ausbreitung von Gräsern an Land zusammenhing. Die globale Abkühlung sowie die zunehmende Trockenheit führten vermutlich zu einer Verschiebung der Hauptniederschlagsgebiete in die Indo-Burman Ranges. Ein Anstieg der Sr-Isotopenzusammensetzung zwischen 6 und 5 Millionen Jahren vor heute war entkoppelt von Nd- und Pb-Isotopensignaturen und deutet vermutlich auf verstärkte chemische Verwitterungsintensitäten in den Einzugsgebieten der Ganges-Brahmaputra und Irrawaddy Flusssysteme hin. Ein möglicher Mechanismus für eine erhöhte chemische Verwitterung könnte die Ausdehnung von Grasland gewesen sein, das mächtige, leicht verwitterbare Böden erzeugt hat und von einer erhöhten Exposition des Kontinentalschelfs aufgrund eines niedrigeren Meeresspiegels begleitet wurde. Der zeitgleiche starke Anstieg der Sr-Isotopenzusammensetzung des Meerwassers im späten Miozän könnte durch diese Änderung der detritischen Sr-Isotopensignaturen der Himalaya-Flusseinträge mit verursacht worden sein.

Um Signale der Verwitterungsintensität besser von Änderungen der Sedimentherkunft des detritischen Tonmaterials zu unterscheiden, wurden Nd- und Hf-Isotopenzusammensetzungen kombiniert. Dies wurde genutzt, um Änderungen der Verwitterungsintensität im Einzugsgebiet des Golf von Bengalen zu rekonstruieren. Abweichungen der Hf-Isotopenzusammensetzungen von dem durch globale Tone definierten Datenfeld ($\Delta\varepsilon_{Hf\ clay}$) zeigen einige der höchsten bisher gemessenen Werte, was auf extreme chemische Verwitterungsintensitäten unter tropisch warmen und feuchten Klimabedingungen hinweist. Authigene Tone bauten hochradiogenes Hf aus den Verwitterungslösungen ein, das durch die Auflösung sehr labiler Mineralphasen mit radiogenen Hf-Signaturen freigesetzt wurde. Die extrem hohen $\Delta\varepsilon_{Hf\ clay}$-Werte wurden wahrscheinlich durch eine Kombination aus stark verwitterten Sedimenten und erheblicher Erosion in tropischem Milieu mit intensiven und saisonalen Niederschlägen (hier der saisonale Monsunregen) erzeugt. Die Entwicklung der Hf-Isotopenzusammensetzung zeigt eine Abnahme im späten Miozän, die wahrscheinlich als Reaktion auf die globale Abkühlung und zunehmende Trockenheit durch die Abnahme der Monsun-Saisonalität und/oder verstärkter Erosion aufgrund der damit verbundenen Graslandausdehnung resultierte. Es wird angenommen, dass verstärkte Erosion die Bildung dieser sehr alten und extrem verwitterten Oberflächen, die eine Voraussetzung für die außergewöhnlich hohen $\Delta\varepsilon_{Hf\ clay}$-Werte waren, im späten Miozän wahrscheinlich zunehmend verhindert hat.

Contents

1. Introduction

1.1 Motivation and Objectives

The South Asian monsoon (SAM) is a major component of the global climate system and influences the lives of more than a billion people, regionally affecting most or all parts of the present-day territories of India, Pakistan, Sri Lanka, Bangladesh, Bhutan, Nepal, Myanmar, Laos, Thailand and parts of China. It is a major factor in the South Asian economy (e.g., Barker et al., 1985), providing vital water resources and being essential for agriculture as well as hydroelectric power generation and industrial development (Turner and Annamalai, 2012), but also putting people, infrastructure and crops in jeopardy through flooding. The South Asian monsoon is characterized by the seasonal reversal of surface winds and associated precipitation leading to rainy summer and dry winter seasons in most places (Fig. 1.1; e.g., Wang et al., 2017). On a very basic level and already described by Halley in 1686, this is caused by differential heating of the continental land mass and the adjacent ocean as a consequence of differences in heat capacity. Heating of the Asian continent during boreal summer forms a low-pressure zone over Tibet creating a N-S pressure gradient which results in cross-equatorial air mass transport (Turner and Annamalai, 2012). Summer monsoon winds from the southwest bring moisture originating from warm waters of the tropical Indian Ocean to the continent resulting in the rainy summer monsoon. Today, nearly 80 % of India's total annual rainfall is received during the summer monsoon season from June to September (Gupta et al., 2015; Turner and Annamalai, 2012).

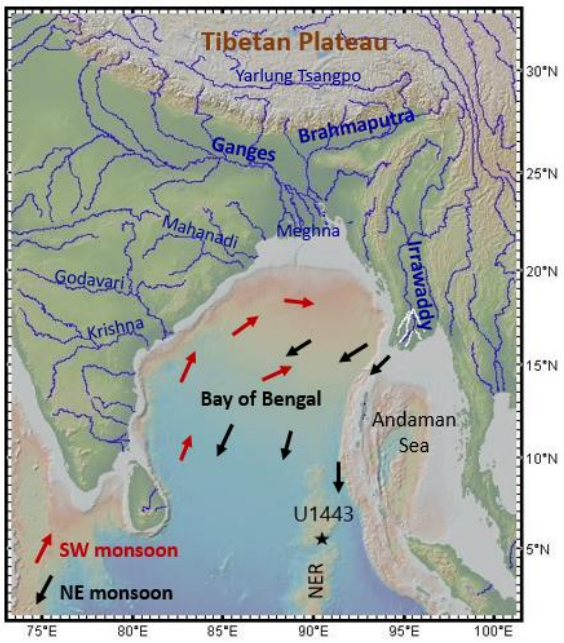

Fig. 1.1: Map of the Bay of Bengal with marked Site U1443 and major river systems supplying sediments to the bay. The arrows represent the main wind directions during summer (SW, red) and winter (NE, black) monsoons.

Despite its importance, the SAM remains difficult to predict. In order to improve coupled ocean-atmosphere general circulation models, it is thus crucial to understand how the monsoon behaves under different boundary conditions such as a warmer world with reduced continental ice cover that we will likely experience in the near future. To constrain monsoon behavior in a warmer than modern world we have to look into periods of time in the geological past when temperatures were higher than today. The Miocene epoch (23.03-5.33 Ma) is a geologically recent period that was characterized by warmer than present temperatures and pronounced global climatic changes (Fig. 1.2). The Miocene Climatic Optimum (~17 to 15 Ma) was a warm period with global annual mean temperatures ~3°C higher than today, based on proxy data constraining land and sea surface temperatures (You et al., 2009). The Miocene Climatic Optimum was followed by a stepwise cooling trend that led to development of a permanent Antarctic ice-sheet after 13.9 Ma (e.g., Holbourn et al., 2005) associated with a marked decrease in atmospheric CO_2 (Foster et al., 2012).

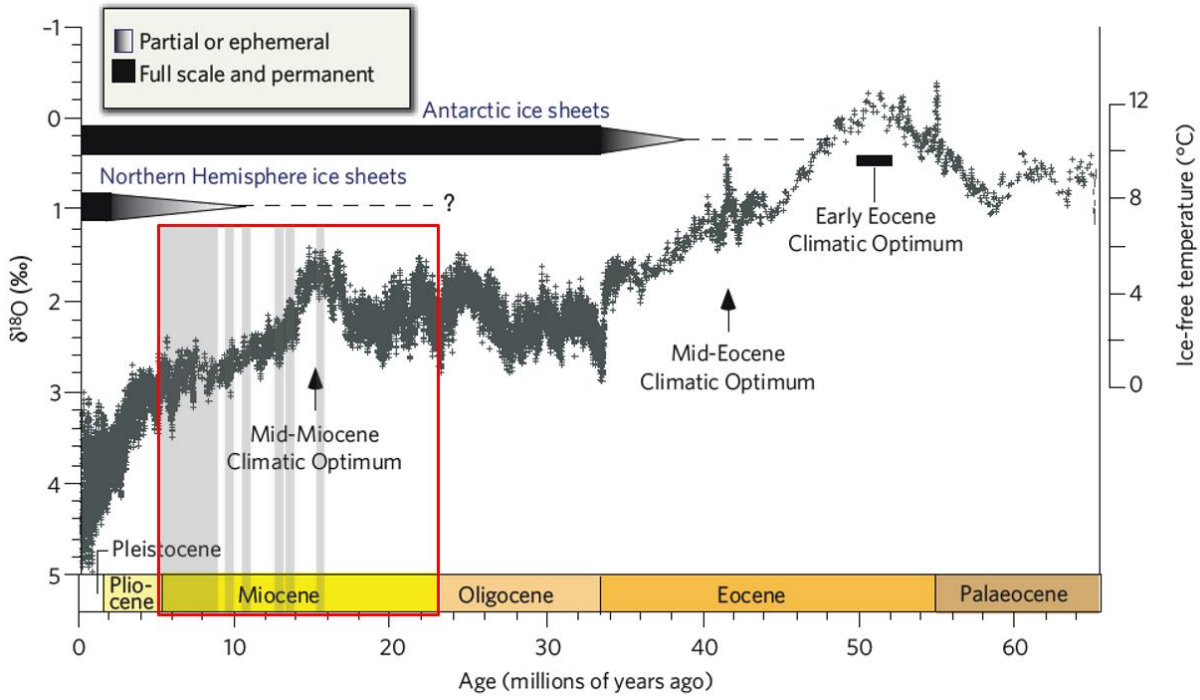

Fig. 1.2: Cenozoic benthic $\delta^{18}O$ evolution representing temperature and global ice volume over the last 65 Myr. The Miocene epoch is marked by the red frame and the grey bars within represent the intervals investigated in this thesis (modified from Zachos et al., 2008).

Apart from its warm temperatures, the Miocene is also particularly interesting because the SAM has been considered to have initiated or intensified during this period, the exact timing, however, still being debated. Some records (e.g., Arabian Sea upwelling) indicate that an initial intensification occurred at ~7-8 Ma whereas others (e.g., Loess deposits) suggest that this intensification occurred at least as early as ~22 Ma or even earlier (Clift et al., 2008; Licht et al., 2014; Wang et al., 2005). The uplift of the Himalayan-Tibetan Plateau is considered an important prerequisite for the development of the Asian monsoon system (e.g., Prell and Kutzbach, 1992)

given that those high elevations (>4.5 km above sea level) must have considerably influenced atmospheric circulation patterns (e.g., Hahn and Manabe, 1975; Huber and Goldner, 2012; Molnar et al., 1993; Ruddiman and Kutzbach, 1989). A higher and wider Himalayan-Tibetan plateau provided a heat source at mid-latitudes, likely increasing sensible and latent heat fluxes driving summer monsoon circulation (Molnar et al., 1993). Therefore, the uplift history of the Himalayan orogen has been suggested to be closely linked to the development of the SAM (e.g., Clift et al., 2008; Molnar et al., 1993).

Erosion intensity, for example, increases with the amount of precipitation, which is also influenced by temperature and the degree of evaporation and how much water is present in the atmosphere. Precipitation, in turn, strongly influences relief and exhumation rates (Deng et al., 2019; Kutzbach et al., 1989). Furthermore, Raymo (1994) proposed that increased silicate weathering, as well as organic carbon burial, promoted CO_2 drawdown and may have led to the global cooling of the middle Miocene. Hence, monsoon intensity, global climate, tectonic changes, weathering and erosion are closely intertwined and understanding the different feedback mechanisms controlling the various factors is therefore crucial to make reliable predictions. Both external (orbital insolation) and internal (boundary conditions such as ice volume, atmospheric greenhouse gases and topography) forcing factors play a significant role in controlling the SAM (e.g., Clemens and Prell, 2007; Ruddiman, 2006). Records extending over orbital to tectonic timescales, particularly over warmer than present intervals of Earth's history, are fundamental to evaluate the factors controlling the evolution of the monsoon. While the East Asian monsoon evolution has been studied at orbital resolution in the South China Sea (e.g., Holbourn et al., 2010; Steinke et al., 2010), the available records of the South Asian monsoon do not date back thus far in the geological past or have been of insufficient time resolution to investigate the relationship between climatic changes and the SAM throughout the Miocene. The new continuous cores from Site U1443 in the Bay of Bengal now provide such a rare high-resolution sediment archive dating back to the Oligocene and thus allow reconstructing long-term monsoonal circulation changes. The Bay of Bengal receives one of the largest freshwater and sediment discharges in the world from large Ganges-Brahmaputra and Irrawaddy river systems, which are primarily influenced by the SAM. It is therefore a key location to monitor past monsoonal trends in relation to changes in insolation forcing and in boundary conditions such as orography, global ice volume and greenhouse gas concentrations (Kuhnt et al., 2020).

1.2 Reconstructing past monsoon intensity

To reconstruct past changes in monsoon circulation, well-understood proxies from geological archives are necessary. Monsoon proxies are usually separated into two groups – proxies related to monsoon winds and those associated with monsoon induced precipitation (Wang et al., 2005).

Wind-based proxies include for example eolian dust records representing wind strength (e.g., Clemens and Prell, 1990) and planktic foraminiferal abundances indicative of monsoon-induced upwelling (e.g., Kroon et al., 1991; Prell and Kutzbach, 1992). Precipitation-based proxies are directly linked to the monsoon via hydrological pathways. One example are paired Mg/Ca and planktic $\delta^{18}O$, which can be used to infer sea surface salinity and thus river runoff (e.g., Gebregiorgis et al., 2018). The Bay of Bengal is a core region of the SAM where rainfall is the dominant factor defining monsoon intensity. Moreover, it is crucial to understand how precipitation through the SAM affected the development of orogens through enhanced erosion (Burbank et al., 2003; Clift et al., 2008; Clift et al., 2014). Thus, well-dated proxy records of precipitation and terrigenous runoff are essential to reconstruct SAM evolution (Kuhnt et al., 2020).

One approach to reconstruct monsoon intensity is the investigation of environmental changes on the continent. Changing flora and fauna as well as weathering regimes have been closely linked to climate and monsoon precipitation (Clift et al., 2014). However, the investigation of chemical weathering as a response to past climate is challenging because continuous, well-dated records of past continental weathering are difficult to find. Information about the evolution of continental weathering is, however, archived in marine sedimentary records. In the SAM domain, weathered and eroded sediments from the mountain belts surrounding the Bay of Bengal have been transported from the continent to the bay via rivers and accumulated in deltas and on submarine fans. Many studies used sediment records from the Bengal Fan, which cover the past 17 Ma (e.g., Derry and France-Lanord, 1996; Galy et al., 1996; Galy et al., 2010) and found remarkably stable sediment provenance throughout the middle to late Miocene. The ages of the sediments, were, however not well constrained and the turbiditic nature of these records often resulted in incomplete time series. Therefore, we investigated a record recovered from the crest of the Ninetyeast Ridge, which experienced a slow and continuous hemipelagic sedimentation reaching back to the Oligocene. We used the radiogenic isotope compositions of detrital clays from the Ninetyeast Ridge to infer changes in the sediment source and weathering regime across key intervals of the Miocene. Focusing on the detrital clay size minimized mineral sorting effects, which may occur during transport. Grain size effects on sedimentary radiogenic isotope compositions are typically ascribed to hydrodynamic sorting of distinct size fractions composed of different mineral phases (Tütken et al., 2002).

The continental lithologies surrounding the Bay of Bengal constrain the possible endmembers for the mixture of sediment deposited at Site U1443 on the Ninetyeast Ridge. Sr, Hf and Pb isotope compositions are additionally influenced by fractionation during weathering and transport due to the large range in the isotope composition of different mineral phases and differences in their resistance to weathering (Ali et al., 2015; Blum et al., 1993; Tütken et al., 2002). These isotopic signals thus provide information on prevailing weathering regimes in the past.

1.3 Radiogenic isotope systematics of terrestrial rocks

Radiogenic isotopes are produced by the radioactive decay of parent isotopes. Varying radiogenic isotope signatures of rocks are thus a consequence of the ratios of abundances of parent and daughter elements over time due to the ingrowth caused by the decay of the parent isotope. During the differentiation of the Earth's crust from the mantle and the formation of silicate rocks from magma and partial melts, parent and daughter isotopes are fractionated according to their ability to substitute for a major element in the mineral lattice, also known as their compatibility. This results in different element ratios for mantle and continental crust derived rocks, which has consequences for the amount of ingrowth of the radiogenic daughter isotopes. Hence, the radiogenic isotope compositions of rocks are a function of rock type (chemical differentiation) and their age (radioactive decay) leading to significant isotopic variations. This in turn can be used to trace geochemical processes including continental erosion and weathering as well as oceanic water mass mixing.

The radiogenic neodymium (Nd) isotope ^{143}Nd is produced by the radioactive decay of the samarium (Sm) isotope ^{147}Sm with a half-live of 106 Gyr (Lugmair and Marti, 1978) and commonly normalized to the primordial ^{144}Nd. Sm and Nd are both rare earth elements and behave chemically similar. Nevertheless, during partial melting Sm behaves slightly more compatible than Nd and stays preferentially in the residual mantle leading to higher Sm/Nd ratios and thus higher ^{143}Nd/^{144}Nd in the mantle compared to the continental crust (Fig. 1.3; DePaolo and Wasserburg, 1976). The ^{143}Nd abundances in rocks vary as a function of age and Sm/Nd ratio of the rock. The differences between the ^{143}Nd/^{144}Nd ratios are small and are thus expressed using the dimension-free ε-notation

$$\varepsilon_{Nd} = \left(\frac{(^{143}Nd/^{144}Nd)_{sample}}{(^{143}Nd/^{144}Nd)_{CHUR}} - 1 \right) \times 10^4$$

where CHUR refers to the chondritic uniform reservoir, which reflects the Nd isotope evolution from a uniform reservoir with a Sm/Nd ratio equal to that of chondritic meteorites and therefore represents a hypothetical isotopic evolution of the Earth without fractionation processes. The present-day ^{143}Nd/^{144}Nd$_{CHUR}$ value is 0.512638 (Jacobsen and Wasserburg, 1980).

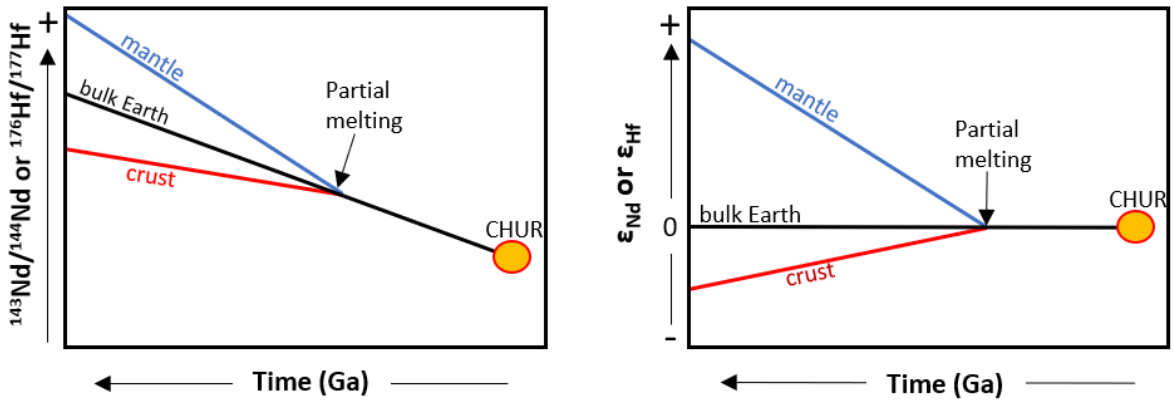

Fig. 1.3: Schematic evolution of Nd and Hf isotope compositions of the Chondritic Uniform Reservoir (CHUR) over time and within the Earth's mantle and crust after partial melting.

The stable, radiogenic hafnium (Hf) isotope ^{176}Hf is produced by β-decay of the radioactive lutetium (Lu) isotope ^{176}Lu with a half-life of 37.3 Gyr (Nir-El and Lavi, 1998; Scherer et al., 2001), causing variations in the $^{176}Hf/^{177}Hf$ ratio between different rocks due to radiogenic ingrowth. The primordial isotope used for normalization is ^{177}Hf. Analogous to Nd, variations in $^{176}Hf/^{177}Hf$ are expressed in the ε-notation (Goldstein and Jacobsen, 1987)

$$\varepsilon_{Hf} = \left(\frac{(^{176}Hf/^{177}Hf)_{sample}}{(^{176}Hf/^{177}Hf)_{CHUR}} - 1 \right) \times 10^4$$

with a modern CHUR value of 0.282785 (Bouvier et al., 2008). Like Sm and Nd, Lu is a rare earth element, while Hf belongs to the group of high field strength elements. Similar to Sm-Nd, the daughter isotope Hf accumulates in the melt fraction, while Lu preferentially stays in the residuum resulting in lower $^{176}Hf/^{177}Hf$ ratios in the Earth's crust than in the mantle (Fig. 1.3). Due to their similar behavior, Nd and Hf isotope compositions of most terrestrial rocks exhibit a strong positive correlation, which has been described as the "terrestrial array" (Vervoort et al., 1999). Rocks of the continental crust (especially old cratons) are characterized by generally unradiogenic Nd and Hf isotope compositions (low ε_{Nd} and ε_{Hf}) while young volcanic rocks of mantle origin (e.g., ocean island basalts or mid ocean ridge basalts) exhibit radiogenic (high ε_{Nd} and ε_{Hf}) isotope compositions.

The radiogenic strontium (Sr) isotope ^{87}Sr is the product of the radioactive decay of rubidium (Rb) isotope ^{87}Rb (half-life of 48.8 Gyr; Blum and Erel, 2003; Steiger and Jäger, 1977). The abundance of ^{87}Sr is commonly normalized to the primordial ^{86}Sr. During partial melting, the highly incompatible Rb is preferentially incorporated into the magmatic melt instead of staying in the mantle. This results in low Rb/Sr ratios in the mantle and high ratios in the continental crust (Fig. 1.4), which is opposite to Sm-Nd and Lu-Hf isotope systematics. Consequently, this produces young mantle-derived rocks with low $^{87}Sr/^{86}Sr$ and old continental rocks with high $^{87}Sr/^{86}Sr$. The trace elements rubidium and strontium are geochemically similar to the major elements potassium

and calcium, respectively. Minerals with high K/Ca ratios thus produce high $^{87}Sr/^{86}Sr$ ratios over time.

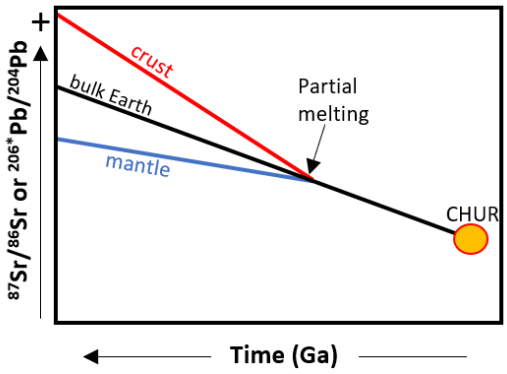

Fig. 1.4: Schematic evolution of Sr and Pb isotope compositions of the Chondritic Uniform Reservoir (CHUR) over time and within the Earth's mantle and crust after partial melting. *The $^{206}Pb/^{204}Pb$ isotope ratio is one example, but it also applies for $^{207}Pb/^{204}Pb$ and $^{208}Pb/^{204}Pb$.

Lead has three radiogenic isotopes, ^{206}Pb, ^{207}Pb, and ^{208}Pb, which are the stable end products of the decay series of uranium and thorium with the parent isotopes ^{238}U, ^{235}U and ^{232}Th (half-lives are 4.47 Gyr, 0.704 Gyr, and 14 Gyr, respectively; Steiger and Jäger, 1977). The abundances of the radiogenic Pb isotopes are normalized to primordial ^{204}Pb or are expressed as ratios amongst each other. U and Th behave geochemically similarly and during partial melting in that they preferentially migrate into the melt, resulting in an enrichment of U and Th of the continental crust compared to the mantle (Fig. 1.4). This explains higher abundances of radiogenic Pb isotopes in the continental crust while mantle-derived rocks are represented by unradiogenic Pb isotope compositions similar to Rb-Sr systematics.

1.4 Radiogenic isotopes as tracers of continental weathering

The geochemical processes in the Earth's interior form rocks with distinct isotope compositions depending mainly on the fractionation between parent and daughter elements and the time of melt extraction. When the rocks are exposed to weathering processes, particles with distinct radiogenic isotope signatures are released. Therefore, their isotope compositions can be used to reconstruct the provenance of the weathered and eroded material. At the same time, the minerals are dissolved according to their chemical resistance during weathering. This can lead to differences between the isotope compositions of the host rocks and the weathering fluids, which are incorporated for example into secondary clay minerals.

In the case of the Sm/Nd system, parent and daughter isotopes are chemically very similar which generally results in only very small variations of Sm/Nd ratios between the different minerals and between source rocks and weathered material and weathering solutions. Their weathering is thus overall considered congruent. Exceptions have, however, been found in glacially dominated regions

(e.g., Hindshaw et al., 2018). In contrast, Sr, Hf and Pb isotope compositions exhibit large variations between the different minerals of the rocks, which also differ in their resistance to weathering (Blum et al., 1993; Tütken et al., 2002). This is called incongruent weathering and these isotope systems are thus sensitive to changes in weathering regimes of the past.

The combination of Lu-Hf and Sm-Nd isotope systems has successfully been used to trace silicate weathering. In contrast to Sm and Nd, Lu and Hf are partitioned differently into mineral phases which results in highly variable Lu/Hf ratios of the different minerals. This decoupling between the Lu-Hf and Sm-Nd systems at mineral scale enables the tracing of silicate weathering intensity because different mineral phases with distinct resistance to weathering are affected differently (Bayon et al., 2009b). Zircons play a fundamental role in the Lu-Hf isotope systematics, because a large proportion of Hf in crustal rocks is contained in zircons, which therefore exhibit low Lu/Hf ratios, i.e. highly unradiogenic Hf isotope compositions. Zircons are extremely resistant to weathering and preferentially accumulate in the coarse-grained fractions of sediments during transport processes (Patchett et al., 1984). This "zircon effect" (Van de Flierdt et al., 2007; White et al., 1986) leads to a significant decoupling between Hf and Nd. If sediments contain large amounts of zircons, their extremely unradiogenic Hf isotope signatures will dominate the Hf isotope composition of the coarse grained detrital sediment fraction. The zircon effect is likely also the main reason for the more radiogenic Hf isotope compositions for a given Nd isotope signature of marine sediments compared to igneous rocks, as represented by the seawater array (Albarède et al., 1998).

The sedimentary Sr isotopic composition is also affected by isotopic fractionation during weathering and transport. Different mineral phases exhibit large variations in radiogenic Sr isotope compositions. Minerals such as K-feldspar, plagioclase, carbonates and micas contain high Sr abundances and thus play an important role in the Sr isotope budget of sediments (Derry and France-Lanord, 1996). Incongruent weathering leads to differences in isotopic compositions of the sediments (e.g., Blum and Erel, 2003) and to a systematic variation of $^{87}Sr/^{86}Sr$ ratios with grainsize during weathering. Clays incorporate a substantial fraction of the isotopic compositions of the waters present during their alteration (Bayon et al., 2016). Therefore, the release of highly radiogenic $^{87}Sr/^{86}Sr$ from micas shifts the isotopic composition of the altered clays towards more radiogenic values (Derry and France-Lanord, 1996).

The Pb isotope compositions of clays are also affected by isotopic fractionation during incongruent weathering and are therefore potentially sensitive to changes in weathering intensities (e.g., Erel et al., 1994; Harlavan and Erel, 2002). Radioactive decay of the U- and Th-series causes radiation damage to the crystal structure of the host minerals. This leads to more loosely bound radiogenic daughter isotopes (^{206}Pb, ^{207}Pb, ^{208}Pb), which are thus easier to mobilize from rocks during weathering compared to the primordial ^{204}Pb isotope (Erel et al., 1994; von Blanckenburg and

Nägler, 2001). Leaching experiments showed that rather than this so-called alpha-recoil process, the preferential dissolution of labile accessory minerals, in particular apatite and sphene, dominates the release of radiogenic Pb isotopes during weak chemical weathering, while the dissolution of major minerals (i.e. feldspars) becomes important during more advanced stages of chemical weathering and enhanced physical erosion (Dausmann et al., 2019). Hence, the Pb isotope composition of weathering solutions and weathered rocks may not reflect that of the source rocks (Frank, 2002).

1.5 Major research goals and outline of thesis

The principal objective of this thesis was to generate the first high-resolution radiogenic isotope record of the clay size fraction for the Miocene period in the Bay of Bengal in order to gain fundamental understanding of the various forcing mechanisms of South Asian monsoon precipitation on orbital to tectonic timescales. The previous proxy records for the SAM have been of insufficient time resolution to investigate the relationship between global climate and the SAM during the Miocene. The continuous sediment archive recovered at IODP Site U1443 in the Bay of Bengal allowed a much more detailed study. The newly established high resolution benthic stable isotope record for Site U1443 provided the climatic and stratigraphic framework to reconstruct Himalayan silicate weathering and its relationship to changes of the SAM and climate during the Miocene based on radiogenic isotope compositions of the clay size fraction. More specifically, the following objectives and research questions are addressed in this thesis:

- *How did the detrital clay radiogenic isotope composition evolve in the Bay of Bengal across the Miocene and how did changes in weathering regime and intensity contribute to global carbon cycle changes?*

  Existing low-resolution radiogenic isotope records from the Bengal Fan and the Ninetyeast Ridge are now complemented using the new high-resolution archive of Site U1443 and allow new insights into links between orbital scale climate variability and monsoon strength. The late Miocene part of the record from 9 to 5 Ma is particularly interesting to reconstruct variability of the monsoon, source contributions and shifts in weathering regime in relation to C4 plant expansion reflected by the global benthic $\delta^{13}C$ decline.

- *What was the radiogenic isotope variability on orbital time scales and can we infer changes in SAM intensity?*

  The study of five selected middle Miocene key climatic intervals at orbital resolution allows to distinguish between tectonic and climatic forcing of monsoon intensity, weathering regime and erosion intensity in the watersheds feeding into the Bay of Bengal. The high

resolution of one of the intervals permits the investigation of orbital periodicities in the record. This helps advancing our understanding of the major controls of past SAM intensity.

- *Did the sources of sediments delivered to the Ninetyeast Ridge change over time and what are the implications for the reconstruction of global climate, tectonics and monsoon intensity?*
  The combination of different isotope systems (Sr, Nd, Hf, Pb) helps to constrain the sources of sediments delivered to the Ninetyeast Ridge, which provides information on which lithologies were eroded and thus allows inferences on tectonic changes, exhumation of rocks, climate and the area of peak monsoon precipitation.

- *What can we infer in terms of continental weathering regime changes during the Miocene and can we apply the newly established $\Delta\varepsilon_{Hf\ clay}$ proxy for the reconstruction of weathering regimes in tropical environments?*
  Radiogenic Sr and Pb isotope systems are known to weather incongruently and can thus provide information on prevailing weathering regimes. The coupling of Nd and Hf isotopes in detrital clays ($\Delta\varepsilon_{Hf\ clay}$) is a relatively new proxy for silicate weathering intensities and has mostly been applied in glacial environments. We now expand the few datasets that exist for tropical environments in order to extract information on past weathering intensity.

1.6 Outline of the thesis and declaration of my own contributions

The doctoral thesis is divided into three main chapters (chapters 3, 4 and 5) providing the main results and discussion of the radiogenic isotope compositions of detrital clays from Site U1443 in the Bay of Bengal and three chapters (chapters 1, 2 and 6) making up the framework of this thesis. The three main chapters are individual and independent scientific manuscripts. Chapter 3 is currently under review, chapter 4 is about to be submitted and chapter 5 is in preparation for submission to a peer-reviewed journal.

Chapter 1 introduces the basics of South Asian monsoon dynamics, the Miocene epoch and radiogenic isotope systematics applied to trace provenance and continental weathering. The major research questions are presented there.

Chapter 2 presents the chemical procedures applied to extract the Sr, Nd, Hf and Pb isotope signatures of detrital clays from the marine sediments.

Chapter 3 presents high-resolution records of Sr, Nd, and Pb isotope compositions of five key climatic intervals of the middle to late Miocene (15.8 to 9.5 Ma), which allow to differentiate long-

term changes in source contributions due to the migration of peak precipitation areas to different regions and orbital-scale excursions likely reflecting climatically driven shifts in monsoon strength. This chapter is currently under review in *Paleoceanography and Paleoclimatology*.

Chapter 3 Declaration: Ed Hathorne proposed this study. He and the Expedition 353 Science Party collected the samples during IODP cruise 353 to the Bay of Bengal. The sediments were washed at the university of Kiel during the construction of the benthic foraminifera stable isotope stratigraphy. I set up the alkaline fusion technique for the complete digestion of the samples and carried out the analyses including leaching of the samples and all the column chemistry as well as the Sr and Nd isotope measurements at GEOMAR after training by Ed Hathorne. Pb isotope measurements were mostly conducted by Huang Huang and Marcus Gutjahr. I interpreted the data and wrote the manuscript, which was improved by contributions from and discussions with the co-authors and two anonymous reviewers.

Chapter 4 presents a 100 kyr resolution clay Sr, Nd, and Pb isotope record for the late Miocene interval from 9 to 5 Ma. We can thus infer effects on the source contributions and shifts in weathering regime in relation to benthic $\delta^{13}C$ decline which characterized global late Miocene carbon cycle changes. Nd and Pb isotope compositions reflect higher Irrawaddy contributions after 7.3 Ma, which was attributed to a climatically driven shift in precipitation patterns. A marked late Miocene increase in Sr isotope compositions suggests enhanced chemical weathering from 6 to 5 Ma.

Chapter 4 declaration: Ed Hathorne proposed this study with CEREGE and Exp. 353 colleague Clara Bolton. He and the Expedition 353 Science Party collected the samples during IODP cruise 353 to the Bay of Bengal. The samples were washed at CEREGE during the construction of the benthic foraminifera stable isotope stratigraphy. I carried out the analyses including leaching of the samples and the column chemistry as well as the Sr and Nd isotope measurements at GEOMAR after training by Ed Hathorne. Pb isotope measurements were mostly conducted by Huang Huang and Marcus Gutjahr. I interpreted the data and wrote the manuscript, which was improved by contributions from and discussions with Martin Frank and Ed Hathorne.

Chapter 5 presents coupled Nd-Hf isotope compositions ($\Delta\varepsilon_{Hf\ clay}$) across the entire middle to late Miocene record (15.8 to 5 Ma) from Site U1443 to trace silicate weathering in warm and humid environments. Extremely high $\Delta\varepsilon_{Hf\ clay}$ signatures are interpreted to reflect high chemical weathering intensities in tropical environments experiencing intense seasonal precipitation.

Chapter 5 declaration: Ed Hathorne proposed this study. He and the Expedition 353 Science Party collected the samples during IODP cruise 353 to the Bay of Bengal. I carried out the analyses including leaching of the samples and the column chemistry. I carried out the Hf isotope measurements with the Help of Ed Hathorne, Marcus Gutjahr and Antao Xu at GEOMAR. I

interpreted the data and wrote the manuscript, which was improved by contributions from and discussions with Martin Frank and Ed Hathorne.

Chapter 6 presents a brief summary of this thesis and an outlook to possible future studies.

2. Methods

This chapter provides an overview of all analytical procedures applied for the extraction of Sr, Nd, Hf, and Pb isotope compositions of the detrital clays including purification and measurement protocols.

2.1 Sample Collection

This thesis is based on sediments of IODP Site U1443 (Latitude 5°23'N; Longitude 90°21'E, water depth: ~2930 m), cored with the RV *JOIDES Resolution* during IODP Expedition 353 in December 2014. Site U1443 was a redrill of nearby ODP Site 758 and located on the crest of the Ninetyeast Ridge in the southern Bay of Bengal (Fig. 1.1). Four holes were combined to form a splice comprising sediments from the Oligocene to the late Pleistocene. The recovered sediment is a nannofossil ooze with varying abundances of detrital clays, foraminifers, and authigenic carbonates (Clemens et al., 2016).

2.2. Leaching procedure

The sediment samples were washed over a 63 µm sieve and the fine fraction was collected in 3 liter plastic bags. While the coarser fraction was used for micropaleontological studies, the fine fraction was freeze-dried and leached to remove all authigenic Fe-Mn oxyhydroxides. The leaching procedure followed a modified method for the extraction of seawater Nd and Pb isotopic compositions from Fe-Mn coatings described by Gutjahr et al. (2007). ~2 g of fine sediments were washed with deionized water (Milli-Q, 18.2 MΩcm) three times to eliminate the soluble fraction, each rinsing cycle including the suspension of the sediment in deionized water using a vortex mixer, centrifugation of the suspension until the supernatant was free of particles, and decanting the supernatant. The samples were then leached with a 10 % concentrated 0.05M hydroxylamine hydrochloride–15% distilled acetic acid–0.03M Na-EDTA solution, buffered to pH 4 with analytical grade NaOH. For this first leaching, the sample and leaching solution were shaken for 30 seconds, then centrifuged and the supernatant pipetted off and kept for potential future analysis of the seawater signature. To fully decarbonate the samples, 40 % acetic acid was added to the samples and shaken overnight, then centrifuged and the supernatant decanted. This step was repeated until no reaction of the samples was visible anymore. Subsequently, the samples were leached with 20 ml undiluted leaching solution and shaken overnight before the supernatant was decanted to make sure that the authigenic Fe-Mn oxyhydroxide fractions were completely removed. The samples were washed three times with Milli-Q again and then the clay fraction (<2 µm) was separated using a centrifuge-based Atterberg method. The required settling time and speed were calculated using the

freely available software SediCalc (Krumm, 2006). The leached detritus was filled up to 40 ml with deionized water and suspended and then centrifuged 9 minutes and 11 seconds at 500 rpm. The supernatant with suspended clay-sized particles was pipetted into a second centrifuge tube, which was then centrifuged at full speed for at least 30 minutes to decant the supernatant water. The residual clay fraction was dried at low temperature (<45°C) in an oven. To ensure that the clay separation was complete, a few samples were cross-checked on a laser particle-sizer.

2.3 Total dissolution applying the alkaline fusion method

A complete sample digestion is a prerequisite for precise and accurate isotope composition determinations and has commonly been achieved by HF-acid digestions (e.g., Yu et al., 2001). To avoid handling of concentrated HF and to guarantee rapid and complete digestion of all rock-forming minerals including highly resistant minerals such as zircons, we now established a new technique at GEOMAR based on the alkaline fusion method by Bayon et al. (2009a) but without addition of TiO_2, Fe_2O_3 or Tm. In order to check the accuracy of the obtained data and to assess potential blank contributions from the reagents, various rock reference materials were digested applying the new technique and were purified and analyzed, and their isotope compositions checked against published analytical values compiled by the GeoReM database (Fig. 2.1; Table 2.1; Jochum et al., 2005). Procedural blanks were low (<1 %) for Nd, Hf and Pb isotope measurements but contributed up to 8.8 % of the total Sr signal. This rather high contribution originated from the NaOH and NaO_2 used for the alkaline fusion. To correct for the blank contributions, samples of the reagents were regularly digested and measured for concentrations (n=15). These were later combined and measured for their isotopic composition. The blank contributions were then removed from the sample Sr isotope signals via mass balance calculations.

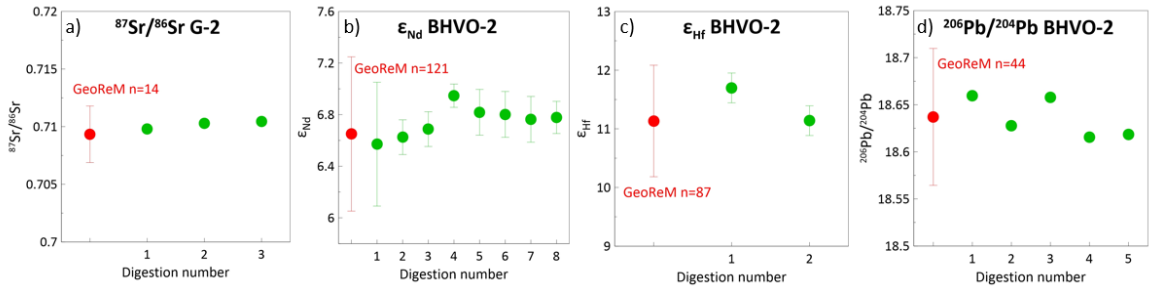

Fig. 2.1: Examples of radiogenic Sr (a), Nd (b), Hf (c) and Pb (d) isotope compositions of geological reference materials measured following the digestion with the alkaline fusion technique compared to literature values from the GeoReM database. The error bars for Sr and Pb isotope ratios are within the symbol size.

Table 2.1: Average (av.) isotope compositions including standard deviations (2SD) of three rock reference materials of this study compared to published data compiled by the GeoReM database (Jochum et al., 2005).

	BHVO-2	MAG-1	G-2
$^{87}Sr/^{86}Sr$			
GeoReM av. ± 2SD	0.70348 ± 0.00006 (n=99)	0.72274 ± 0.00031 (n=4)	0.70934 ± 0.00245 (n=14)
this study av. ± 2SD	0.70364 ± 0.00014 (n=7)	0.72597 ± 0.00716 (n=7)	0.71018 ± 0.00067 (n=3)
ε_{Nd}			
GeoReM av. ± 2SD	6.65 ± 0.60 (n=121)	-10.85 ± 0.58 (n=6)	-7.87 ± 0.39 (n=12)
this study av. ± 2SD	6.74 ± 0.25 (n=8)	-10.92 ± 0.36 (n=5)	-8.00 ± 0.61 (n=2)
ε_{Hf}			
GeoReM av. ± 2SD	11.13 ± 0.95 (n=87)	-7.04 ± 3.33 (n=6)	-9.61 ± 0.68 (n=8)
this study av. ± 2SD	11.42 ± 0.79 (n=2)	-8.15 ± 2.51 (n=3)	-9.71 ± 0.25 SE (n=1)
$^{206}Pb/^{204}Pb$			
GeoReM av. ± 2SD	18.637 ± 0.073 (n=44)	18.861 ± 0.001 (n=2)	18.403 ± 0.013 (n=7)
this study av. ± 2SD	18.636 ± 0.043 (n=5)	18.865 ± 0.043 (n=3)	18.425 ± 0.041 (n=2)

For the alkaline fusion, about 100 mg of the dried silicate clays were placed into a graphite crucible together with 1.2 g of Na_2O_2 and 0.6 g of NaOH pellets. The mixture was put into a muffle furnace at 650-700 °C for 15 minutes. After removing the crucibles, they were left to cool for ~5 minutes. Ten ml of Milli-Q H_2O were added to the fused bead and the crucibles were placed on a hotplate at ~90 °C. Stirring with a pipette tip helped disaggregating the solid bead in the crucible. The solution was then transferred into clean 30 ml teflon vials and ~15 ml Milli-Q were used to rinse the crucible and make sure that the mixture was completely transferred into the vial. The closed vials were transferred into the clean lab and put on a hotplate at 130 °C for two hours. After cooling down again, the mixture was transferred into clean 50 ml centrifuge tubes and centrifuged at 3000 rpm for three minutes. The supernatant was discarded and the tubes with the remaining solids were filled again with 15 ml Milli-Q, shaken, and then centrifuged again and the supernatant discarded. This step was repeated one more time. Finally, 5 ml of 6 M HCl were added to dissolve the solid. The solution was split into three aliquots; 2 ml for Nd-Hf, 2 ml for Pb-Sr and 1 ml was kept for storage.

2.4 Ion exchange chromatographic purification of Sr, Nd, Hf and Pb

To separate and purify Sr, Nd, Hf and Pb to avoid isobaric interferences and matrix effects during measurement, standard ion chromatographic procedures were applied. All samples were centrifuged prior to column chromatography to avoid loading undissolved particles onto the ion exchange columns. For Nd and Hf, first the REEs (including Nd) were separated from the HFSEs (including Hf) and from other matrix elements using a cation exchange resin (Bio-Rad AG 50W-X8, 200-400 mesh) following the elution scheme in Table 2.2. The Nd was then separated from the other REEs using 2 ml Eichrom® Ln-Spec resin (50-100 µm mesh) following the procedure shown

in Table 2.3 modified from Pin and Zalduegui (1997). The procedure to purify Hf from the other HFSEs changed during the thesis. For the first set of samples, Hf was separated using Eichrom® Ln-Spec resin (100-150 µm mesh) following the method of Münker et al. (2001) (Table 2.4). For most of the remaining samples, the method was streamlined to use 1.6 ml of Bio-Rad AG1-X8 resin (200-400 mesh) following a modified scheme of Sahoo et al. (2006) (Table 2.5). For the purification of Pb, the combined Sr-Pb aliquot was first dried three times in 2M hydrobromic acid (HBr) before being dissolved in the carrier acid and being passed through 100 µl Bio-Rad AG1-X8 resin (100-200µm mesh), as described in Table 2.6 (modified from Galer and O'Nions, 1989). The cut containing Sr was separately collected from the Pb columns and further purified for Sr using 50 µl Eichrom® Sr-Spec resin (50-100 µm mesh) following the modified protocol of Horwitz et al. (1992) (Table 2.7). To remove residual traces of the resin as well as organic compounds, the Sr, Nd and Hf cuts were treated with 100 µl of concentrated HNO_3 and 100 µl H_2O_2 (30 wt.%, Merck Suprapur®).

Table 2.2: Cation AG50W-X8 (1.4 ml, 200-400 µm) column chemistry to separate Hf and REE

Step	Volume	Reagent
pre-clean	8 ml	6M HNO_3/0.5M HF
acid change	2 x 1 ml	Milli-Q
conditioning	0.5 ml	1M HCl/0.05M HF
conditioning	1 ml	1M HCl/0.05M HF
load sample and directly collect Hf	**2 ml**	**1M HCl/0.05M HF (sample)**
collect Hf	**2 ml**	**1M HCl/0.05M HF**
elute Fe	5 ml	3M HCl
change of acid	2 x 1ml	Milli-Q
elute Ba	12 ml	2M HNO_3
collect REE/Nd	**6 ml**	**6M HNO_3**
cleaning	6 ml	6M HNO_3/0.5M HF
pass	3 x 1ml	Milli-Q
store	1 ml	Milli-Q

Table 2.3: Eichrom® Ln-Spec (2 ml, 50-100 µm) column chemistry for Nd purification (modified form Pin and Zalduegui, 1997)

Step	Volume	Reagent
pre-clean	8 ml	6M HCl
conditioning	0.5 ml	0.1 M HCl
conditioning	1 ml	0.1 M HCl
load sample	**0.5 ml**	**0.1 M HCl (sample)**
wash and elute Ba	0.5 ml	0.1 M HCl
elute LREE	7.5 ml	0.25 M HCl
collect Nd	**5 ml**	**0.25 M HCl**
clean	8 ml	6M HCl
pass	1 ml	0.3M HCl
store	1 ml	0.3M HCl

Table 2.4: Eichrom® Ln-Spec (1 ml, 100-150 µm) column chemistry for Hf purification (modified from Münker et al., 2001)

Step	Volume	Reagent
pre-clean	15 ml	6M HCl
pre-clean	15 ml	2M HF
wash HF	2 ml	Milli-Q
conditioning	2 x 3 ml	3M HCl
add ascorbic acid to each sample and load the sample	**4 ml + 0.8 ml**	**3M HCl + 0.4M ascorbic acid**
elute matrix, REE	2 x 25 ml	6M HCl
change of acid	2 x 3 ml	Milli-Q
elute Ti	30 ml	0.45M HNO_3 + 0.09M citric acid + 1wt% H_2O_2
change of acid	2 x 3 ml	Milli-Q
elute Zr	5 ml	2M HCl + 0.1M HF
collect Hf	**6 ml**	**3M HCl + 0.2M HF**
clean	25 ml	6M HCl
clean	25 ml	2M HF
Pass/store	3 ml	1M HCl

Table 2.5: Anion Bio-Rad AG1X-8 (1.6 ml, 200-400 µm) column chemistry for Hf purification (modified from Sahoo et al., 2006)

Step	Volume	Reagent
pre-clean	8 ml	9M HCl/1M HF
pre-clean	2 x 8 ml	Milli-Q
pre-condition	8 ml	0.1 M HF
load sample	2 ml	**0.1 M HF (sample)**
elute Fe, Ti	4 ml	0.1 M HF + 2% H_2O_2
elute Zr, Ti (Hf)	3 ml	1 M HF + 0.2% H_2O_2
wash resin	3 ml	Milli-Q
collect Hf	6 ml	**6M HCl**
clean, elute W	8 ml	9M HCl/1M HF
pass/store	2 + 2 ml	Milli-Q

Table 2.6: Bio-Rad AG1-X8 resin (100 µl, 100-200 µm) column chemistry for Pb purification (modified from Galer and O'Nions, 1989)

Step	Volume	Reagent
clean columns	1 res.	1M HNO_3
clean columns	1 res.	Milli-Q
load resin	50 µl resin	resin
clean resin	2 x 1 ml	0.25M HNO_3
condition resin	2 x 100 µl	0.5M HNO_3/0.2M HBr
load sample & collect (for Sr)	**300 µl**	**0.5M HNO_3/0.2M HBr (sample)**
elute & collect (for Sr)	2 x 100 µl	0.5M HNO_3/0.2M HBr
elute & collect (for Sr)	2 x 150 µl	0.5M HNO_3/0.2M HBr
collect Pb	**150 µl**	**0.5M HNO_3/0.03M HBr**
collect Pb	**2 x 300 µl**	**0.5M HNO_3/0.03M HBr**
used resin to waste	backwash	Milli-Q

Table 2.7: Eichrom® Sr-Spec (50 µl, 50-100 µm) column chemistry for Sr purification (modified from Horwitz et al., 1992)

Step	Volume	Reagent
clean column	1 res.	0.1M H_2SO_4
clean column	2 x 1 res.	Milli-Q
load resin	50 µl	resin
clean resin	1 ml	0.1M H_2SO_4
clean resin	2 x 1 res.	Milli-Q
condition resin	2 x 50 µl	3M HNO_3
condition resin	2 x 75 µl	3M HNO_3
load sample	**50 µl**	**3M HNO_3 (sample)**
elute sample	2 x 50 µl	3M HNO_3
elute sample	300 µl	3M HNO_3
collect Sr	**500 µl**	**Milli-Q**
salvage used resin	backwash	Milli-Q

2.5 Acquisition of Sr, Nd, Hf and Pb isotope ratios

The Sr isotope and some Nd isotope measurements were performed on a Nu Plasma (Nu Instruments Limited) high-resolution MC-ICP-MS at GEOMAR while most Nd and Hf and all Pb isotope analyses were carried out on a Thermo Scientific Neptune Plus MC-ICP-MS at GEOMAR. For the measurements the samples were dissolved in the carrier acid 0.3M HNO_3 (for Sr, Nd and Pb) or 0.5M HNO_3/0.1M HF (for Hf). Before measuring the isotope ratios, the concentration of each sample was established by diluting a small aliquot of the sample solution. This enabled the dilution of the samples to concentrations matching those of the standards, which were measured repeatedly between samples. Nd isotope ratios were corrected for instrumental mass bias using a $^{146}Nd/^{144}Nd$ of 0.7219 (Vance and Thirlwall, 2002) and were normalized to the accepted values of the JNdi-1 standard (0.512115; Tanaka et al., 2000). The instrumental mass bias of Sr isotopic measurements was corrected using an $^{88}Sr/^{86}Sr$ of 0.1194 (Steiger and Jäger, 1977) and normalized to the NIST SRM 987 $^{87}Sr/^{86}Sr$ of 0.710245. Hf isotope ratios were corrected for instrumental mass bias using a $^{179}Hf/^{177}Hf$ of 0.7325. Mass-bias corrected values for $^{176}Hf/^{177}Hf$ were normalized to a JMC 475 value of 0.282163 (Blichert-Toft, 2008; Blichert-Toft and Albarède, 1997). The mass bias correction for the Pb isotope measurements was carried out by doping the samples with the NIST997 Tl standard solution (Pb/Tl ~4) (Belshaw et al., 1998; White et al., 2000). Since Tl and Pb fractionate slightly differently during ionization (Vance and Thirlwall, 2002), the $^{205}Tl/^{203}Tl$ ratio

was adjusted on a session-by-session basis in order to match accepted SRM 981 Pb isotope compositions ($^{206}Pb/^{204}Pb$ = 16.9416, $^{207}Pb/^{204}Pb$ = 15.4998 and $^{208}Pb/^{204}Pb$ = 36.7249; Baker et al., 2004).

In addition to repeated measurements of certified as well as in-house standard solutions, the multiple digestion and measurement of various rock reference materials allowed the estimation of the external reproducibility of the isotope measurements. These and the measured blank concentrations are reported separately in the following chapters.

3. Scientific Chapter I

Provenance and weathering of clays in the Bay of Bengal during the Miocene: Linkages to tectonics and monsoonal climate

Submitted to *Paleoceanography and Paleoclimatology* as: Bretschneider, L., Hathorne, E.C., Huang, H., Lübbers, J., Kochhann, K.G.D., Holbourn, A., Kuhnt, W., Thiede, R., Gebregiorgis, D., Giosan, L. and Frank, M.: Provenance and weathering of clays in the Bay of Bengal during the Miocene: Linkages to tectonics and monsoonal climate.

Abstract

Tectonics and regional monsoon strength control weathering and erosion regimes of the watersheds feeding into the Bay of Bengal, which are important contributors to global climate evolution via carbon cycle feedbacks. The detailed mechanisms controlling the input of terrigenous clay to the Bay of Bengal on tectonic to orbital timescales are, however, not yet well understood. We produced orbital-scale resolution geochemical records for International Ocean Discovery Program Site U1443 (southern Bay of Bengal) across five key climatic intervals of the middle to late Miocene (15.8 – 9.5 Ma). Our new radiogenic Sr, Nd, and Pb isotope time series of clays transported to the Ninetyeast Ridge suggest that the individual contributions from different erosional sources overall remained remarkably consistent during the Miocene, despite major tectonic reorganizations in the Himalayas. On orbital timescales, however, high-resolution data from the five investigated intervals show marked fluctuations of all three isotope systems. Interestingly, variability was much higher within the Miocene Climatic Optimum (around 16-15 Ma) and across the major global cooling (~13.9-13.8 Ma) until ~13.5 Ma, than during younger time slices. This change is attributed to a major restriction on the supply of High Himalayan erosion products due to migration of the peak precipitation area towards the frontal domains of the Himalayas and the Indo-Burman Ranges. The transient excursions of the radiogenic isotope signals on orbital timescales most likely reflect climatically driven shifts in monsoon strength.

3.1 Introduction

The South Asian monsoon (SAM) influences the lives of more than a billion people, but remains difficult to predict. It is thus crucial to understand how the monsoon behaves under different boundary conditions such as a warmer world with reduced continental ice cover. Many studies have focused on the Late Quaternary glacial-interglacial cycles to reconstruct how monsoon strength, weathering intensity and global climate have been linked on orbital timescales (e.g., Ahmad et al., 2005; Colin et al., 1999; Gebregiorgis et al., 2018; Joussain et al., 2016; Li et al., 2018; Wilson et al., 2015), but there are fewer studies of warmer periods in the geological past. Since the monsoon

is thought to have initiated during the warmer than present Miocene (Clift et al., 2008), this period of time offers a unique window into past monsoon variability and its controlling factors. Studies that investigated the relationship between variations of the SAM and the erosional regime during the Miocene period were conducted at low time resolution (e.g., France-Lanord et al., 1993: Myr timescale; Banerjee et al., 2019: ~500 kyr resolution), and thus do not allow insights into the links between orbital-scale climate variability and monsoon strength.

The continuous sediment archive recovered at IODP Site U1443 in the Bay of Bengal (Fig. 3.1) now allows a much more detailed study. Lübbers et al. (2019) established a high resolution benthic stable isotope record from 13.5 to 8.2 Ma for Site U1443, which provides the climatic and stratigraphic framework to reconstruct Himalayan silicate weathering and its relationship to changes of the SAM and climate during the Miocene based on radiogenic isotope compositions of the clay size fraction. Since tectonics, climate, erosion, type and intensity of weathering and monsoon strength can all affect the detrital isotope signatures on different time scales, our approach is to disentangle the different factors using higher temporal resolution records than in previous work to advance our understanding of the major controls of past SAM intensity.

The Bay of Bengal receives large freshwater and sediment inputs from the rivers draining the Himalaya (Ganges, Brahmaputra, Meghna), the Indo-Burman Ranges and the Arakan coast (Irrawaddy), and the Indian Peninsula (Godavari, Krishna, Mahanadi) (Fig. 3.1). The sediments deposited in the Bay of Bengal mainly originate from Himalayan erosion and have formed the Bengal Fan, the world's largest submarine fan with a sediment volume of $12.5*10^6$ km^3 (Curray et al., 2003). The Bengal Fan has existed since at least early Miocene times (Derry and France-Lanord, 1996; France-Lanord et al., 1993) and its deposits provide a record of the erosion and weathering history of the surrounding mountain belts, as a consequence of the continental Indian-Eurasian collision and the resulting uplift history of the Himalayas (Colin et al., 1999; France-Lanord et al., 1993). In the modern system, 95% of the volume of sediments is transported to the Bay of Bengal during peak monsoon precipitation (Singh et al., 2007) and thus the variability of erosion intensity and deposition rates is directly related to changes in monsoonal precipitation. The erosion of the Himalayas is considered to be fundamental for regulating Earth's climate because the sequestration of CO_2 through enhanced silicate weathering and the burial of organic carbon in the fan result in lower global temperatures (France-Lanord and Derry, 1997; Galy et al., 2007; Galy et al., 2010; Raymo, 1994; Raymo and Ruddiman, 1992).

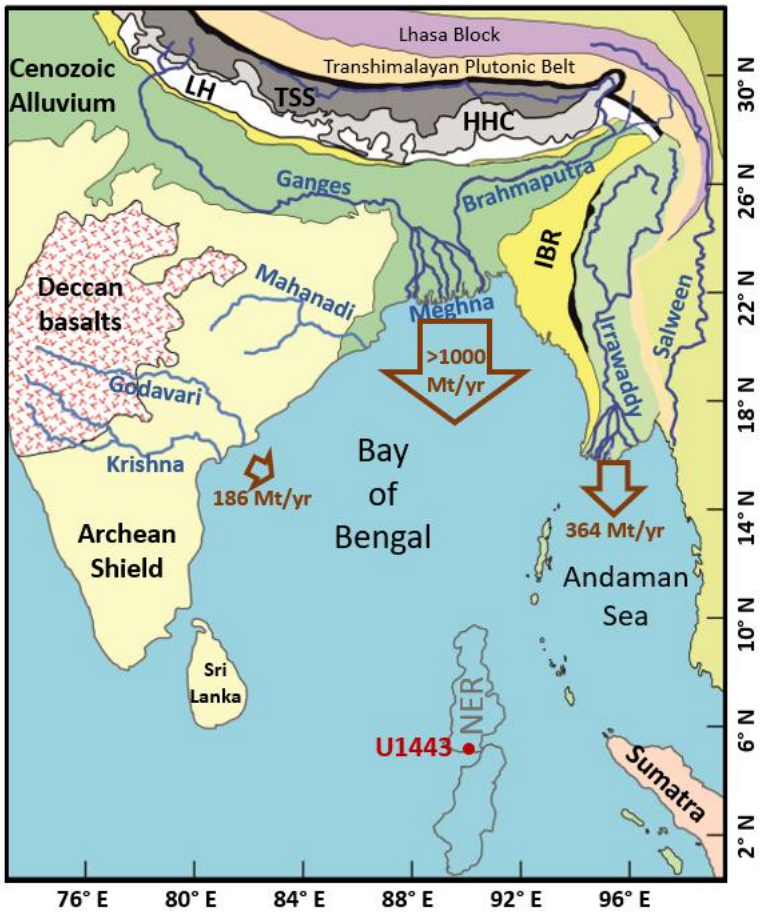

Fig. 3.1: Map of the Bay of Bengal modified from Ali et al. (2021). The location of IODP Site U1443 on the Ninetyeast Ridge (NER) is marked. The major continental river systems are indicated as well as the major geological units: LH = Lesser Himalayas, TSS = Tethyan Sedimentary Series, HHC = High Himalayan Crystalline, and IBR = Indo Burman Ranges. The arrows indicate modern sediment fluxes from major rivers (Milliman and Syvitski, 1992; Robinson et al., 2007).

Radiogenic Sr, Nd, and Pb isotope compositions of detrital materials transported to the central Bay of Bengal vary as a function of the age and the geological history of the continental rocks in the hinterland and, therefore, serve as reliable tracers of the sediment sources (Ahmad et al., 2005; Colin et al., 1999). The continental lithologies surrounding the Bay of Bengal constrain the possible endmembers for the mixture of sediment deposited at Site U1443. Within the Himalayas, at least four main lithologies are likely sources: The Lesser Himalaya (LH), the High Himalayan Crystalline (HHC), the Tethyan Sedimentary Series (TSS) and the Transhimalayan Plutonic Belt (TPB) (France-Lanord and Le Fort, 1988; Galy et al., 1996; Gansser, 1964; LeFort, 1975; Singh and France-Lanord, 2002). Another important source are the Indo-Burman Ranges (IBR), which are drained by the Irrawaddy River (Giosan et al., 2018). Based on the mixture of these distinct sediment source signatures in the Bay of Bengal, the location of highest monsoon precipitation as well as erosional and tectonic changes can be reconstructed. Sr and Pb isotope compositions are additionally influenced by fractionation during weathering and transport due to large variations in the isotope composition of different mineral phases and differences in their resistance to weathering

(Ali et al., 2015; Blum et al., 1993; Tütken et al., 2002). These signals can potentially provide useful information on prevailing types and intensities of weathering and thus help reconstructing past weathering regimes.

The Miocene epoch (23.03-5.33 Ma) was characterized by pronounced global climatic changes. The Miocene Climatic Optimum (MCO, ~17 to 15 Ma) was a warm period with global annual mean temperatures ~3°C higher than today, based on proxy data constraining land and sea surface temperatures (You et al., 2009). Taking into account variations in global tectonic boundary conditions, Miocene climate reconstructions thus allow insights into the ability of climate models to simulate warm climates, comparable to those the Earth may experience in the near future (Henrot et al., 2017). The MCO was followed by a stepwise cooling trend with development of a permanent Antarctic ice-sheet after ~13.8 Ma (e.g., Holbourn et al., 2005), that was associated with a marked decrease in atmospheric CO_2 (Foster et al., 2012). Miocene climatic changes and tectonic events may have been closely linked, since erosion intensity increases with the amount of precipitation, which in turn influenced relief and exhumation rates (Deng et al., 2019). Furthermore, Raymo (1994) proposed that increased silicate weathering, as well as organic carbon burial, promotes CO_2 drawdown and may have led to the global cooling in the middle Miocene.

The study by Allen and Armstrong (2012) summarized the main tectonic events in the Himalayan-Tibetan region during the Miocene, which comprised a reorganization of the thrusting, which propagated south from the Main Central Thrust. Large changes in tectonic regime have been inferred for the middle Miocene, starting with synchronous ductile shear along the South Tibetan Detachment System and the Main Central Thrust (Burchfiel et al., 1992; Hodges et al., 1998; Kellett et al., 2009; Searle et al., 2008), contemporaneous with leucogranite generation and rapid exhumation (Catlos et al., 2004; Thiede et al., 2004). This was followed by the onset of ~N-S oriented normal faulting in southern Tibet and thrusting south of the Main Central Thrust (Allen and Armstrong, 2012; Molnar and Tapponnier, 1978), as well as a decrease in exhumation rates of the High Himalayas at ~16 Ma (Najman et al., 2009; Thiede et al., 2009). These processes played an important role in determining which Himalayan rocks were exposed and were thus subject to erosion during particular periods of time. Changes in the tectonically induced exposure of different rock types are therefore expected to be reflected by source changes of the eroded material in the Bay of Bengal sediments. Despite this, previous studies have shown that the sources of sediments in the Bay of Bengal have remained overall similar since at least the early Miocene (Ali et al., 2021; Bouquillon et al., 1990; France-Lanord et al., 1993). However, on orbital timescales, significant variations in the provenance and grain size of sediments have been observed and attributed to climate and monsoon changes (Ahmad et al., 2005; Bookhagen et al., 2006; Clift et al., 2008; Colin et al., 1999; Tripathy et al., 2011). Over the most recent glacial-interglacial cycles, the interglacials were generally dominated by a strong summer monsoon, while the glacials were drier and suggested

to have been characterized by a stronger winter monsoon (Ahmad et al., 2005; Galy et al., 2008; Joussain et al., 2016; Li et al., 2018; Tripathy et al., 2011; Wilson et al., 2015). However, in detail, this relationship is not always as clear and periods with strong monsoons were also recognized during glacials (Bolton et al., 2013; Gebregiorgis et al., 2018).

Here we follow a similar high-resolution approach to the glacial-interglacial studies, to reconstruct both long and short-term monsoon variability. However, instead of using Bengal fan sediments, which are often disturbed and discontinuous due to the occurrence of turbidites (e.g., Derry and France-Lanord, 1996; Galy et al., 1996; Galy et al., 2010), we analyze the continuous sediment record of the crest of the Ninetyeast Ridge (NER). Moreover, we focus on the detrital clay size to minimize mineral sorting effects, which may occur during transport. Since the time-consuming preparation of the samples limits the number of analyses of radiogenic isotopes, we focus on orbital-scale variability during five selected Miocene key climatic intervals to better constrain the roles of tectonics and global climate in driving regional monsoon intensity and erosion and to discuss potential interactions and feedbacks between them. The selected intervals include the central part of the MCO (15.8 – 15.3 Ma), two global cooling steps from 14 to 13.5 Ma and 13.3 to 12.8 Ma, the event of peak warmth at 11 – 10.5 Ma and an interval marking the transition from ~100 kyr periodicity to the dominant 41 kyr variability in benthic $\delta^{18}O$ (10 – 9.5 Ma).

3.2 Materials & Methods

Our study is based on sediments of IODP Site U1443 (Latitude 5°23'N; Longitude 90°21'E, water depth: ~2930 m), cored with the RV *JOIDES Resolution* during IODP Expedition 353 in December 2014. Site U1443 was a redrill of nearby ODP Site 758 and located on the crest of the NER in the southern Bay of Bengal. This ridge-top location ensured a slow and continuous sedimentation and prevented the deposition of disturbed sedimentary sequences typically associated with transport processes on the Bengal Fan (Clemens et al., 2016). The average sedimentation rates during the Miocene varied between 0.41 cm/kyr in the late to middle Miocene and 0.81 cm/kyr in the early Miocene to Oligocene. Four holes were combined to form a splice comprising sediments from the Oligocene to the late Pleistocene. The recovered sediment is a nannofossil ooze with varying abundances of detrital clays, foraminifers, and authigenic carbonates (Clemens et al., 2016). The Miocene samples investigated in this study span a composite depth between 125.88 and 152.78 m below seafloor. The age model is based on the isotope stratigraphy of Lübbers et al. (2019) for the intervals younger than 13.5 Ma and of K. Kochhann (personal communication, 2020) for the intervals older than 13.5 Ma. The Irrawaddy samples were collected during field expeditions to the Irrawaddy delta in 2016 and 2017 (for further information see Giosan et al., 2018).

The sediment samples were washed over a 63 µm sieve and the fine fraction collected in 3 liter plastic bags. While the coarser fraction was used for micropaleontology, the fine fraction was freeze-dried and leached to remove all authigenic Fe-Mn oxyhydroxides. The leaching procedure was modified from Gutjahr et al. (2007). Briefly, ~2 g of fine sediments were washed with deionized water, leached step by step with a 0.05M hydroxylamine hydrochloride–15% acetic acid–0.03M Na-EDTA solution, buffered to pH 4 with analytical grade NaOH, and fully decarbonated with 40% acetic acid. Having been washed again with deionized water, the clay fraction was separated using a centrifuge-based Atterberg method.

For the Sr, Nd and Pb isotope analyses, the clay fraction was then dried at low temperature (<45°C) in an oven. For the Irrawaddy samples, both clay and >2µm fractions were dried and digested. About 100 mg of the dried silicate clays (and silts) were completely digested using alkaline fusion ($NaOH$-Na_2O_2), as described in Bayon et al. (2009a) but without addition of TiO_2, Fe_2O_3 or Tm, and then further dissolved in 6 M HCl. To separate and purify Nd, Sr and Pb, standard ion chromatographic procedures were applied (Cohen et al., 1988; Galer and O'Nions, 1989; Pin and Zalduegui, 1997). For Nd, first the REEs (including Nd) were separated using a cation exchange resin (Bio-Rad AG 50W-X8, 200-400 mesh), while most matrix elements were discarded. The Nd was then separated from the other REEs using Ln-spec resin (50-100 µm). Pb and Sr were separated using AG1-X8 (100-200 µm) and Sr-Spec resin, respectively. Sr isotope and some Nd isotope measurements were performed on a Nu Plasma high-resolution MC-ICP-MS at GEOMAR while most Nd and all Pb isotope analyses were carried out on a Thermo Scientific Neptune Plus MC-ICP-MS at GEOMAR.

Nd isotope ratios were corrected for instrumental mass bias using a $^{146}Nd/^{144}Nd$ of 0.7219 (Vance and Thirlwall, 2002) and were normalized to the accepted values of the JNdi-1 standard (0.512115; Tanaka et al., 2000). The Nd isotope ratios are reported as εNd(0) values = $(((^{143}Nd/^{144}Nd)_{sample}/(^{143}Nd/^{144}Nd)_{CHUR} - 1) \times 10^4$ with CHUR being the Chondritic Uniform Reservoir and $(^{143}Nd/^{144}Nd)_{CHUR} = 0.512638$ (Jacobsen and Wasserburg, 1980). Procedural blanks for Nd were <0.5 ng and thus below 0.5% of the total amount of Nd in the samples. Separate digestions and measurements of USGS reference material BHVO-2 (n=8) gave a mean εNd value of 6.75±0.24, which agrees well with the mean value (6.65±0.60) compiled by the GeoReM database (Jochum et al., 2016).

The instrumental mass bias of Sr isotopic measurements was corrected using a $^{88}Sr/^{86}Sr$ of 0.1194 (Steiger and Jäger, 1977) and normalized to the NIST SRM 987 $^{87}Sr/^{86}Sr$ of 0.710245. Procedural blanks were on average 50 ng, contributing between 0.7 and 8.8 % of the total Sr signal. This rather high contribution originated from the NaOH and NaO_2 used for the alkaline fusion. To correct for the blank contributions, samples of the reagents were regularly digested and measured for concentrations (n=15). These were later combined and measured for their isotopic composition.

The blank contributions were then removed from the Sr sample signals via mass balance calculations. Repeated digestions and measurements of USGS reference material BHVO-2 (n=12) gave a mean $^{87}Sr/^{86}Sr$ value of 0.70363±0.00013, which is in good agreement with the GeoReM average value of 0.70348±0.00006.

The mass bias correction for the Pb isotope measurements was carried out by doping the samples with the NIST997 Tl standard solution (Pb/Tl ~4) (Belshaw et al., 1998; White et al., 2000). Since Tl and Pb fractionate slightly differently during ionization (Vance and Thirlwall, 2002), $^{205}Tl/^{203}Tl$ was adjusted on a session-by-session basis in order to match accepted SRM 981 Pb isotope compositions ($^{206}Pb/^{204}Pb$ = 16.9416, $^{207}Pb/^{204}Pb$ = 15.4998 and $^{208}Pb/^{204}Pb$ = 36.7249; Baker et al., 2004). Repeated processing and analysis of USGS reference material BHVO-2 (n=6) gave mean values (±2 standard deviations) of 18.619±0.090, 15.536±0.019, and 38.219±0.052 for $^{206}Pb/^{204}Pb$, $^{207}Pb/^{204}Pb$, and $^{208}Pb/^{204}Pb$, respectively. These Pb isotope values agree well with those previously measured for BHVO-2 (n=44, 18.637±0.073, 15.528±0.045, and 38.223±0.103; GeoReM database). Procedural blanks for Pb were <70 pg and contributed less than 0.1% of the total amount of Pb in the samples.

In order to identify cyclic changes in contributions from the source areas reflected by the radiogenic isotope compositions of the clay fractions, spectral analyses of the records were performed on unevenly spaced time series using REDFIT (Schulz and Mudelsee, 2002).

3.3 Results

The ε_{Nd}, $^{87}Sr/^{86}Sr$ and Pb isotope compositions ($^{206}Pb/^{204}Pb$, $^{207}Pb/^{204}Pb$, $^{208}Pb/^{204}Pb$, $^{207}Pb/^{206}Pb$ and $^{208}Pb/^{206}Pb$) of the silicate clay fraction are shown in Figure 3.2 and Table A1 and A3. The ε_{Nd} values range from -13.3 to -8.6 and exhibit highest variability during the MCO and the 14-13.5 Ma interval, which comprises the global cooling step at ~13.9-13.8 Ma. The least radiogenic ε_{Nd} values (-13.3) were found at 13.7 Ma. The $^{87}Sr/^{86}Sr$ compositions vary between 0.71119 and 0.71661, also showing the highest fluctuations and highest values, in the two older intervals. The youngest two investigated intervals after the cooling only show minor variability and overall lower values, ranging from 0.71119 to 0.71306. $^{206}Pb/^{204}Pb$ values vary between 18.84 and 19.10 and exhibit a clear radiogenic peak and the highest variability at the beginning of cooling at ~14 Ma.

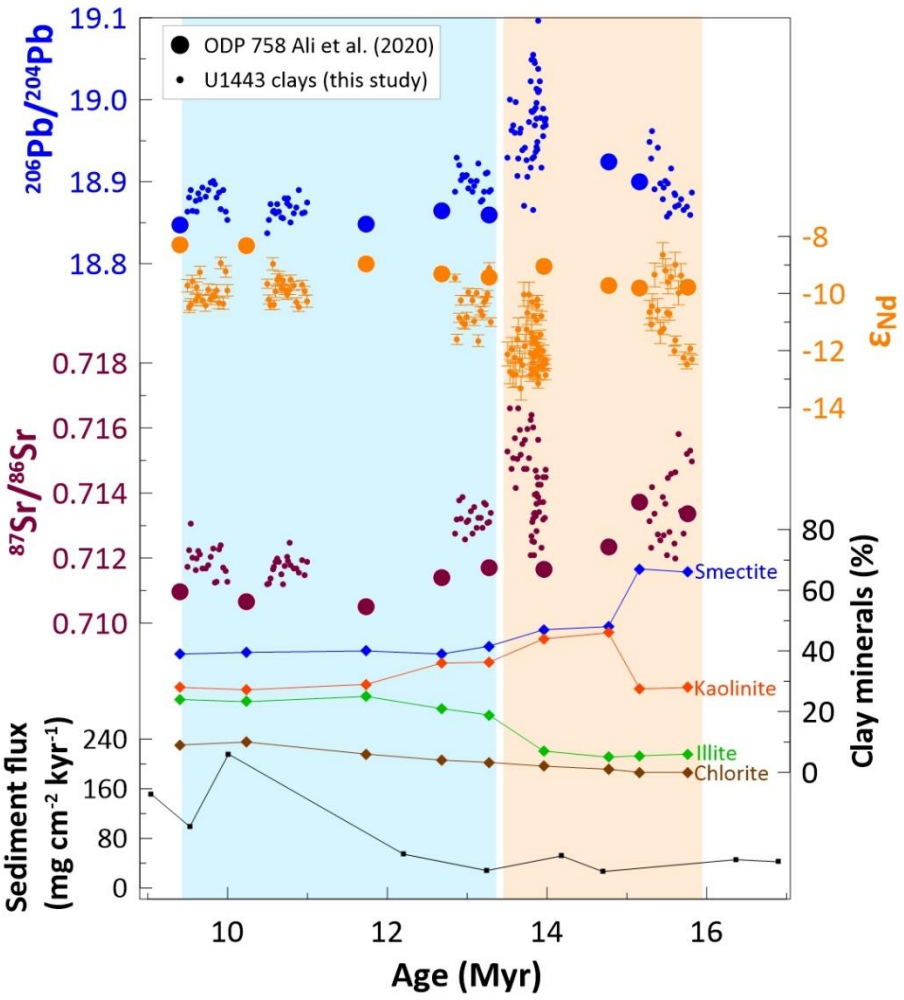

Fig. 3.2: Radiogenic Pb, Sr and Nd isotope compositions of the U1443 clay samples for the five investigated Miocene time intervals. The larger symbols represent part of the ODP Site 758 low resolution clay record by Ali et al. (2021). The light orange shaded interval marks high variability of the radiogenic isotopes while the blue shaded interval reflects the low variability after the first Miocene cooling interval. The relative abundances of the clay minerals smectite, kaolinite, illite and chlorite from ODP Site 758 (Ali et al., 2021) are shown, as well as the sediment flux record of ODP Site 758 (Hovan & Rea, 1992; recalculated by Ali et al., 2021).

To evaluate potential grain size effects, differences in Sr, Nd and Pb isotopic compositions of the same samples between clay (<2µm) and silt (>2µm) fractions from the Irrawaddy delta (Giosan et al., 2018) were analyzed (Fig. 3.3). The clay size Irrawaddy show systematically more radiogenic Nd isotope signatures than the silt size samples (a difference of 2 εNd units reaching up to 2.5 εNd units, samples), while the Sr isotope signatures do not differ significantly (up to 0.0057 higher values in the clays than in the silt fraction) (Table A2). The Pb isotope signatures are systematically more radiogenic in the silt fraction (0.1-0.2 higher $^{206}Pb/^{204}Pb$ ratios and 0.2-0.4 higher $^{208}Pb/^{204}Pb$ ratios) than in the clays (Table A4).

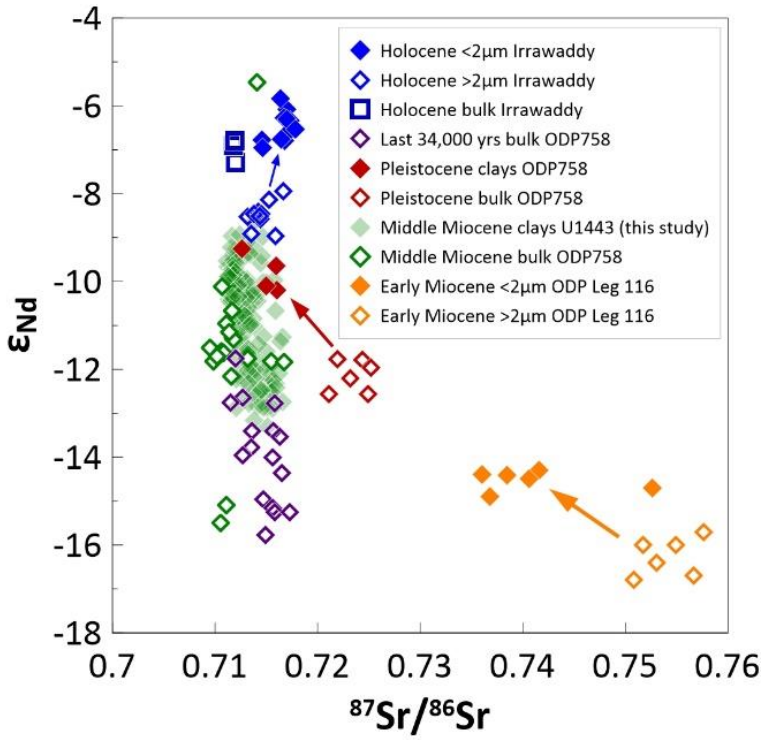

Fig. 3.3: Grain size dependence of the radiogenic Sr and Nd isotope composition, comparing the clay (<2µm) and bulk or >2µm fraction of sediments from the Holocene Irrawaddy River (blue, Giosan et al., 2018, and this study), the last 34,000 years of ODP Site 758 (purple, Ahmad et al., 2005), Pleistocene of ODP Site 758 (red, Ali et al., 2021; Gourlan et al., 2010), middle Miocene of ODP Site 758 and U1443 (green, Banerjee et al., 2019 and this study), and early Miocene sediments of the distal Bengal Fan (orange, Galy et al., 1996).

3.4 Discussion

3.4.1 Provenance control on the U1443 detrital clay isotope signature

Figures 3.4 and 3.5 compare the Nd-Sr and Nd-Pb isotope compositions of the U1443 clays with those of potential source areas surrounding the Bay of Bengal and the sediments sampled in the major rivers. Of the Himalayan sources, the TPB signature is almost identical to that of the IBR and is already included in the Brahmaputra sediment signatures as it is fed by the Yarlung-Tsangpo River which drains the TPB. It is therefore not considered as an independent endmember. The wide exposure of the TPB and the TSS rocks within the drainage basin of the Yarlung-Tsangpo is the main reason for the difference in isotope signatures between the Ganges, with only very sparse coverage of TSS for upper and already arid regions of its watershed, and Brahmaputra sediments and the large range of Brahmaputra compositions. Since other potential contributors of radiogenic Nd such as the Deccan Traps or the Sunda Arc (Fig. 3.4a) are considered negligible (see discussion below), the IBR is considered the dominant contributor of sediments with radiogenic Nd and unradiogenic Sr isotope values. In contrast to the NER samples, Bengal Fan silicates with a similar age to ours clearly overlap with HHC signatures (Fig. 3.4a, e.g., France-Lanord et al., 1993; Galy et al., 2010) and lack the IBR influence. Nevertheless, the large scale changes are similar to the

ones observed at the NER (Ali et al., 2021). Hemipelagic sediments from the Bengal Fan plot much closer to our samples (Fig. 3.4a) and were interpreted to contain significant IBR contributions (Galy et al., 2010), indicating that the NER clay radiogenic isotope compositions represent the fine-grained sediment supplied to the central basin. The overlap of our clay results with bulk detrital measurements from the same location (Figs. 3.3 and 3.4a; Banerjee et al., 2019) confirms that they originate from the same sources and that grain size dependent fractionation of the isotope compositions did not have a significant impact on the reconstructed mixing relationships between the main source areas. The grain size effects are small compared to the isotopic range of source areas and therefore it is reasonable to relate the clay results to bulk sediment data.

In addition to the sediments supplied by major rivers, fine-grained mineral dust, for example from the Thar desert, may have contributed to the U1443 clay isotopic composition. However, the calculated annual mineral dust input of ~0.3-6 g m^{-2} yr^{-1} to the Bay of Bengal (extrapolated to the surface area of the Bay of Bengal, the annual mineral dust input corresponds to a maximum of ~13 Mt yr^{-1}; Srinivas & Sarin, 2013) is minor (~1 %) compared to the 1300 Mt yr^{-1} of sediments supplied by the Ganges, Brahmaputra and Irrawaddy Rivers (Fig. 3.1; Milliman and Syvitski, 1992) and is therefore considered negligible.

Due to the movement of the Indian Plate, Site U1443 was located at least 800 km further south, at ~2°S during the middle Miocene. However, tectonic reconstructions suggest that the location of the Himalayas and the Indian Peninsula relative to the NER have remained the same since the Oligocene/Miocene (Hall, 2012; Zahirovic et al., 2016). Given the invariant distance from the Himalayas, the plate motion most likely did not affect the source contributions of clays reaching the core location. Instead, the advancing Himalayan sediments rapidly filling basins now on land and feeding the growing Bengal and Nicobar fans likely influenced sediment accumulation on the NER (e.g., McNeill et al., 2017). The evolution of Sundaland to the east was more complex (e.g., Zahirovic et al., 2016) but the lack of volcanic detritus in the Nicobar Fan (Pickering et al., 2020) suggests that the Sumatra magmatic arc was only a minor contributor throughout the middle Miocene. Moreover, over the last 30 Myr repeated flooding and exposure of the shelf seas around Sumatra (Zahirovic et al., 2016) should have strongly affected the sediment supply from this source, which is not consistent with the overall near stable source contributions recorded in our U1443 clays. The influence of sources from the Indian Peninsula, like the Deccan Traps or Archean terranes is also considered to be minor (Ali et al., 2021; France-Lanord et al., 1993). Deccan Trap isotope compositions of the younger and more voluminous flows display highly radiogenic Nd and unradiogenic Sr and Pb isotope compositions (Figs. 4a & 5a; e.g., Lightfoot et al., 1990), while Archean Terranes are characterized by extremely unradiogenic ε_{Nd} signatures (Fig. 3.4a; Kessarkar et al., 2005; Peucat et al., 1989), thus both being distinct from our clay isotope compositions. Although mixing between the Archean Indian Peninsula and the IBR endmembers could produce

the isotope composition of the U1443 clays, this is not reasonable given that this would require 20 to 50 % contributions from Archean Indian continental sources. This is highly unlikely for a number of reasons. First, the Krishna and Godavari Rivers draining the Indian Peninsula reflect a combined signature of the Indian Peninsula sediments (Fig. 3.4b), which can neither account for the more radiogenic ε_{Nd} isotope compositions nor the low $^{87}Sr/^{86}Sr$ signatures of our samples. Secondly, the supply of material from these sources by the Krishna and Godavari Rivers was likely restricted to the Indian margin due to the monsoon-induced Indian coastal current (Ali et al., 2021; Kumar et al., 2006). The east-west divide of isotope compositions in surface sediments from the Bay of Bengal (Colin et al., 1999) corroborates the fact that Peninsula river sediments are restricted to the western Bay of Bengal. Additionally, their sediment load is minor compared to that of the major rivers (Fig. 3.1) and sediments recently deposited on the NER have a composition similar to those deposited in the Miocene (Fig. 3.3). Consequently, we are confident that the dominant sources supplying clays to the NER are the Himalayan and IBR sources in the north.

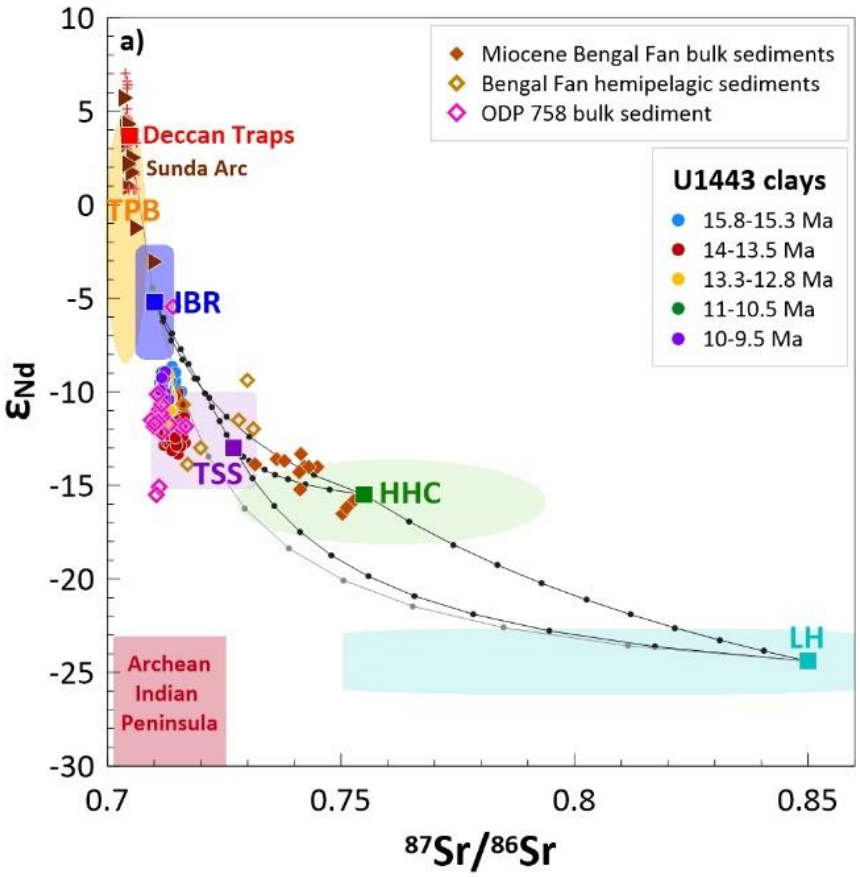

Fig. 3.4: (a) Nd-Sr isotope composition of the clay size fraction of Site U1443 compared with published data. Miocene Bengal Fan bulk sediments (Galy et al., 2010), Bengal Fan hemipelagic sediments (Galy et al., 2010; Hein et al., 2017) and ODP 758 bulk sediments (Banerjee et al., 2019) are plotted for comparison. Potential sources include the different Himalayan lithologies (Transhimalayan Plutonic Belt - TPB, Tethyan Sedimentary Series - TSS, High Himalayan Crystalline - HCC, and Lesser Himalayas - LH), the Indo-Burman Ranges (IBR), the Deccan Traps, the Archean Indian Peninsula, the Sunda Arc and the rivers draining these lithologies – Irrawaddy, Ganges, and Brahmaputra (squares). References are listed in Table 3.1.

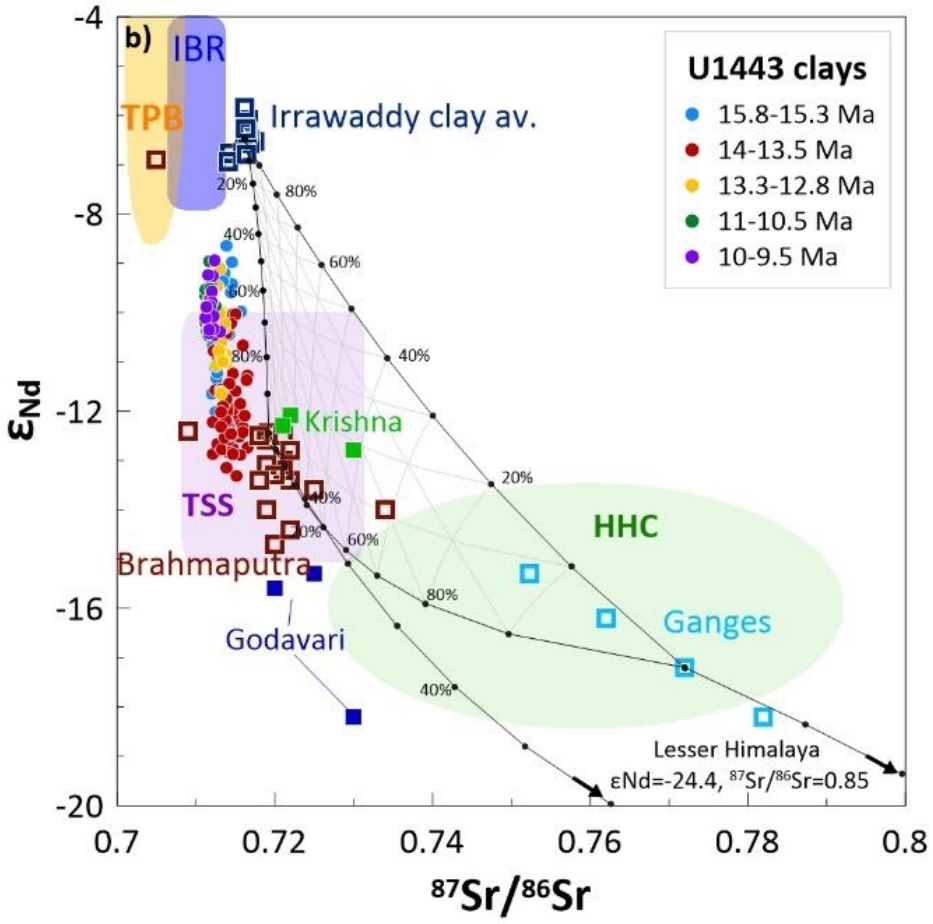

Fig. 3.4: (b) Nd-Sr isotope composition of the clay size fraction of Site U1443 compared with published data. Average values of the three major rivers are used as endmembers to define a mixing field. The grid was calculated according to a 10 % increment of the mixture composition using the compositions listed in Table 3.1. U1443 clays do not plot within the mixing field but show a binary mixing trend between the Irrawaddy and the Brahmaputra Rivers.

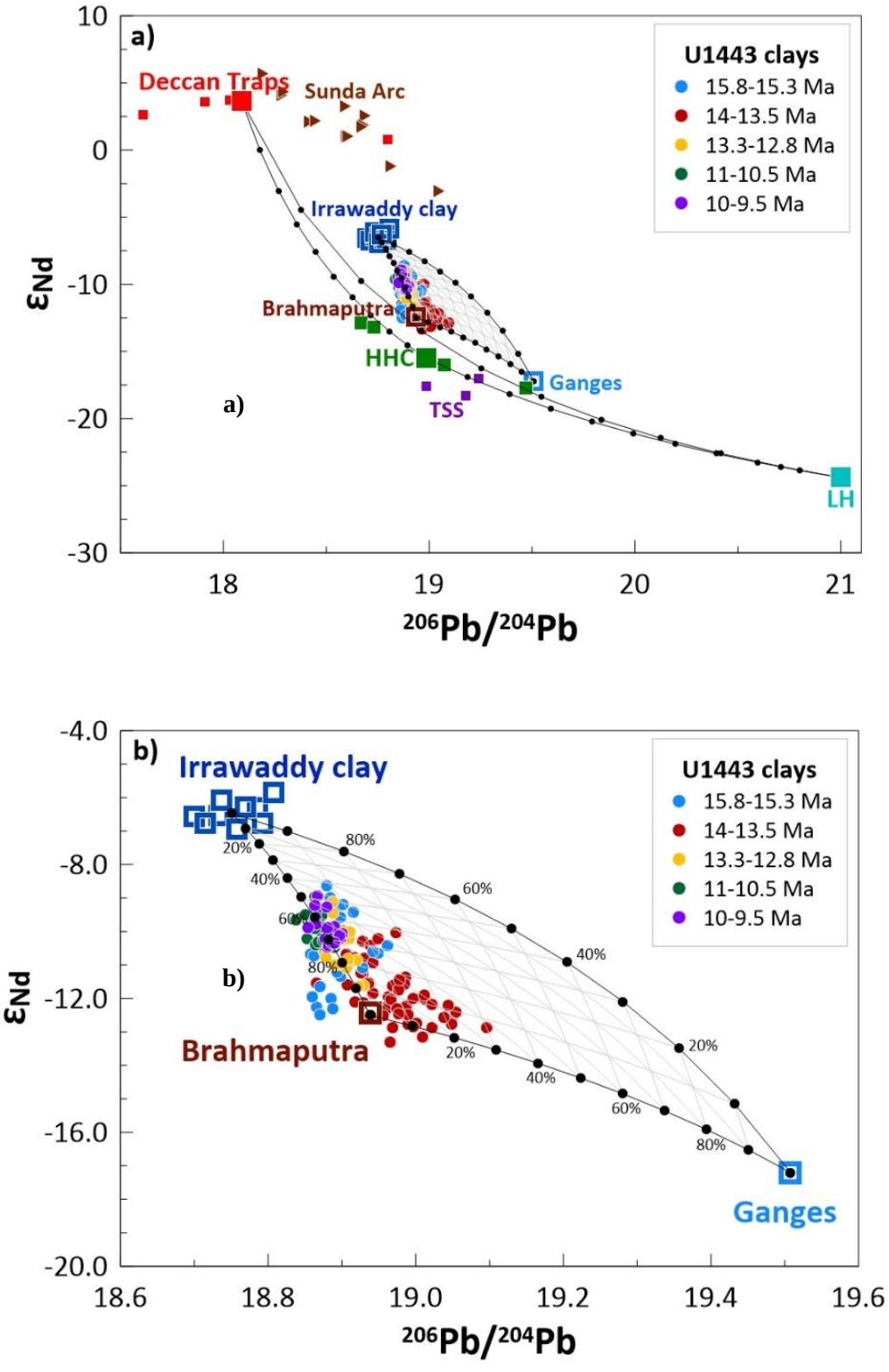

Fig. 3.5: (a) Nd-Pb isotopic composition of U1443 clays compared to the potential sediment sources, represented by Deccan Traps, Sunda Arc, TSS, HHC and LH average compositions as well as the Irrawaddy, Ganges, and Brahmaputra Rivers (squares, references in Table 3.1). (b) Expanded view of mixing field spanned by the three major rivers used as endmembers. The grid was calculated according to a 10 % increment of the mixture composition. The U1443 clays show a dominant contribution of Irrawaddy and Brahmaputra sources.

Table 3.1: Literature Sr, Nd, and Pb average isotopic compositions and concentrations for the major lithologies and river systems used as endmembers.

Endmember	$^{87}Sr/^{86}Sr$	Sr (ppm)	ε_{Nd}	Nd (ppm)	$^{206}Pb/^{204}Pb$	$^{208}Pb/^{204}Pb$	References
IBR	0.71	200	-5.2	24			Awasthi et al. (2014)
TSS	0.727	229	-13	26.7			France-Lanord et al. (1993)
HHC	0.755	70	-15.5	23.6			France-Lanord et al. (1993); Singh and France-Lanord (2002)
LH	0.85	70	-24.4	40.3	21		Singh and France-Lanord (2002); Clift et al. (2002)
TPB	0.705	400	-6.5				Singh and France-Lanord (2002)
Deccan Traps	0.705	228	3.67	11	18.088		Lightfoot et al. (1990); Mahoney et al. (1982); Tripathy et al. (2011)
Archean Indian Peninsula	0.716		-25				Kessarkar et al. (2005); Peucat et al. (1989)
Sunda Arc	0.705		1.97		18.565		Gasparon and Varne (1995)
Irrawaddy	0.716	100	-6.47	50	18.751	39.098	Awasthi et al. (2014); this study
Brahmaputra	0.719	212	-12.5	35.6	18.938	39.571	Singh and France-Lanord (2002); Millot et al. (2004)
Ganges	0.772	32	-17.2	23.6	19.508	39.766	Singh and France-Lanord (2002); Millot et al. (2004)
Godavari	0.725		-16.4				Ahmad et al. (2009)
Krishna	0.724		-12.4				Ahmad et al. (2009)

The Pb isotope composition provides additional constraints on the sources of the clay size sediments. Fig. 3.6 shows the U1443 clays together with typical fluvial sediments representing the catchment areas. Consistent with the Nd-Sr isotope relationships, our Pb isotope data indicate that the samples reflect a mixture of more radiogenic Himalayan sources represented by Ganges and Brahmaputra sediments and less radiogenic sources from the IBR represented by the Irrawaddy sediments. However, the estimated mixture percentages differ from those based on the Nd-Sr calculations, with a ~20 % higher Irrawaddy endmember contribution.

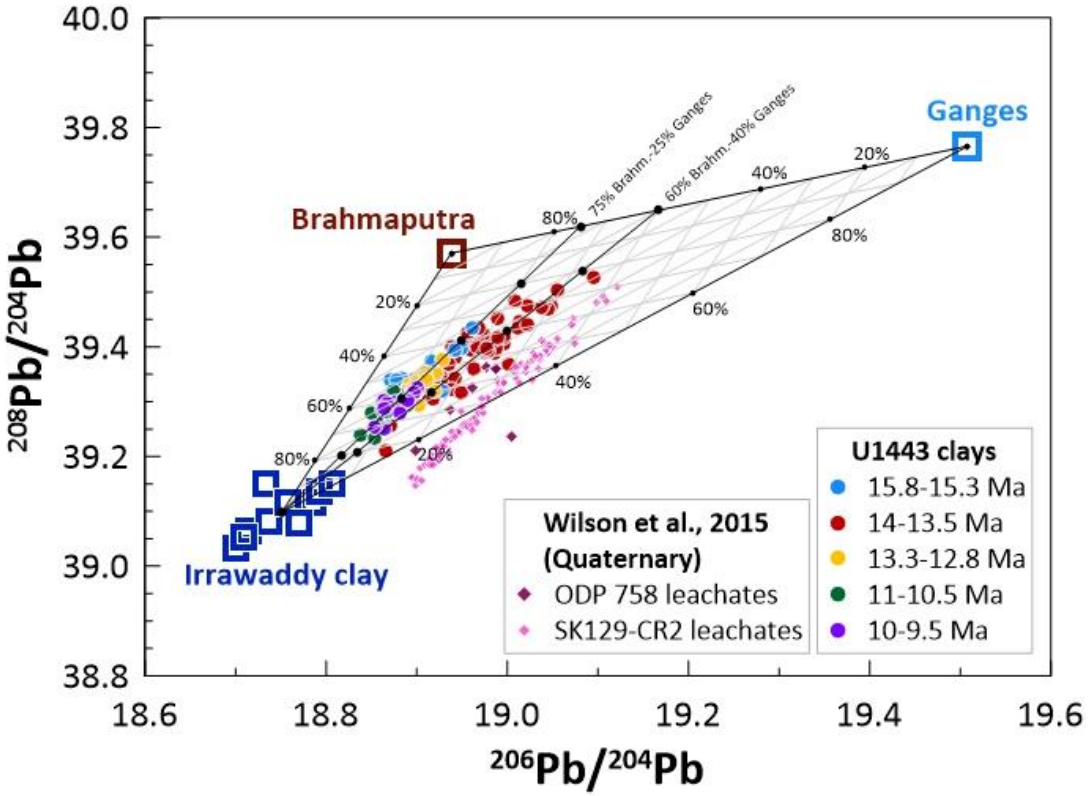

Fig. 3.6: Pb isotopic composition of U1443 clays compared to Quaternary Indian Ocean leachate data (Wilson et al., 2015) and potential sources represented by the Irrawaddy, Ganges, and Brahmaputra Rivers (squares, references in Table 3.1). The three major rivers are used as endmembers to span a mixing field. The grid was calculated according to a 10 % increment of the mixture composition. U1443 clays plot within the mixing triangle, suggesting a mixture of source contributions. Two binary mixing lines between the Irrawaddy endmember and two Brahmaputra-Ganges mixtures show the binary mixing trend of the clays.

To better constrain the different source contributions, we calculated binary mixing relationships between the most likely endmembers (Table 3.1) and added ternary mixing grids to Figures 3.4b, 3.5 and 3.6. Since data for all three isotope systems exist for most of the river sediments in contrast to the major lithologies, we applied average Irrawaddy clay, and average bulk Brahmaputra and Ganges sediment isotopic signatures as mixing endmembers (Figs. 3.4, 3.5, 3.6). The Sr-Nd mixing plot shows that the U1443 clays do not fall into the field spanned by Irrawaddy, Brahmaputra and Ganges sediments (Fig. 3.4). While ε_{Nd} values plot almost on a line between the Irrawaddy and Brahmaputra, indicating up to 60 % Irrawaddy and 40-100 % Brahmaputra contributions, the $^{87}Sr/^{86}Sr$ isotopic signatures are shifted towards more unradiogenic Sr values and do not overlap with any mixing trends between the three endmembers. Given that contributions from seawater Sr are minimal (see Ali et al., 2021), and similar values are found for the bulk detrital data from ODP Site 758 (Fig. 3.3) the most likely explanation for the observed shift is that the average river isotope compositions used as endmembers are not well constrained. The river endmembers are derived from modern day bulk river sediments (Galy and France-Lanord, 2001; Giosan et al., 2018; Singh and

France-Lanord, 2002) but their isotopic compositions may have varied over the last 16 Myr. Furthermore, the spread in values of measured river sediments, especially for the Brahmaputra River, is large. Therefore, it is possible that the actual source endmembers of our clays in the Miocene had less radiogenic Sr isotopic signatures than the average values applied as endmembers. Additionally, Sr isotopes are known to be influenced by grain size fractionation and weathering effects (Blum and Erel, 2003; Derry and France-Lanord, 1996), which is consistent with previous work in the region that has shown detrital Sr isotopes to vary, while Nd isotopes suggest a constant source (Ali et al., 2015; Colin et al., 1999).

We thus consider the mixing relationships of the Pb-Pb and the Nd-Pb isotope system (Figs. 3.5b & 3.6) more appropriate to reflect changes in the source contributions of the clays. The plots clearly show that all three endmembers contributed to the NER clays. There is a clear difference between the youngest intervals (11-10.5 and 10-9.5 Ma), exhibiting little variability in source contributions (<25 %) and a Ganges contribution of <10 %, and the two intervals between 15.8 and 13.5 Ma. By far the largest variability in source contributions (up to 60 %) is found for the interval comprising the major cooling step at ~13.9-13.8 Ma (14-13.5 Ma). Interestingly, the samples define binary mixing trends between the Irrawaddy endmember and a rather constant Ganges-Brahmaputra mixture. The Nd-Pb isotope plot shows an almost pure Brahmaputra-Irrawaddy mixing line for all intervals except the 14-13.5 Ma interval, which shows a Ganges contribution for the Ganges-Brahmaputra endmember of 10-20 %. These lower Ganges contributions agree with observations of Galy and France-Lanord (2001), who found a higher modern sediment flux from the Brahmaputra compared to the Ganges. During the Miocene, the Ganges contribution was also likely diminished by changes in the routing of the rivers as documented by differences in the composition of sediments in the Nicobar and Bengal fans (Chen et al., 2020b). In the Pb-Pb isotope space, most samples plot on the mixing line between the Irrawaddy and a 75 %-Brahmaputra–25 %-Ganges endmember. In agreement with the Nd-Pb isotope plot, the 14-13.5 Ma interval points to a Ganges-Brahmaputra endmember with higher Ganges contribution, in this case ~40 %. Even though the percentages do not match precisely for Nd and Pb isotopes, the trend of a higher Ganges contribution during the 14-13.5 Ma interval is clear. A possible explanation for the differences may be the known influence of weathering on clay Pb isotope signatures (e.g., Erel et al., 1994; Harlavan and Erel, 2002). Across the investigated Miocene time interval, we observe a marked change in the overall balance of the sources from relatively low Irrawaddy and high Brahmaputra and Ganges contributions prior to 13.5 Ma to higher amounts (by ~20 %) of Irrawaddy material delivered thereafter (Fig. 3.2).

The radiogenic Sr, Nd, and Pb isotope compositions of the clays transported to the southern Bay of Bengal suggest that the different erosional sources have overall supplied clays during the Miocene in a remarkably consistent manner, considering the major tectonic reorganizations in the Himalayas

(Ali et al., 2021). This mixture was enriched in material originating from formations with more radiogenic Nd isotope compositions (i.e. the IBR) where the monsoon rains are strongest today (Damodararao et al., 2016). Our new high resolution data, however, reveal periods of source variability of up to 60 % which were not captured by the lower resolution study of Ali et al. (2021) (Fig. 3.2).

3.4.2 Tectonic and climatic control on the long-term radiogenic isotope evolution of clays during the Miocene

On long timescales, our data document that the sources of sediments remained remarkably stable throughout the middle and early late Miocene. This is in agreement with previous Sr and Nd isotope records from the distal and central Bengal Fan spanning the last 17 Myr (France-Lanord et al., 1993) and the last 12 Myr (Galy et al., 2010), as well as the low-resolution record for the last 27 Myr from Site 758 (Ali et al., 2021). The evolution of the radiogenic isotope record between 17 and 9 Ma at Site 758 is overall consistent with our data (Fig. 3.2). The Site 758 data generally plot at the less radiogenic end of the spectrum of our records for $^{206}Pb/^{204}Pb$ and $^{87}Sr/^{86}Sr$, and at the more radiogenic end for ε_{Nd} values. The higher resolution data of our study exhibit much higher variability and document increased contributions from the Himalayas (up to 20 % more Ganges, up to 40 % more Brahmaputra contribution). The difference between the two records may also, at least partly, originate from differences in leaching or dissolution techniques in the two studies. A weaker leaching prior to dissolution of the clay-size minerals applied by Ali et al. (2021) may have left some seawater-derived authigenic signatures in the low resolution data, while the alkaline fusion technique employed here is more likely to dissolve all refractory minerals than simple mixed acid digestion at low pressure (Bayon et al., 2009a). Generally, the warmer intervals are marked by a much higher variability in all three isotope systems and by relatively higher Himalayan contributions additionally to IBR dominated samples. The colder intervals show a lower isotopic variability and contributions generally dominated by the IBR. This change occurred directly following the major global Miocene cooling, at ~13.9-13.8 Ma (Fig. 3.7). One possible driver of this shift is therefore a change in global climate, but how could climate cooling have caused this change in radiogenic isotope variability? Warmer climates were, if similar to Holocene observations (e.g., Galy et al., 2008; Li et al., 2018), associated with a stronger land-sea surface temperature contrast, resulting in a strengthening of summer monsoon circulation and an enhanced atmospheric water vapor transport. The higher availability of water in the atmosphere during warmer intervals may then have led to increased penetration of monsoon precipitation into the high mountain areas, possibly overcoming the existing main orographic barrier (the High Himalayas), thus enabling more intense erosion in formerly arid plateau regions and higher contributions of High Himalayan (HHC) material. Climate-tectonic interactions can produce feedbacks in both directions (Clift and Webb,

2018). Since rainfall follows topography, higher erosion in highlands result from both strong precipitation and steep topography. More erosion fosters exhumation, which drives more uplift and higher topography can focus more precipitation. Therefore, the tectonic evolution of the Himalayas also needs to be included in the interpretation of the data on longer timescales.

Considering the major tectonic reorganization of the Himalayan orogenic wedge during the middle Miocene (e.g., Hodges, 2000; Vannay et al., 2004; White et al., 2002; Yin, 2006), it is remarkable that the average mixture of sediment sources deposited at Site U1443 remained consistent throughout the investigated time window. However, the marked decrease in variability in all three radiogenic isotope systems was too rapid to be related to those large tectonic changes. During the early-middle Miocene, the deformation of the wedge was dominated by the frontal accretion and mid crustal extrusion of HHC rocks between two major shear zones, the Main Central Thrust (MCT) to the south and the Southern Tibetan Detachment System (STDS) to the north (e.g., Hodges, 2000, and ref. therein). Rocks from the MCT hanging wall, comprising HHC and TSS, were exhumed and eroded (Vannay et al., 2004; White et al., 2002). Thereafter, during the middle Miocene, the thrusting propagated south from the MCT, shifting the exhumation to the Lesser Himalayan (LH) units, while the exhumation of the HHC and TSS slowed down (Colleps et al., 2019; Najman et al., 2009). Still, High Himalayan lithologies covered large parts of the Himalayas. The LH units, covering the Indian craton, underthrusted the Himalayan wedge, accreted and formed the LH-duplex. These processes shifted the main orographic barrier southward from within the Lhasa Block to its current position in the High Himalayas (Tremblay et al., 2015). This shift likely had a large impact on which rocks were exposed to erosion. The exact timing of the tectonic changes is difficult to constrain, but most studies agree on a peak time of rapid exhumation of the HHC, TSS and TPB at ~17-16 Ma (Carrapa et al., 2014; Colleps et al., 2018; Tremblay et al., 2015), while the timing for the slowdown of exhumation varies between ~16 Ma (Najman et al., 2009) and ~10 Ma (Tremblay et al., 2015). One way to explain those different ages is the locally restricted sampling of these studies, whereas our record provides an integrated signal of the different sediment sources in the catchment areas of the rivers. Before this tectonic reorganization, a mixture of TSS and HHC rocks were dominantly eroded. The two intervals prior to 13.5 Ma include higher $^{87}Sr/^{86}Sr$ and lower ε_{Nd} values than the subsequent intervals, typical for more High Himalayan-influenced sources. The main orographic barrier was positioned further north, which would have enabled high erosion rates across the Indus-Tsangpo suture zone and the southern Tibetan Plateau and a steeper and very erosive drainage network across the Himalayas (Tremblay et al., 2015; White et al., 2002). Moreover, under these conditions, Tremblay et al. (2015) also expect a wetter precipitation regime on the southern Tibetan Plateau, which drove large-scale erosional exhumation. This is in agreement with thermochronological data of Carrapa et al. (2014) that document the removal of large volumes of rock from the suture zone within a few million years. This can only be

accomplished by sufficient precipitation, efficient river incision and enhanced sediment transport due to an intensified SAM across these internal parts of the mountain belt during and around the MCO.

The tectonic reorganization, including the southward propagation of the thrusting and the accompanied southward shift of the orographic barrier, as well as the decrease in High Himalayan exhumation, restricted the erosion of Himalayan source rocks. The reorganization of the drainage system most likely resulted in a much smoother channel slope and thus in decreasing stream power. Moreover, due to the southward shift of the orographic barrier, the precipitation no longer reached the interior of the southern Tibetan plateau and aridity increased. The decrease in stream power and the increase in aridity probably resulted in the shutdown of erosion in Southern Tibet, which Tremblay et al. (2015) considered to have happened at the latest around 10 Ma. The shutdown of intense erosion is documented by the low variability and the decrease in Himalayan source contributions in the U1443 record after 13.5 Ma, thus considerably earlier than the estimated age of Tremblay et al. (2015). As mentioned before, this could be due to the integrated sediment signal of Site U1443 in contrast to the local study of Tremblay et al. (2015). After the erosion of the MCT hanging wall units, erosion of LH units, as part of the exhuming LH-duplex after the reorganization, would be expected (Colleps et al., 2018). However, there is a complete lack of LH signatures (Fig. 3.4, $\varepsilon_{Nd}\approx$-24.4, $^{87}Sr/^{86}Sr\approx0.85$; Singh & France-Lanord, 2002) in our record, as well as in Miocene Bengal Fan records (France-Lanord et al., 1993; Galy et al., 1996), implying no extensive weathering and supply of these lithologies as clays. A possible explanation for the missing signal of the LH is that LH units are much more dominant in the central Himalayas drained by the Ganges, while they are hardly exposed in the eastern part (Fig. 3.1), which is the major watershed of the Brahmaputra. Our provenance estimates clearly indicate a dominance of Brahmaputra over Ganges contributions for the Himalayan component, which can at least partly explain the absence of LH influence across the east. The continued supply of HHC, TSS and TPB derived material following the mid-Miocene shutdown of strong erosion of these terrains suggests that these sources were weathered to form clay minerals in deposits such as those forming the IBR.

The decrease in variability of the radiogenic isotope signatures at 13.5 Ma closely followed the Miocene cooling (major cooling step at ~13.9-13.8 Ma) documented by the benthic $\delta^{18}O$ record and occurred abruptly within only ~200 kyr (Fig. 3.7). This geologically short time period argues for a coupling of climate and erosion and implies that tectonics were not the main driver of this change. Both, vigorous erosion accompanied by rapid sediment transport and deposition of organic material with clastic sediments across the mega fans, as well as chemical weathering of Himalayan material, may have contributed to CO_2 drawdown and thus to the global cooling throughout the Cenozoic. Simultaneously, the cooling climate, whether supported by Himalayan erosion or not, likely had a huge impact on precipitation patterns. While strong precipitation appears to have reached deeper

into the High Himalayas during the warm period around the MCO, its geographic extent was likely decreased with the cooling and focused on the frontal domain of Himalayan orogenic belt. The orographic barrier of the High Himalaya during cooler climate became active in preventing precipitation from reaching the high elevations and distal (from the moisture source) parts (including HHC and TSS) of the southern Tibetan Plateau margin. In turn, without strong erosion, exhumation would be diminished, which is supported by the slowdown in exhumation and erosion of the High Himalayas, the Tethyan Himalayas, the suture zone region and the southern Lhasa Block sometime between 17 to 10 Ma (Najman et al., 2009; Tremblay et al., 2015; White et al., 2002). The increase in sediment flux to the NER following the middle Miocene cooling, as inferred from the study by Hovan and Rea (1992; re-calculated by Ali et al., 2021; Fig. 3.2), seems contradictory to the decrease in High Himalayan erosion. However, the increase in sediment flux might only reflect the progradation of the accumulating Bengal Fan, with suspension transport reaching the top of the NER (Ali et al., 2021). This in turn can be questioned due to the evidence of simultaneous increases in sedimentation at nearby drill sites on the Bengal Fan (Ali et al., 2021). Furthermore, the climatic and/or tectonic changes did not necessarily lead to a general decrease in erosion within the watersheds supplying the Bay of Bengal. Instead, they altered the precipitation pattern and the locus of maximum erosion to more frontal and southern domains of the Himalayas as well as to the present-day LH, which was still mainly covered by High Himalayan thrust nappes during the middle and late Miocene. The focus of monsoonal rains shifted to lower altitudes along the southern Himalayan front, as seen today (Bookhagen et al., 2006) and to the IBR, hence eroding and weathering more material with less radiogenic Sr and Pb and more radiogenic Nd signatures, as reflected by our record. Therefore, the increased sediment delivery to the fans and NER during the Miocene could simply be the result of the shorter transport distance for the sediments derived from the frontal domains of the Himalayas compared to material travelling the distance across the entire orogenic belt. The increase of the primary clay mineral illite during the cooling suggests an increase in physical erosion, which may have been associated with increased aridity in the colder climate (Ali et al., 2021). This also hints at the focus of precipitation on the IBR after the cooling, since the Irrawaddy River does not have an extensive floodplain, as opposed to the Indo-Gangetic plain (Joussain et al., 2016; Li et al., 2018), an environment in which intense chemical weathering producing secondary clay minerals takes place. Ali et al. (2021) interpreted the increase of the primary clay mineral supply accompanied by only subtle changes in the mixture of the source rocks being weathered as resulting from a shift in the weathering regime. This shift during the middle Miocene global cooling likely resulted from the development of the dry NE winter monsoon season (Ali et al., 2021), similar to what had been inferred for the late Miocene in East Asia (Holbourn et al., 2018).

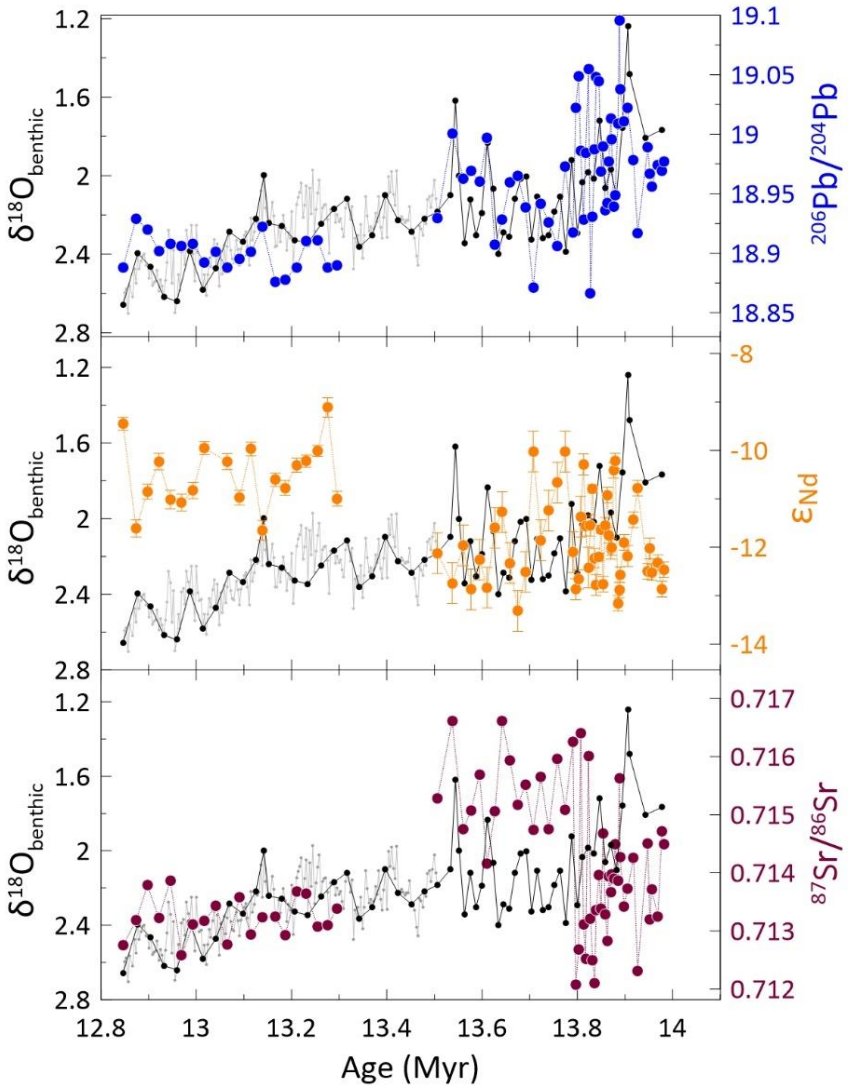

Fig. 3.7: Radiogenic Pb, Nd and Sr isotope compositions of U1443 clays compared to the benthic δ18O signal over the major middle Miocene cooling at ~13.9-13.8 Ma. The black dots and lines represent a low resolution (~40 kyr) benthic $\delta^{18}O$ record. The grey dots and lines in the younger part from 13.5 to 12.8 Ma show the higher resolution (~5 kyr) benthic $\delta^{18}O$ record of Lübbers et al. (2019). The variability of the radiogenic isotopic composition decreases for all three isotope systems after the cooling event. The Pb isotope variations closely follow the benthic δ18O curve in the older part until 13.5 Ma.

3.4.3 Climatic control on source contributions and the weathering regime of the Bay of Bengal catchment areas causing fluctuations of radiogenic isotopes on orbital timescales

The reversible nature of the short-term fluctuations means that they cannot have been caused by tectonics, given that major tectonic reorganizations only occur on longer (Myr) timescales and are generally unidirectional. The changes in isotopic compositions within the individual Miocene time intervals occurred on orbital timescales of a few to tens of thousands of years (Figs. 3.2 & 3.7).

Spectral analyses of the high-resolution ε_{Nd} data obtained between 14 and 13.5 Ma with a much higher average sampling resolution than ~10 kyr and consequently smaller aliasing errors, document a significant ~30 kyr cyclicity with additional contributions of the ~100 kyr eccentricity

(Fig. 3.8; for more details, see also Supporting Information). Although not as pronounced, a ~30 kyr cyclicity (> 80 CI) is also apparent in the Pb isotope data (not shown) but we did not find a similar periodicity in the $^{87}Sr/^{86}Sr$ data. This ~30 kyr periodicity is most likely a heterodyne produced by interaction of the three major orbital cycles and is commonly observed in late Quaternary paleoceanographic and paleoclimatic records of the South (e.g., Chen et al., 2020a; Gebregiorgis et al., 2018) and East Asian monsoon domains (e.g., Beaufort et al., 2003; Clemens et al., 2018; Sun et al., 2010). A ~30 kyr periodicity was also observed in planktonic oxygen isotopes reflecting surface ocean conditions in the South China Sea during the middle Miocene (Holbourn et al., 2010). In the late Quaternary, this heterodyne reflects the non-linearity of the monsoon strength vs. external insolation relationship and the fact that this is the strongest periodicity found in the middle Miocene data suggests this may reflect the strongest monsoon variations resulting in fluctuations in clay provenance. A strong precession signal has been observed in clay mineralogy variations of late Quaternary sediments from the Bay of Bengal (e.g., Colin et al., 1999; Colin et al., 2006) and although the resolution of the mid-Miocene clay isotope data is generally not sufficient to resolve precession, there is a hint of a signal (>80% CL) in the Nd isotope data (Fig. 3.8). Although only possible for the interval with the highest resolution data, these analyses suggest that the high frequency variability in the mixture of clay sources was related to changes in monsoon strength during the middle Miocene.

Since no other orbital-scale resolution Miocene records for radiogenic isotopes exist, we compare our record to Late Quaternary glacial-interglacial records that exhibit changes of radiogenic isotopic compositions of similar range and on comparable timescales to ours (Fig. 3.6 & 3.9). The Pb isotope record of the authigenic sediment fraction representing dissolved deep Indian Ocean water signatures from the NER and the Central Indian Ocean of the last 250 kyr of Wilson et al. (2015) shows a range of Pb isotopic signatures very close to the ones in our detrital record (Fig. 3.6). The variations in Pb isotopes show enhancement of Himalayan contributions by a factor of two to three during interglacial periods. The shifts in source contributions were attributed to changes in regional weathering intensity (Wilson et al., 2015). Cyclic changes in radiogenic isotopic compositions of the bulk silicate fraction from turbiditic Bengal Fan sediments during the last glacial and transition to the Holocene (Joussain et al., 2016; Li et al., 2018), were attributed to sea level changes and to changing surface currents responding to monsoon intensity and resulting changes in detrital supply. Moreover, a stronger summer monsoon during warmer climates (e.g., Galy et al., 2008; Li et al., 2018) may not only influence the source contributions on long timescales as discussed above, but also on short timescales. Increased precipitation over the high mountain areas likely provided higher contributions of High Himalayan material during warmer climatic episodes.

It has been suggested that the strengthening of surface currents in the Bay of Bengal associated with monsoon intensification controlled the deposition of detrital inputs (Ahmad et al., 2005; Joussain

et al., 2016; Li et al., 2018). Enhanced IBR source dominance within the short-term fluctuations may thus be explained by a weakening of the summer monsoon and a stronger winter (NE) monsoon. This may have become particularly important following intensification of the winter monsoon during the major cooling at ~13.9-13.8 Ma (Ali et al., 2021). Stronger NE winds likely started to drive counter-clockwise currents within the Bay of Bengal, increasing the transport of sediment from the Irrawaddy River to Site U1443 (Rao et al., 2005). Such an interpretation was also favored by Ahmad et al. (2005), who recorded pulses of less radiogenic Sr (-0.003 in $^{87}Sr/^{86}Sr$) and more radiogenic detrital Nd isotope values (+1.4 ε_{Nd} units) associated with higher silt abundances during Heinrich intervals linked to an enhanced NE monsoon. Joussain et al. (2016) and Li et al. (2018) also found decreases in ε_{Nd} values (~2 ε_{Nd} units) in interglacials and the Holocene, respectively, compared to glacial periods, which, among other factors, were attributed to changing surface currents. An increase in the transport of Himalayan material to the NER during periods of a stronger summer monsoon and associated strengthened currents coming from the SW is not quite so obvious. However, it is plausible that during enhanced summer (SW) monsoon, the mixing of sediments within the Bay of Bengal was stronger, with clockwise surface currents picking up larger amounts of Himalayan material and transporting it to the NER than during times of dominant winter monsoon. If the same mechanisms apply to the clay distribution, a doubling of Himalayan input during times of enhanced summer monsoon can account for most of the variations in our clay record. However, the glacial-interglacial changes may be mainly attributable to differences in grain size contributions. Higher silt supply during glacials does not necessarily imply higher clay supply. Clays stay in suspension until they are removed by ballasting, and by the time they would get to the NER, the clay's radiogenic isotope signal should be well mixed. Therefore, transport processes should only play a minor role in influencing our clay isotope record.

In addition to changing surface currents, Joussain et al. (2016) and Li et al. (2018) also attributed changes in sediment contribution to the sea level rise and fall between glacials and interglacials. The presence of eccentricity cycles in the record (Fig. 3.8) points to a sea level influence on the Nd isotope composition, even though this was probably not the primary driver. The middle Miocene sea level was likely ~55 to 75 m higher than today (e.g., John et al., 2004; Miller et al., 2020; Miller et al., 2005) and differed even more from Later Quaternary glacial sea level. Therefore, we cannot simply transfer the glacial-interglacial sea level conclusions to the radiogenic isotope excursions apparent in our Miocene record. Nevertheless, sea level variations of ~20 m (Miller et al., 2020; Miller et al., 2005) between warmer and colder episodes of the Miocene would have significantly influenced the extent of the floodplains, the areas where the majority of the secondary clay minerals (which clearly dominate over the primary clay minerals, Fig. 3.2) formed and where sediment was stored. Hence, sea level changes might not have significantly influenced transport pathways in the Miocene, which, as discussed above, should not have a major influence on the clay isotope

signatures, but it would have controlled the storage and chemical weathering of the sediments and, consequently, which sediments eventually were supplied to the NER.

The processes discussed above can explain the range and changes of the radiogenic isotope compositions of the U1443 clays. This is primarily true for Nd and Pb isotope variability, which almost exclusively originates from mixing of the source endmembers. The fact that ε_{Nd} and $^{87}Sr/^{86}Sr$ do not correlate well within the individual time intervals investigated (Fig. 3.9) and that no orbital cycles are present in the Sr isotope record, however, indicates an additional incongruent weathering influence on the Sr isotopic signatures of the clays. The incongruent release of particular mineral phases most likely adds some "noise" to the signal originating from mixing of the sources. Moreover, the sea level fluctuations discussed above, and the accompanied floodplain changes, would have significantly affected the extent of chemical weathering of the sediments. Comparison to results of previous studies that interpreted the Sr isotope variability to be related to weathering regime changes, suggests that incongruent weathering contributed up to ~0.003 of the $^{87}Sr/^{86}Sr$ signature of U1443 clays (Blum and Erel, 1995).

Overall, the spectral analyses of the highest resolution data hint to the fluctuations in clay source being forced by strong variations in monsoon strength while the reduction in variability may have resulted from climate and sea level changes influencing the weathering of foreland sediments.

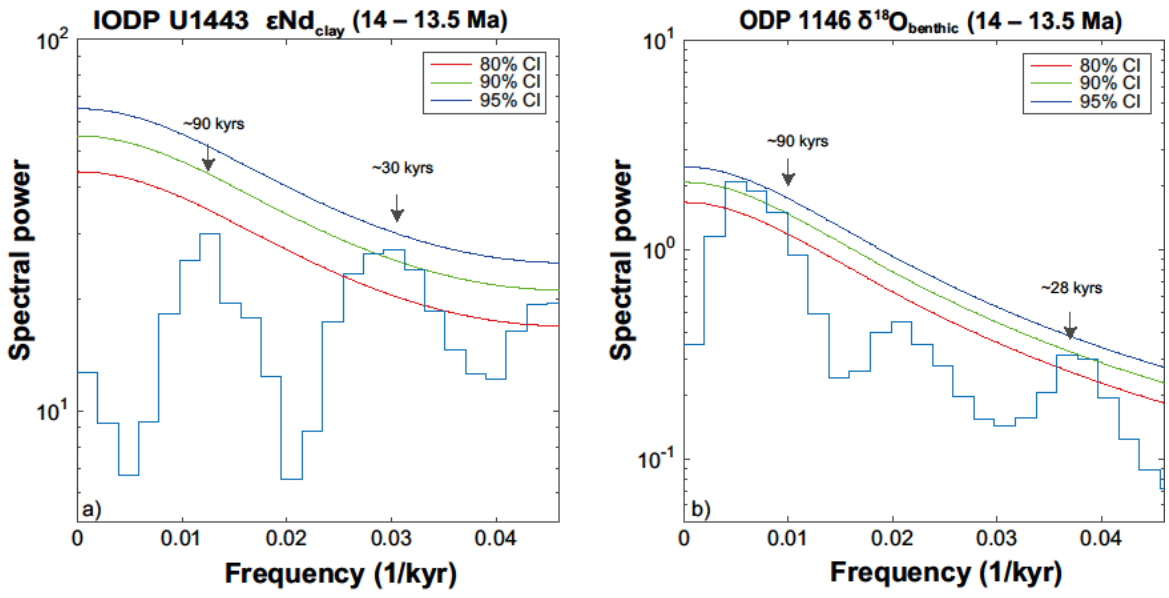

Fig. 3.8: REDFIT spectral analysis of a) Nd isotope compositions of the U1443 clay samples, and b) benthic $\delta^{18}O$ timeseries of ODP Site 1146 (Holbourn et al., 2010) for the interval spanning from 14 to 13.5 Ma. The values of the oversample and segments applied were two and three, respectively.

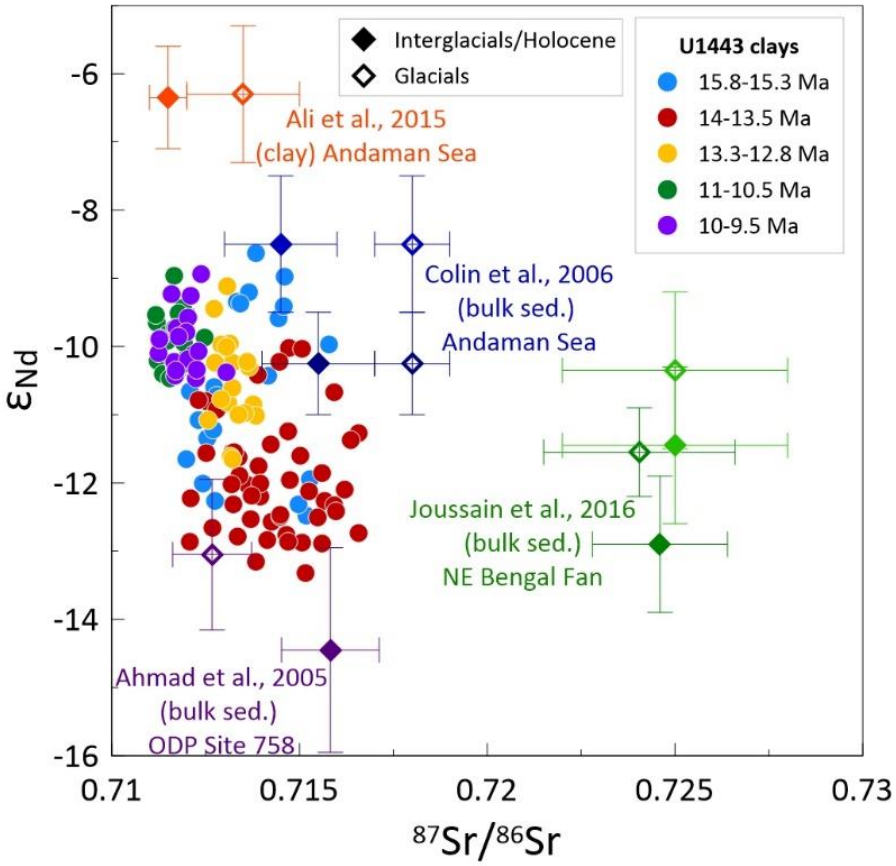

Fig. 3.9: ε_{Nd} vs. 87Sr/86Sr cross-plot of U1443 detrital clay data for all five intervals together with average glacial vs. interglacial values from the literature (Ahmad et al., 2005; Ali et al., 2015; Colin et al., 2006; Joussain et al., 2016). There are two glacial/interglacial average values for the Colin et al. (2006) and Joussain et al. (2016) studies to account for two different sediment core locations.

3.5 Conclusions

We present the first orbital-scale resolution Miocene record of the radiogenic Sr, Nd, and Pb isotope compositions of detrital clays from IODP Site U1443 in the southern Bay of Bengal. Our records focus on key intervals of the middle Miocene and allow us to distinguish tectonic and climatic forcing of monsoon intensity, weathering regime and erosion intensity of the watersheds feeding into the Bay of Bengal. The clay radiogenic isotope signatures indicate that throughout the Miocene intervals, the source of the clays originated from a mixture of the High Himalayan Crystalline, the Tethyan Sedimentary Series and Indo-Burman Ranges. This is remarkable considering the major tectonic orogenic reorganization that took place in the Himalayas during the Miocene. A marked and sudden decrease in average values and variability of the isotope signatures occurred between 13.5 and 13.3 Ma after the middle Miocene global cooling step. While the warmer intervals prior to 13.5 Ma were marked by a much higher variability in the compositions of all three isotope systems and by increased Himalayan contributions, inferred from up to 40 % of the detrital material supplied by the Ganges River, the colder intervals were characterized by lower isotopic variability and increased relative contributions from the Indo-Burman-Ranges. This change in variability

coincided with the tectonic reorganization of thrusting, shifting the main orographic barrier to the south and slowing down exhumation of extended internal regions of the High Himalayas, Tethyan Himalayas and suture zone regions to the north. While tectonic reorganization likely had some background influence, the relatively short period of 200 kyr, in which most of the change happened, argues for global climate cooling being the primary driver for the decrease in radiogenic isotope variability at Site U1443 due to the associated impact on precipitation patterns-causing a restriction of the supply of High Himalayan erosion products.

The fluctuations of the isotope signatures on orbital timescales were mainly triggered by changes in the balance of source contributions and were climatically driven. Since the grain size was confined to the clay fraction, transport related effects are considered minor. The major control on those short-term fluctuations were likely shifts of weathering regimes on land, influenced by changes of the locus of peak monsoon precipitation between higher and lower elevations. This is supported by the presence of a significant 30 kyr periodicity in the Nd isotope record, a heterodyne typically associated with monsoon variability, as well as 100 kyr eccentricity cycles in the record which could reflect changes in sea level affecting the spatial variation of floodplain extent.

3.6 Supplementary Material: Spectral analysis and aliasing

Spectral analyses of high-resolution ε_{Nd} data obtained between 14 and 13.5 Ma and on unevenly spaced time series was performed using REDFIT (Schulz and Mudelsee, 2002). The high-resolution ε_{Nd} data spanning between 14 and 13.5 Ma has an average sampling resolution of ~10 kyrs. The primary objective here is to test whether there is significant periodicity in the proxy timeseries with sufficient resolution while avoiding errors due to spectral aliasing (e.g., Pisias and Mix, 1988). The high-resolution ε_{Nd} data spanning between 14 and 13.5 Ma document a significant ~30 kyr cyclicity, with additional contributions of the ~100 kyr eccentricity cycle (Fig. 3.8). To test whether the observed spectral variance in this section of the record is not caused by spectral aliasing (e.g., Pisias and Mix, 1988), REDFIT spectral analyses were performed on evenly spaced (5 kyrs) proxy timeseries between 14 and 13.5 Ma and unevnely spaced proxy timeseries between 14 and 13.75 Ma (Fig. 3.10). The latter section of the record, in particular, has an average sampling resolution of ~7 kyrs and provides sufficient resolution to resolve Milankovitch band cyclicity in the proxy timeseries. Both evenly and unevenly spaced proxy timeseries document a significant ~30 kyr cyclicity and are consistent with results shown in Fig. 3.8 in the main text. It's therefore conceivable that the ~30 kyr periodicity observed in the high-resolution ε_{Nd} data is likely a heterodyne produced by interaction of the three major orbital cycles rather than one produced by spectral aliasing.

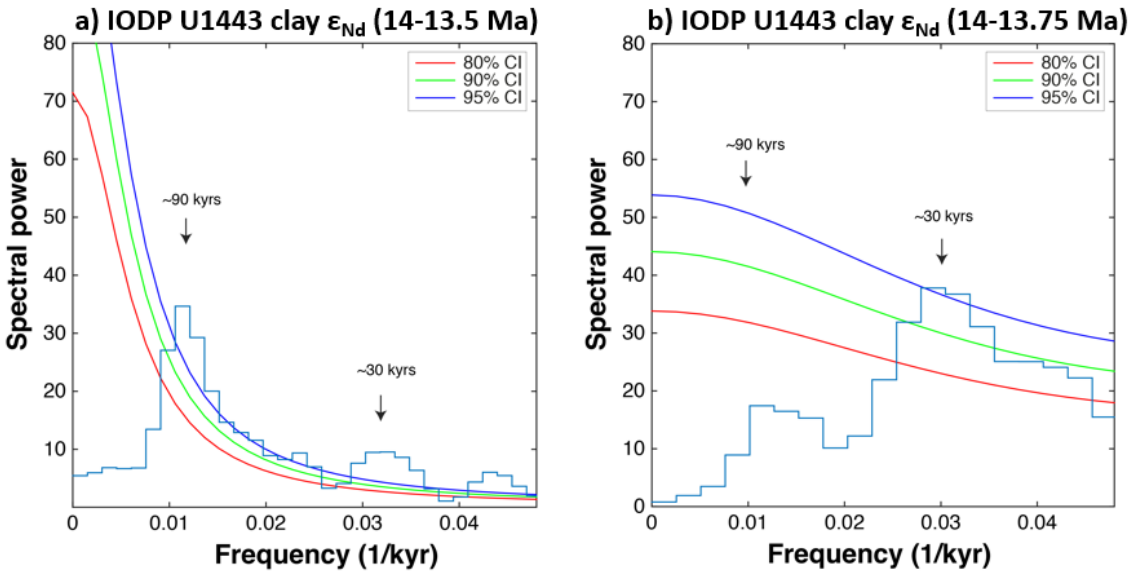

Fig. 3.10: REDFIT spectral analysis of Nd isotope compositions of the U1443 clay samples a) spanning from 14 to 13.5 Ma on an evenly spaced time interval of 5 kyrs, and b) spanning from 14 to 13.75 Ma on an unevenly spaced timeseries. The values of the oversample and segments applied were two and two, respectively.

4. Scientific Chapter II

Enhanced Late Miocene chemical weathering and altered precipitation patterns in the watersheds of the Bay of Bengal recorded by detrital clay radiogenic isotopes

Abstract

The South Asian Monsoon has long been thought to have intensified or even initiated during the late Miocene but this has been challenged in recent years by studies suggesting a weakening of the monsoon at this time. Declining CO_2 levels and extensive environmental changes had a large impact on monsoon strength as well as on the weathering and erosion intensity of the watersheds feeding into the Bay of Bengal, but these feedback systems are known to work in multiple ways. To resolve some of this ambiguity, radiogenic Sr, Nd, and Pb isotope compositions of detrital clays from IODP Site U1443 in the southern Bay of Bengal were analysed to reconstruct changes in sediment provenance and weathering regime related to South Asian Monsoon intensity from 9 to 5 Ma. The 100 kyr resolution late Miocene to early Pliocene record suggests an overall low variability of the provenance of the clays deposited on the Ninetyeast Ridge. However, at 7.3 Ma, Nd and Pb isotope compositions indicate a switch to elevated contributions from the Irrawaddy River (by ~10 %) and a relative decrease of the Himalayan contributions supplied by the Ganges and Brahmaputra Rivers. This was contemporaneous with the global benthic $\delta^{13}C$ decline, which was driven by C4 plant expansion on land. Global cooling and increasing aridity likely resulted in an eastward shift of precipitation patterns leading to a more focussed erosion of the Indo-Burman Ranges. Sr isotope compositions were decoupled from Nd and Pb isotope signatures and became more radiogenic between 6 and 5 Ma. Grassland expansion generating thick, easily weatherable soils and potentially enlarged floodplains as a consequence of a sea level drop led to an environment supporting intense chemical weathering likely responsible for the elevated detrital clay $^{87}Sr/^{86}Sr$ ratios. This change in detrital Sr isotope signatures may also have contributed to the major late Miocene increase in seawater Sr isotope composition.

4.1 Introduction

The Late Miocene was an important period within the global Cenozoic cooling trend and was marked by extensive marine and terrestrial environmental and ecosystem changes. This time interval was characterized by relative global warmth and thus holds great potential to better understand climate-carbon cycle dynamics on a warmer-than-modern Earth (Holbourn et al., 2018). It is, however, not yet well understood how exactly tectonic changes within the Himalayas, global climate change and associated ecosystem transformation, and the erosion and weathering regimes

were linked and what effect they had on South Asian Monsoon (SAM) strength and vice versa during the late Miocene.

As global climate cooled during the Miocene, the first ephemeral northern hemisphere glaciations occurred between 6 and 5.5 Ma (Holbourn et al., 2018). Interestingly, benthic oxygen isotopes ($\delta^{18}O$) did not change much during the late Miocene indicating minor ice-sheet variability, while a global decrease in benthic $\delta^{13}C$ was observed (Herbert et al., 2016). This has been related to the aridification of interior Asia (An et al., 2001) and the expansion of C4 plants in the Himalayan foreland basin (Clift and Webb, 2018; Galy et al., 2010; Huang et al., 2007; Quade et al., 1989; Singh et al., 2011). These changes have been linked to the strengthening of the dry winter monsoon season in the east Asian domain (Holbourn et al., 2018).

Studies of the tectonic evolution of the Himalayas in the late Miocene are contradictory. While several publications inferred a pulse of Himalayan-Tibetan plateau uplift around 8 Ma (An et al., 2001; Li et al., 2014; Miao et al., 2012; Molnar, 2005), other studies claimed that the plateau has been at nearly present elevation for the past 15 Myr (e.g., Ding et al., 2017). Accumulation rates of the distal Bengal Fan, as recorded in ODP Sites 717 and 718, were high from 17 to 7 Ma, but decreased from 7 to 1 Ma (Derry and France-Lanord, 1996). Moreover, the clay mineral assemblages of these sites indicated high chemical weathering intensity and reduced physical erosion rates in the Ganges-Brahmaputra basin after 7 Ma (Derry and France-Lanord, 1996). Another argument brought forward against a major enhancement of tectonic uplift in the late Miocene is the relatively constant provenance of the eroded sediments supplied to the Bengal Fan over the last >17 Ma (Derry and France-Lanord, 1996; Galy et al., 2010) and to the Ninetyeast Ridge (NER) over the last 27 Ma (Ali et al., 2021).

Changes in weathering regime have also been related to monsoon strength. For many years, it was considered that the SAM experienced a major strengthening at ~8-7 Ma as suggested by enhanced oceanic upwelling recorded in the Arabian Sea (Gupta et al., 2015; Kroon et al., 1991). However, studies investigating the late Miocene monsoon intensity using different proxies in different regions rather indicate a weakening of summer monsoon intensity, as inferred for example from clay mineral compositions (Lee et al., 2019), K/Al ratios (Clift et al., 2008), seawater $\delta^{18}O$ (Steinke et al., 2008) or leaf wax δD (Huang et al., 2007). At the same time, winter monsoon intensity is thought to have strengthened (Holbourn et al., 2018; Huang et al., 2007; Lee et al., 2019). The discrepancy between these interpretations results from the mismatch between oceanic wind-based records and rain-related erosion and weathering records. To reconcile the discrepancies between the proxy records, Clift et al. (2014) suggested that chemical weathering is largely controlled by temperature rather than seasonal summer rainfall, while physical erosion rates are much more affected by precipitation than by changes in temperature.

All studies investigating the relationship between variations of the SAM and the erosional and weathering regime during the Miocene period have been carried out at low time resolution (e.g., France-Lanord et al., 1993: Myr timescale) and thus do not allow insights into the links between orbital scale climate variability and monsoon strength. The continuous sediment record recovered at IODP Site U1443 on the NER in the southern Bay of Bengal now allows a much more detailed study. A high resolution benthic stable isotope record from 9 to 5 Ma is available (Bolton et al., unpublished), which provides the climatic and stratigraphic framework to reconstruct the evolution of Himalayan silicate weathering and its relationship to changes of the SAM and climate during the late Miocene based on radiogenic isotope compositions of the clay size fraction at Site U1443. Since tectonics, climate, erosion, as well as the type and intensity of weathering and monsoon strength can all affect the detrital isotope signatures on different time scales, our approach is to disentangle these different factors using multiple isotope systems and higher temporal resolution records than in previous studies to advance our understanding of the major controls of past SAM intensity.

The Bay of Bengal receives large freshwater and sediment inputs from the rivers draining the Himalayas (Ganges, Brahmaputra, Meghna), the Indo-Burman Ranges (Irrawaddy) and the Arakan coast, and the Indian Peninsula (Godavari, Krishna, Mahanadi) (Fig. 4.1). The sediments deposited in the Bay of Bengal mainly originate from Himalayan erosion and have formed the world's largest submarine fan, the Bengal Fan (Curray et al., 2003) as well as the Nicobar Fan (McNeill et al., 2017; Pickering et al., 2020). The Bengal Fan has existed since at least early Miocene times and its deposits provide a record of the erosion and weathering history of the surrounding mountain belts (Derry and France-Lanord, 1996; France-Lanord et al., 1993). Since the majority of sediments is transported to the Bay of Bengal during peak monsoon precipitation (Singh et al., 2007), the variability of erosion intensity and deposition rates has been directly related to changes in monsoonal precipitation. The erosion intensity of the Himalayas is considered a fundamental driver of Earth's climate because the sequestration of CO_2 through enhanced silicate weathering and the burial of organic carbon in the fan reduced global temperatures (France-Lanord and Derry, 1997; Galy et al., 2007; Galy et al., 2010; Raymo, 1994; Raymo and Ruddiman, 1992).

Elevated secondary clay abundances, in particular of smectite and its more radiogenic Sr isotope ratio in the late Miocene reflect an interval of intensified chemical weathering intensity (Ali et al., 2021; Derry and France-Lanord, 1996).

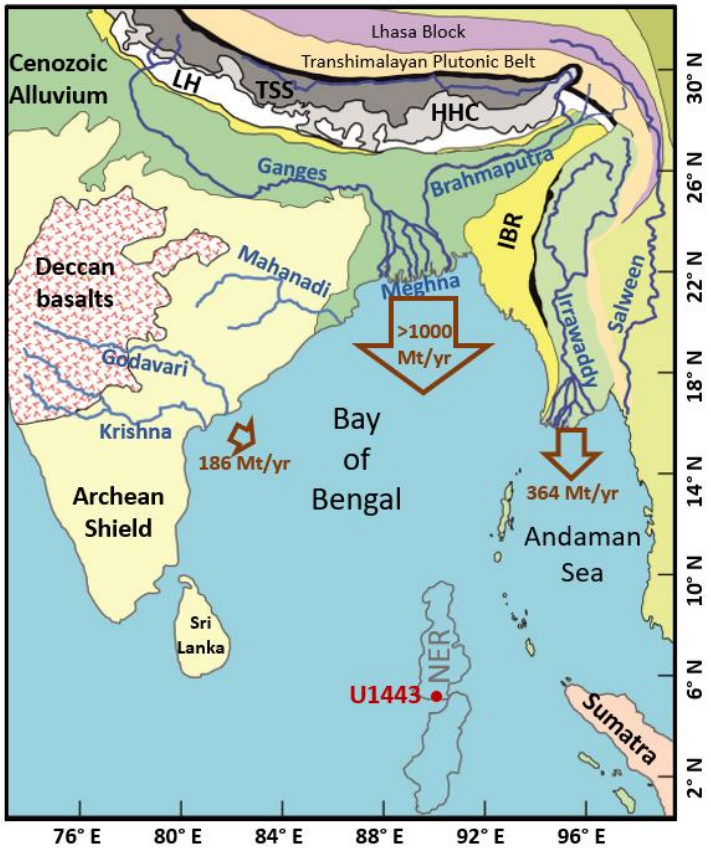

Fig. 4.1: Map of the Bay of Bengal modified from Ali et al. (2021). The location of IODP Site U1443 on the Ninetyeast Ridge (NER) is marked. The major continental river systems and the major geological units are also indicated: LH = Lesser Himalayas, TSS = Tethyan Sedimentary Series, HHC = High Himalayan Crystalline, and IBR = Indo Burman Ranges. The arrows indicate modern sediment fluxes of the major rivers (Milliman and Syvitski, 1992; Robinson et al., 2007).

Radiogenic Sr, Nd, and Pb isotope compositions of detrital material vary as a function of the age and the geological history of the continental rocks in the hinterland and therefore serve as reliable tracers of sediment provenance and sources transported to the central Bay of Bengal (Ahmad et al., 2005; Colin et al., 1999). The continental lithologies surrounding the Bay of Bengal constrain the possible endmembers for the mixture of sediments deposited at Site U1443. Within the Himalayas, at least four main lithologies are likely sources: The High Himalayan Crystalline (HHC), the Tethyan Sedimentary Series (TSS), the Transhimalayan Plutonic Belt (TPB), and the Lesser Himalaya (LH) (France-Lanord and Le Fort, 1988; Galy et al., 1996; Singh and France-Lanord, 2002). Another important source are the Indo-Burman Ranges (IBR), which have an isotopic signature almost identical to the TPB (Awasthi et al., 2014; Singh and France-Lanord, 2002) and have been the western boundary of the Irrawaddy catchment since the earliest Miocene (Najman et al., 2020). The Brahmaputra River, in which the TPB draining Yarlung-Tsangpo River is entrained, includes that TPB contribution (Singh and France-Lanord, 2002), which is why the sediments displaying radiogenic isotope signatures in that range are attributed to the IBR. Based on the mixture

of these distinct sediment source signatures in the Bay of Bengal, the location of highest monsoon precipitation as well as erosional and tectonic changes can be inferred.

Here, we reconstruct monsoon variability at a 100 kyr resolution based on the continuous sediment record of the crest of the NER, an advantage compared to the discontinuous turbiditic Bengal Fan sediments. We focus on the detrital clay size to minimize mineral sorting effects that occur during transport. This is particularly important for Sr and Pb isotopic ratios, which vary systematically with grain size (Douglas et al., 1995; Eisenhauer et al., 1999; Garçon et al., 2014; Tütken et al., 2002). Even though Nd isotope signatures generally do not vary strongly with grain size (e.g., Tütken et al., 2002), exceptions exist, in particular in sediments from "larger rivers" (Bayon et al., 2015). Sr and Pb isotope compositions are additionally influenced by fractionation during weathering and transport due to large variations in the isotope composition of different mineral phases and differences in their resistance to weathering (Ali et al., 2015; Blum et al., 1993; Tütken et al., 2002). These isotopic signals thus also provide information on prevailing weathering regimes in the past. Concentrating on the clay size fraction allows to infer both changes in source contributions and climatically driven weathering effects.

4.2 Methods

Our study is based on sediments of IODP Site U1443 (Latitude 5°23'N; Longitude 90°21'E, water depth ~2930 mbsl), cored with the RV *JOIDES Resolution* during IODP Expedition 353 in December 2014. Site U1443 was a redrill of nearby ODP Site 758 and located on the crest of the NER in the southern Bay of Bengal. This ridge-top location ensured a slow and continuous sedimentation and prevented the deposition of disturbed sedimentary sequences typically associated with transport processes of the Bengal Fan (Clemens et al., 2016). The sedimentation rate during the Late Miocene was ~1.20 cm/kyr (Clemens et al., 2016). Four holes were combined to form a splice comprising sediments from the Oligocene to the late Pleistocene. The recovered sediment is a nannofossil ooze with varying abundances of detrital clays, foraminifers, and authigenic carbonates (Clemens et al., 2016). The Late Miocene samples span a composite core depth from 70 m to 123 m below seafloor. The age model used in this study is based on astronomically tuned $\delta^{18}O$ and $\delta^{13}C$ measurements of epifaunal benthic foraminifers by Bolton et al. (unpublished).

In the laboratories of CEREGE, the sediment samples were washed over a 63 µm sieve and the fine fraction collected. While the coarser fraction was used for micropaleontological work, the fine fraction was sent to GEOMAR where it was freeze-dried and processed to isolate clays. Firstly, the fine fraction was leached to remove all authigenic Fe-Mn oxyhydroxides following a procedure modified from Gutjahr et al. (2007) and the first leach was kept for future analysis of the dissolved radiogenic isotope signature of past seawater. Briefly, ~2 g of fine sediment were washed with

deionized water, leached step by step with a 0.05M hydroxylamine hydrochloride–15% distilled acetic acid–0.03M Na-EDTA solution, buffered to pH 4 with analytical grade NaOH. To remove all the oxides, the samples were leached in a strong leach solution overnight before being fully decarbonated with 40 % acetic acid (acid was added until no reaction was visible and then some excess). Having been washed again with deionized water, the clay fraction was separated using a centrifuge-based Atterberg method.

For the radiogenic isotope analyses, the clay fraction was then dried at low temperature (<45°C) in an oven. About 100 mg of the dried clays were completely digested using alkaline fusion (NaOH-Na_2O_2), as described in Bayon et al. (2009a) but without addition of TiO_2, Fe_2O_3 or Tm, and then further dissolved in 6 M HCl. To separate and purify Nd, Sr and Pb, standard ion chromatographic procedures were applied (Cohen et al., 1988; Galer and O'Nions, 1989; Pin and Zalduegui, 1997). For Nd, first the REEs (including Nd) were separated using a cation exchange resin (Bio-Rad AG 50W-X8, 200-400 mesh), while most matrix elements were discarded. The Nd was then separated from the other REEs using Ln-spec resin (50-100 µm). Pb and Sr were separated using AG1-X8 (100-200 µm) and Sr-Spec resin, respectively. Sr isotope measurements were performed on a Nu Plasma high-resolution MC-ICP-MS while Nd and Pb isotope analyses were carried out on a Thermo Scientific Neptune Plus MC-ICP-MS at GEOMAR.

Nd isotope ratios were corrected for instrumental mass bias using a $^{146}Nd/^{144}Nd$ of 0.7219 (Vance and Thirlwall, 2002) and were normalized to the accepted values of the JNdi-1 standard (0.512115; Tanaka et al., 2000). The Nd isotope ratios are reported as $\varepsilon_{Nd}(0)$ values = $(((^{143}Nd/^{144}Nd)_{sample}/(^{143}Nd/^{144}Nd)_{CHUR} - 1) \times 10^4$ with CHUR being the Chondritic Uniform Reservoir and $(^{143}Nd/^{144}Nd)_{CHUR} = 0.512638$ (Jacobsen and Wasserburg, 1980). Procedural blanks for Nd were ≤50 pg and thus below 0.05 % of the total amount of Nd in the samples. Separate digestions and measurements of USGS reference material BHVO-2 (n=8) gave a mean ε_{Nd} value of 6.75±0.24, which agrees well with the mean value (6.65±0.60) reported by the GeoReM database (Jochum et al., 2016).

The instrumental mass bias of Sr isotopic measurements was corrected using a $^{88}Sr/^{86}Sr$ of 0.1194 (Steiger and Jäger, 1977) and normalized to the NIST SRM 987 $^{87}Sr/^{86}Sr$ of 0.710245. Procedural blanks were an average 50 ng, contributing between 0.6 and 3 % of the total Sr signal. This rather high contribution originated from the use of NaOH and NaO_2 for the alkaline fusion. To correct for the blank contributions, samples of the reagents were regularly digested and measured for concentrations (n=15). These were later combined and measured for their isotopic composition. The blank contributions were then removed from the Sr sample signals via mass balance calculations. Repeated digestions and measurements of USGS reference material BHVO-2 (n=12) gave a mean $^{87}Sr/^{86}Sr$ value of 0.70363±0.00013, which is in good agreement with the GeoReM average value of 0.70348±0.00006.

The mass bias correction for the Pb isotope measurements was carried out by doping the samples with the NIST997 Tl standard solution (Pb/Tl ~4) (Belshaw et al., 1998; White et al., 2000). Since Tl and Pb fractionate slightly differently during ionization (Vance and Thirlwall, 2002), $^{205}Tl/^{203}Tl$ was adjusted on a session-by-session basis in order to match accepted SRM 981 Pb isotope compositions ($^{206}Pb/^{204}Pb$ = 16.9416, $^{207}Pb/^{204}Pb$ = 15.4998 and $^{208}Pb/^{204}Pb$ = 36.7249; Baker et al., 2004). Repeated processing and analysis of USGS reference material BHVO-2 (n=6) gave mean values (±2 standard deviations) of 18.619±0.090, 15.536±0.019, and 38.219±0.052 for $^{206}Pb/^{204}Pb$, $^{207}Pb/^{204}Pb$, and $^{208}Pb/^{204}Pb$, respectively. These Pb isotope values agree well with those previously measured for BHVO-2 (n=44, 18.637±0.073, 15.528±0.045, and 38.223±0.103; GeoReM database). Procedural blanks for Pb were ≤60 pg and contributed less than 0.1% of the total amount of Pb in the samples.

4.3 Results and Discussion

The $^{87}Sr/^{86}Sr$, ε_{Nd}, and Pb isotope compositions ($^{206}Pb/^{204}Pb$, $^{207}Pb/^{204}Pb$, $^{208}Pb/^{204}Pb$, $^{207}Pb/^{206}Pb$ and $^{208}Pb/^{206}Pb$) of the silicate clay fraction are shown in Fig. 4.2 and are provided in Tables A5 and A6. The $^{87}Sr/^{86}Sr$ compositions vary between 0.71261 and 0.71595 over the entire time interval from 9 to 5 Ma. Between 9 and 6 Ma, the $^{87}Sr/^{86}Sr$ values exhibit little variability between 0.71261 and 0.71465 but then increase to a maximum value of 0.71595 between 6 and 5 Ma. The ε_{Nd} values range from -11.4 to -9.1, with a small step change in average ε_{Nd} value from ~-10.7 between 9 and 7.3 Ma to a more radiogenic average ε_{Nd} value of ~-10.1 between 7.3 and 5 Ma. $^{206}Pb/^{204}Pb$ values vary between 18.945 and 19.084 and, similar to the ε_{Nd} values, exhibit a step change in average values at ~7.3 Ma: The average $^{206}Pb/^{204}Pb$ signature between 9 and 7.3 Ma of ~19.02 decreased to ~18.99 between 7.3 and 5 Ma.

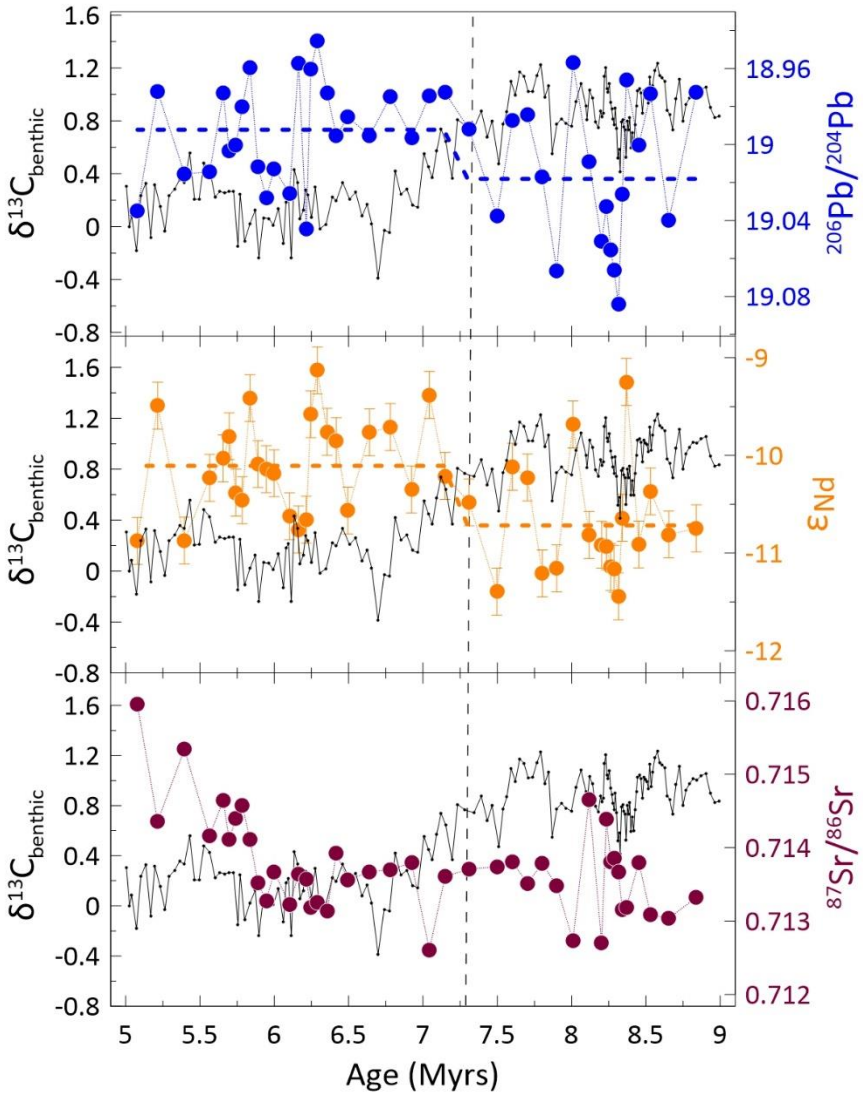

Fig. 4.2: Radiogenic Pb (blue, inverted scale), Nd (orange) and Sr (red) isotope compositions of U1443 clays compared to the benthic $\delta^{13}C$ signal for the interval from 9 to 5 Ma. The black dots and line represent every 6th value of the benthic $\delta^{13}C$ measurements of Bolton et al. (unpublished) and Lübbers et al. (2019). The error bars represent the 2 s.d. of the repeated processing and measurement of BHVO-2 and are smaller than symbol size for Sr and Pb isotopes. The horizontal dashed lines represent the average Pb and Nd isotope compositions before and after 7.3 Ma (vertical dashed line) representing the shift to more Irrawaddy dominated contributions. A t-test using the software Past verified that the average values in ε_{Nd} and $^{206}Pb/^{204}Pb$ signatures before and after 7.3 Ma differed significantly from one another ($p\text{-values}_{same\ mean} < 0.05$).

4.3.1 Provenance of clays

The U1443 clays represent a mixture of the Indo-Burman Ranges (IBR), High Himalayan Crystalline (HHC), and Tethyan Sedimentary Series (TSS) sources. Fig. 4.3 shows the Nd-Sr isotope compositions of the U1443 clays in comparison with literature data of possible source areas and the isotopic compositions of sediments of the major rivers. The TPB is not separately defined here as an independent source area because it is included in the Brahmaputra sediment signatures. The TPB and TSS rocks are widely exposed in the drainage basin of the Yarlung-Tsangpo River, which flows into the Brahmaputra and is the main reason for the difference in isotope signatures

between Ganges and Brahmaputra sediments. In addition to the sediments supplied to the NER by the big rivers, fine-grained mineral dust, for example from the Thar desert, may have contributed to the U1443 clay isotopic composition. However, the annual mineral dust input only makes up ~1 % of the amount of sediment supplied by the Ganges, Brahmaputra and Irrawaddy Rivers to the Bay of Bengal (Fig. 4.1; Milliman and Syvitski, 1992; Robinson et al., 2007; Srinivas and Sarin, 2013) and is therefore considered negligible. Moreover, sources from the Indian Peninsula or the Sumatra volcanic are considered to be minor, as discussed in Bretschneider et al. (submitted).

The binary mixing relationships of Nd-Sr (Fig. 4.3), Pb-Pb (Fig. 4.4), and Nd-Pb (Fig. 4.5) isotope compositions between the most likely endmembers (Table 4.1) allow to identify and quantify the different sediment contributions of the different major rivers to the NER clays. To better constrain the different source contributions, ternary mixing grids were added to Figures 4.3, 4.4, and 4.5. Since data for all three isotope systems exist for most of the river sediments, we applied average Irrawaddy clay, and average bulk Brahmaputra and Ganges sediment isotopic signatures as mixing endmembers. Even though the comparison of different grain sizes is not ideal, grain size effects are small compared to the isotopic range of source areas, making it reasonable to relate the clay results to bulk sediment data (c.f. Bretschneider et al., submitted). On the Nd-Sr isotope mixing plot, the U1443 clays do not fall within the triangle spanned by the Irrawaddy, Brahmaputra and Ganges sediments (Fig. 4.3). While ε_{Nd} values plot close to a mixing line between the Irrawaddy and Brahmaputra endmembers, the $^{87}Sr/^{86}Sr$ isotopic signatures are shifted towards less radiogenic Sr values and do not overlap with any mixing trends between the three endmembers (Fig. 4.3). A similar offset has already been discussed by Bretschneider et al. (submitted) for the period between 15.8 and 9.5 Ma and has been attributed to a shift in the average source endmember signature of the clays towards less radiogenic Sr isotopic signatures in the Miocene compared to the modern. We note that the spread in Sr isotope compositions of measured river sediments, especially for the Brahmaputra River, is large and the available data may simply miss the least radiogenic part. Therefore, the mixing relationship of the Pb-Pb and the Nd-Pb isotope systems are likely more appropriate to reflect changes in the source provenance of the clays. The plots (Figs. 4.4 and 4.5) clearly demonstrate that all three endmembers contributed to the late Miocene U1443 Pb and Nd budgets. The late Miocene samples define a clear linear trend on the Pb-Pb isotope plot (Fig. 4.4) on the mixing line between Irrawaddy clay and a mixture of ~45 % Ganges and ~55 % Brahmaputra sources. The Irrawaddy contribution ranges from ~25 % to 60 %, while the mixed Himalayan contribution accordingly amounts 40-75 %. On the Nd-Pb isotope plot (Fig. 4.5), the binary trend is not as obvious. The Irrawaddy contribution ranges from ~20 % to 55 %, very close to what has been inferred from the Pb-Pb mixing plot. If a binary mixing line is drawn through the samples and the Irrawaddy endmember, the Ganges-Brahmaputra (G-B) endmember mixture would again be very similar to the Pb-Pb plot reaching around 40 % Ganges and 60 % Brahmaputra contributions.

The late Miocene samples are offset from the middle Miocene U1443 clays (Bretschneider et al., submitted). This offset is most likely due to a shift to a higher Ganges fraction in the G-B endmember. A 20 % elevated fraction of Ganges material in the G-B mixture in the late Miocene compared to middle Miocene intervals (15.8 to 9.5 Ma) can explain this shift. Another possibility for the offset could be some minor LH contributions. If we substitute the Ganges for LH material, a contribution of 3 to 10 % LH material could account for the shift in the late Miocene sample composition. Since this is unrealistic given that there must have been a Ganges contribution, it is likely that much smaller percentages of the LH component shifted the Ganges endmember towards more radiogenic Sr and less radiogenic Nd isotope compositions. Thus, it was not necessarily a higher contribution but a shift in Ganges endmember composition that may have resulted in the shift of the clays' isotope composition.

Table 4.1: Sr, Nd, and Pb average isotopic compositions and concentrations for the major lithologies and river systems used as endmembers from the literature.

Endmember	$^{87}Sr/^{86}Sr$	Sr (ppm)	ε_{Nd}	Nd (ppm)	$^{206}Pb/^{204}Pb$	$^{208}Pb/^{204}Pb$	References
IBR	0.71	200	-5.2	24			Awasthi et al. (2014)
TSS	0.727	229	-13	26.7			France-Lanord et al. (1993)
HHC	0.755	70	-15.5	23.6			France-Lanord et al. (1993); Singh and France-Lanord (2002)
LH	0.85	70	-24.4	40.3	21		Singh and France-Lanord (2002); Clift et al. (2002)
TPB	0.705	400	-6.5				Singh and France-Lanord (2002)
Irrawaddy	0.716	100	-6.47	50	18.751	39.098	Awasthi et al. (2014); this study
Brahmaputra	0.719	212	-12.5	35.6	18.938	39.571	Singh and France-Lanord (2002); Millot et al. (2004)
Ganges	0.772	32	-17.2	23.6	19.508	39.766	Singh and France-Lanord (2002); Millot et al. (2004)

The late Miocene time series of Fig. 4.2 shows a step change in both average ε_{Nd} and $^{206}Pb/^{204}Pb$ values at ~7.3 Ma. The Nd isotope composition becomes more radiogenic, while the average Pb isotope composition decreases, both indicating an increase in Irrawaddy sediment contributions of about ~10 % on average. Although the change in the average value is small (but statistically significant), more radiogenic ε_{Nd} and lower $^{206}Pb/^{204}Pb$ values occurred much more frequently after 7.3 Ma and the peak unradiogenic ε_{Nd} and highest $^{206}Pb/^{204}Pb$ values were less extreme than those encountered prior to 7.3 Ma. This may hint to the reduction of the least radiogenic ε_{Nd} component, either the HHC or a small LH fraction, or that Irrawaddy material was more continuously supplied than prior to 7.3 Ma.

Overall, the sources contributing material to the U1443 clays remained relatively stable throughout the late Miocene, which is in agreement with the relatively stable provenance of sediments supplied

to the Bengal Fan over the last 12 Ma (Galy et al., 2010) and of the clays delivered to the NER over the last 27 Ma (Ali et al., 2021).

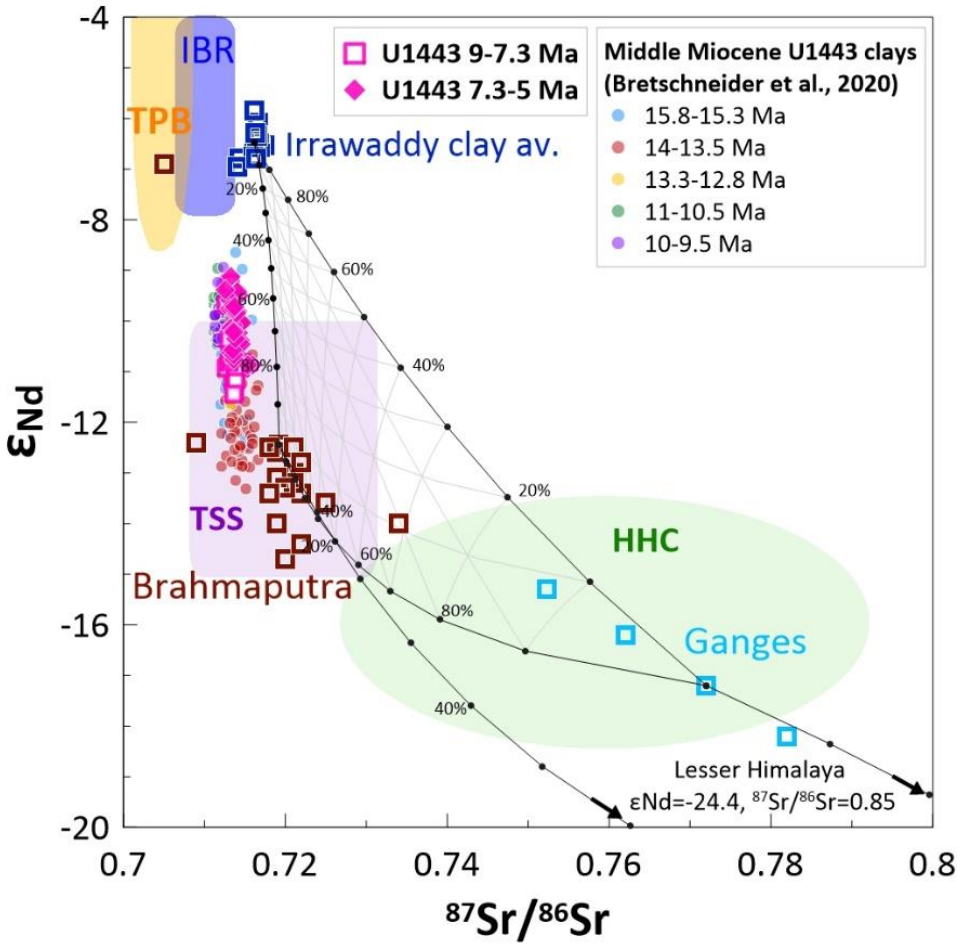

Fig. 4.3: Nd-Sr isotope composition of the clay size fraction of Site U1443 compared with literature data of possible sources. These include the different Himalayan lithologies (Transhimalayan Plutonic Belt - TPB, Tethyan Sedimentary Series - TSS, High Himalayan Crystalline – HCC, and Lesser Himalaya) and the Indo-Burman Ranges (IBR) and the rivers draining these lithologies – Irrawaddy, Ganges, and Brahmaputra (squares). References are listed in Table 4.1. Average values of the three major rivers are used as endmembers for the displayed mixing plane. The grid was calculated at 10% increments of the composition of the mixture using the endmembers listed in Table 4.1. U1443 clays do not plot within the mixing triangle but show an offset binary mixing trend between the Irrawaddy (IBR) and the Brahmaputra.

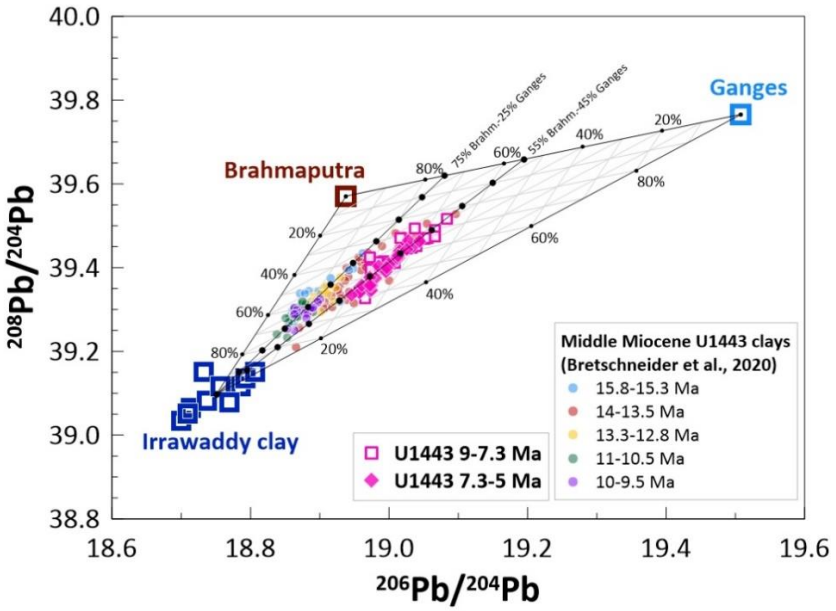

Fig. 4.4: Pb isotope composition of U1443 clays and potential sources represented by the Irrawaddy, Ganges, and Brahmaputra (squares, for references see Table 4.1). The compositions of the three major rivers are used as endmembers to draw the mixing plane. The grid was calculated at 10% increments of the composition of the mixture using the endmembers listed in Table 4.1. U1443 clays plot within the mixing triangle, supporting a mixture of the contributions of the three applied source endmembers. Two binary mixing lines between the Irrawaddy endmember and two different Brahmaputra-Ganges mixtures are shown. The late Miocene data plot on a binary mixing line with higher Ganges contribution (45%) while most other Miocene samples plot on the binary mixing line with only 25% Ganges contribution.

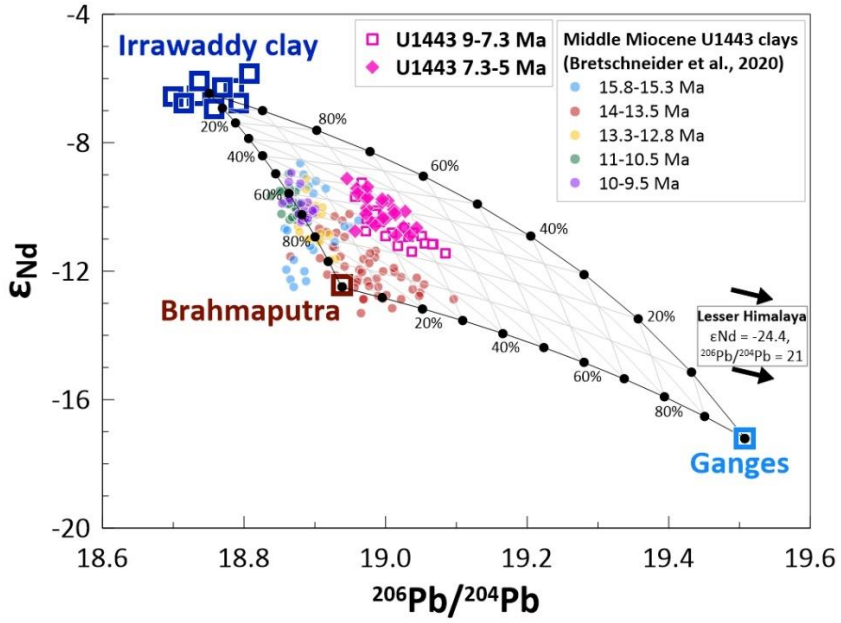

Fig. 4.5: Nd-Pb isotopic composition of U1443 clays compared to the potential sediment sources, represented by the Irrawaddy, Ganges, and Brahmaputra (squares, for references see Table 4.1). The three major rivers are used as endmembers to draw a mixing plane. The grid was calculated at 10% increments of the composition of the mixture using the endmembers listed in Table 4.1. The late Miocene data of this study are clearly offset from the middle Miocene samples from this site (Bretschneider et al., submitted) indicating a higher Ganges contribution for the younger interval (50-60 %) in the Ganges-Brahmaputra mixed endmember. Lesser Himalayan sediments plot far outside these bounds (as indicated by the black arrows) but contribute to the Ganges signal.

4.3.2 Late Miocene climate change, Himalayan uplift and erosion

The U1443 detrital clay radiogenic isotope record of the late Miocene documents two major changes of sediment sources. Firstly, late Miocene samples are systematically offset to the earlier Miocene intervals in Nd-Pb isotope space, attributed to a shift in the Ganges endmember due to increased LH contributions. Secondly, a shift in source contributions to a more dominant Irrawaddy influence occurred at ~7.3 Ma.

4.3.2.1 Late Miocene exhumation of Lesser Himalayan Units

The difference in the G-B mixture, with the late Miocene samples (9 to 5 Ma) containing higher Ganges contributions (by about 20 %) compared to the earlier intervals, may reflect tectonic changes. One possible reason for the shift in G-B mixture is a more intense erosion of HHC rocks. The exhumation of LH rocks (LH: ε_{Nd} ~-24.4, $^{87}Sr/^{86}Sr$ ~0.85, $^{206}Pb/^{204}Pb$ >19.5; Clift et al., 2002; Singh and France-Lanord, 2002) starting in the middle Miocene at ~16 Ma (Colleps et al., 2018) and continuing into the late Miocene may be another explanation. Surprisingly, in the middle Miocene U1443 record, such signatures were completely absent. This has been attributed to the negligible exposure of LH units in the eastern part of the Himalayas, which acts as the major watershed of the Brahmaputra. The Brahmaputra in turn dominates over Ganges contributions in the Himalayan component in the NER clays. However, it is likely that by ~9 Ma, LH rocks were more exposed due to continuing erosion and thus started contributing to the Ganges system, thereby shifting the G-B mixture towards more radiogenic Pb and Sr and less radiogenic Nd isotope compositions and thus closer to a "Ganges-like" signature. A provenance study from the Siwalik Group recorded the first exhumation of LH units at 9 Ma (Najman et al., 2009) thus matching the timing of our observed shift in isotope compositions. Nevertheless, the LH contribution to the clays reaching the NER remained modest throughout the late Miocene.

4.3.2.2 Step change in Nd and Pb isotope compositions at ~7.3 Ma

The shift in Nd and Pb isotope compositions towards higher Irrawaddy contributions at ~7.3 Ma occurred shortly after the proposed increased uplift of the Himalayas at or just before ~8 Ma (An et al., 2001; Harrison et al., 1992; Li et al., 2014; Molnar, 2005; Molnar et al., 1993; Wang et al., 2014) and coincided with the global $\delta^{13}C$ decline. Interestingly, Galy et al. (2010) observed a trend opposite to our record in their Nd isotope compositions of the last 12 Ma on the Bengal Fan (Fig. 4.6) although their low sampling resolution may have resulted in aliased data (only three samples after 7 Ma). The ε_{Nd} signatures, which are much more Himalayan dominated likely due to different source areas for the coarse material supplied to the Bengal Fan compared to the NER clays, became less radiogenic after 7.4 Ma, which was attributed to an increase of HHC rock contributions (Galy et al., 2010). These authors suggested that a reduction in precipitation may have led to a

concentration of erosion at higher elevations of the Himalayas and consequently enhanced erosion of the HHC. However, the colder climate would also have resulted in less moisture in the atmosphere, hampering rainfall from reaching the high elevations and promoting C4 plant expansion as a result of increased aridity. Moreover, modern-day orographic rainfall patterns are centred above the IBR and the LH and not above the HHC (Ali et al., 2021). Instead of a higher erosion intensity of the HHC, the subtle change observed by Galy et al. (2010) could also be attributed to the onset of erosion of LH units and a modest LH contribution resulting in a decrease of the ε_{Nd} of the mixture. These authors found this unlikely based on the lack of change in Os isotope data from the distal Bengal Fan, because increased LH contributions should have resulted in an increase of the $^{187}Os/^{188}Os$ signature (Galy et al., 2010). However, Os is highly concentrated in organic rich sedimentary rocks (Colleps et al., 2018) and therefore could be decoupled from changes in Sr and Nd provenance, in particular when the required LH contribution was small. This possibility is supported by some of the altered carbonates of the LH not having high Os concentrations or $^{187}Os/^{188}Os$ (Colleps et al., 2018).

The coincidence of increasing Irrawaddy contributions at ~7.3 Ma with the cooling of the global climate and the increasing aridity in the Asian interior suggests that it is reasonable to assume a climatic control on this change in sediment source. The decrease in benthic and planktic $\delta^{13}C$ between ~8 and 6.5 Ma (Diester-Haass et al., 2006; Holbourn et al., 2018) accompanied the $\delta^{13}C$ increase of terrestrial records, such as fossil tooth enamel, soil carbonate or organic matter, which was driven by the C4 plant expansion (Behrensmeyer et al., 2007; Cerling et al., 1997; Herbert et al., 2016; Huang et al., 2007; Quade et al., 1989). C4 plants are enriched in ^{13}C compared to C3 plants and their expansion is thus thought to have transferred significant amounts of material enriched in ^{13}C from the marine to the terrestrial carbon reservoir (Diester-Haass et al., 2006; Holbourn et al., 2018). The emerging grasslands themselves, while possibly promoted by declining levels of atmospheric CO_2 (e.g., Holbourn et al., 2018), may also have favoured regional aridification as a consequence of the higher albedo and lower transpiration compared to woodlands (Retallack, 2001). Moreover, grasslands and their soils serve as an important carbon and water vapor sink and therefore their expansion likely contributed to the long-term global climatic cooling (Retallack, 2001). Precipitation patterns likely also changed with the cooling and drying, thereby shifting the focus of monsoonal rains to the IBR, a region that also receives the most intense monsoon rainfall today (Damodararao et al., 2016). Hence, increased amounts of IBR material with less radiogenic Sr and Pb and more radiogenic Nd signatures were weathered and eroded, as reflected by our record. The Nicobar Fan, which receives sediment delivered from the IBR, had high sediment accumulation rates starting at ~9.5 Ma and persisting until ~5 Ma, when the eastern drainage route closed (Pickering et al., 2020). The high sediment supply was attributed to the inversion of the Shillong Plateau and the westward migration of the Indo-Burman wedge, which

reduced continental accommodation space and thus diverted the sediments south directly to the Nicobar fan (McNeill et al., 2017; Pickering et al., 2020). The timing of change in sediment accumulation rates does not match the timing of the step change in Nd and Pb isotope compositions towards a more dominant Irrawaddy contribution at ~7.3 Ma, which is another indication that this change was induced by climatic factors rather than tectonics, which would have also required longer timescales.

4.3.3 $^{87}Sr/^{86}Sr$ ratios trace chemical weathering intensity

The Sr isotope composition of detrital sediments is influenced by grain-size sorting during transport, changes in contributions from the eroded source rocks, and chemical weathering intensity on land (Blum and Erel, 2003; Tütken et al., 2002). We focus on the clay size fraction, for which sorting differences are minimal (e.g., Carter et al., 2020), to infer changes in source contributions and climatically driven weathering regimes. During the interval from 9 to 5 Ma, Nd and Pb isotope compositions show some variability on 100 kyr time scales and a step change towards more IBR dominated sources at 7.3 Ma, which is not mirrored by the Sr isotope compositions. The $^{87}Sr/^{86}Sr$ ratios remained markedly invariant between 9 and 6 Ma and then increased significantly from 6 to 5 Ma. This decoupling from Nd and Pb patterns indicates that changes of the Sr isotope composition of the late Miocene were not driven by changes in source contribution but more likely by variations in incongruent weathering and in chemical weathering intensity. Clays, in contrast to coarser sediments, incorporate a substantial fraction of the ions dissolved in the water present during their alteration and thus also of their isotopic composition (Bayon et al., 2016). Sr is more susceptible to such changes given that the Sr concentrations in the waters are relatively high compared to those of Nd and Pb (e.g., Indus River: 300 ppb Sr vs. 3.2 ppt Nd; Goldstein and Jacobsen, 1987). During weak chemical weathering, the first mineral phase reacting with water is usually plagioclase, which releases relatively low $^{87}Sr/^{86}Sr$ signatures (Douglas et al., 1995). When chemical weathering becomes stronger, micas release Sr with high $^{87}Sr/^{86}Sr$. This would consequently shift the isotopic composition of the altered clays towards less radiogenic values during weak chemical weathering and towards more radiogenic values during stronger chemical weathering (Derry and France-Lanord, 1996). The marked increase of the Sr isotope composition therefore implies an increase in chemical weathering intensity from 6 to 5 Ma.

Another factor possibly affecting the Sr isotope composition of the secondary clays are variable contributions from weathering of the extremely radiogenic metamorphic core complex of the collision zone of the Himalayas, which comprises lithologies of the High Himalayan Crystalline Series and the Lesser Himalayan Crystalline Series (Vannay et al., 2004). During the collision of India and Asia, high-grade metamorphism and partial melting of the rocks mobilized radiogenic Sr of K-rich minerals into Na- and Ca-rich minerals that weather much more easily (Edmond, 1992).

The erosion of rocks containing these highly radiogenic minerals ($^{87}Sr/^{86}Sr$ >0.720) has been suggested to be responsible for the significant increase in $^{87}Sr/^{86}Sr$ values of the global ocean since 40 Ma (Oliver et al., 2003; Raymo and Ruddiman, 1992; Richter et al., 1992). Even though the weathering of the radiogenic metamorphic core complex represents a possible influence on the Sr isotope composition of our U1443 clays, none of the records point at a particular event responsible for intensified core complex erosion at 6 Ma. As potential indicators, we would have expected shifts of the other isotope systems towards more HHC or LH signatures for example. Since this was not the case, it is most likely that increased chemical weathering intensities were the major factor responsible for the increased Sr isotope signature of the clays.

The lack of $^{87}Sr/^{86}Sr$ change at 7.3 Ma when both Nd and Pb isotopes showed a step change towards more IBR dominated contributions (Fig. 4.2) also implies chemical weathering control on the clay Sr isotopes as the change in provenance was likely overprinted by the weathering effect. Moreover, the radiogenic Sr composition of modern Irrawaddy clays and Brahmaputra sediments are very similar while the Miocene clays are slightly less radiogenic than these (Fig. 4.3), highlighting that Sr isotopes are less useful to track source provenance compared to the particle reactive Nd and Pb because of the high water/rock concentration ratios and the mobility of Sr.

The observed shift in $^{87}Sr/^{86}Sr$ of ~0.003 between 6 and 5 Ma is somewhat smaller than the variability in earlier Miocene intervals recorded by Bretschneider et al. (submitted), who found variations of up to ~0.005 in $^{87}Sr/^{86}Sr$ within only 500 kyr in the middle Miocene. However, the increase in the late Miocene is very prominent, given the constancy of the isotope compositions during the four Myr prior to the change. An increase in $^{87}Sr/^{86}Sr$ with a similar amplitude during this period of time was hinted at in the low resolution data from the companion core ODP Site 758 (Fig. 4.6; Ali et al., 2021). Similar amplitude radiogenic spikes of +0.003 in global average riverine sediment $^{87}Sr/^{86}Sr$ of the last 250 kyr have also been attributed to changes in weathering regime caused by accelerated weathering of biotite following deglaciations (Blum and Erel, 1995). We consequently attribute the observed shift almost entirely to an enhancement in chemical weathering intensity.

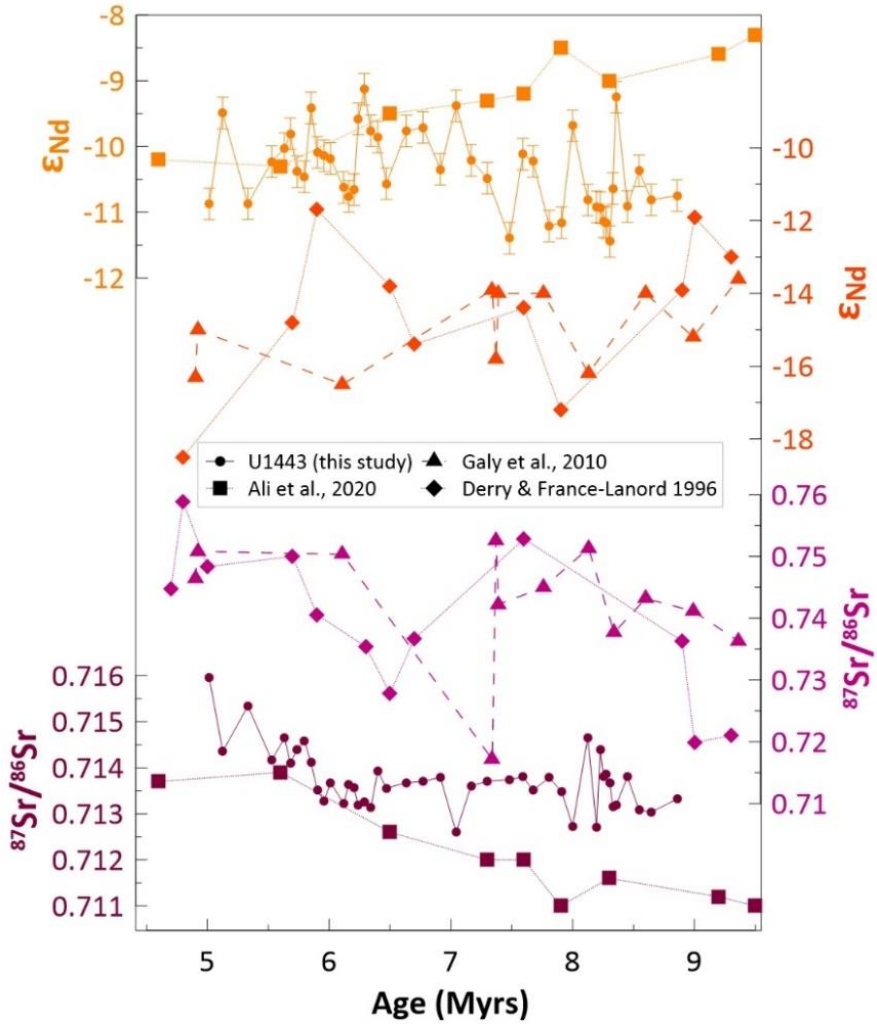

Fig. 4.6: Radiogenic Nd and Sr isotope compositions of U1443 clays compared to literature data. The record of Ali et al. (2021) is on the same scale as the U1443 data, while the records of Galy et al. (2010) and Derry and France-Lanord (1996) are displayed on a larger scale. The large differences in values are a result of the different sample locations and sediment contributions to the Bengal Fan and the NER. The error bars represent the 2 s.d. of the repeated processing and measurement of BHVO-2 and are smaller than the symbols for Sr isotopes.

4.3.4 Monsoon intensity and weathering regimes

The increase in $^{87}Sr/^{86}Sr$ ratios of NER clays from 6 to 5 Ma most likely resulted from an intensification of chemical weathering. An increase in the abundance of the secondary clay mineral smectite at this location in the late Miocene (Ali et al., 2021) supports this hypothesis (Fig. 4.7). However, the increase in smectite abundance was strongest between ~8 and 6.5 Ma to remain at a high level until 5 Ma. Derry and France-Lanord (1996) also observed an increase in smectite abundance compared to primary clay minerals after 7 Ma on the Bengal Fan. They interpreted the high Sr isotope values ($^{87}Sr/^{86}Sr$ increase of ~0.02) to result from intensified chemical weathering of radiogenic silicates. Floodplain weathering, especially of micas containing highly radiogenic Sr, would have produced smectite, and thus may have resulted in more radiogenic Sr isotope signatures of the clays (Derry and France-Lanord, 1996). This also is the most likely explanation for the clear increase in $^{87}Sr/^{86}Sr$ ratios of the U1443 clays after 6 Ma given that these clays are dominated

(>60 %) by secondary smectite. It is therefore possible, that a sea level drop during the late Miocene related to global cooling exposed larger parts of the continents and increased the sizes of floodplains, which are the typical environments accommodating chemical weathering and formation of secondary clays with radiogenic $^{87}Sr/^{86}Sr$ signatures. However, sea level reconstructions for the late Miocene do not show a clear drop, but a sea level similar to today (Kominz et al., 2008). A detailed look at our investigated time interval (e.g., Miller et al., 2005), shows that the variation in sea level was indeed minor compared to the overall sea level evolution of the last 100 Myr, but also indicates that there was a sea level decrease of ~10 to 20 m. Even if the sea level only changed by a few meters, this would have had a big impact on the areas exposed or flooded in Bangladesh, since most of this area has an elevation of less than 10 m above sea level. Small fluctuations and a minor overall decrease in sea level may have enlarged floodplains, enhanced chemical weathering and may have therefore compensated for the expected decrease in chemical weathering and increase in physical erosion due to increased aridity on the continents.

Another factor responsible for expanding floodplains may have been the interplay of high sediment supply, as recorded by the Bengal and Nicobar Fans (Pickering et al., 2020), and grasslands increasing soil thickness. Grassland soils also accommodate much higher internal mineral surface areas prone for weathering compared to woodland or desert soils (Retallack, 2001). Thus, the formation of thick horizons of soils with crumb peds due to the appearance of tall sod grasslands at 7-6 Ma likely accelerated chemical weathering rates (Retallack, 2001). This biological forcing may have contributed to increased chemical weathering intensities seen in the rise in Sr isotope composition and secondary clay abundance.

Most studies (e.g., Huang et al., 2007; Lee et al., 2019; Tripathi et al., 2017) have inferred a reduction in SAM intensity from their Bay of Bengal, Andaman Sea and Arabian Sea records of the late Miocene. If weathering intensity was simply a function of SAM precipitation and temperature then our record apparently does not support this hypothesis since we find an increase in chemical weathering intensity between 6 and 5 Ma. However, the enhanced chemical weathering may be more a result of a large floodplain and a greater surface area available to chemical weathering rather than increased SAM intensity. It has been inferred that precipitation decreased in general (Clift and Webb, 2018; Huang et al., 2007; Miao et al., 2012), while monsoon seasonality increased, which was attributed to strengthening of monsoon winds and increased upwelling in the western Arabian Sea (Gupta et al., 2015; Kroon et al., 1991) and an enhanced winter monsoon as suggested by Holbourn et al. (2018). Therefore, we suggest that despite increasing aridity on land, the seasonally variable monsoon climate provided sufficient humidity to maintain strong chemical weathering. Moreover, reduced precipitation does not necessarily mean less chemical weathering in the floodplains. On the contrary, as discussed above, chemical weathering intensities potentially increased as a result of the emerging C4 grasslands.

4.3.5 Implications for the marine Sr isotope evolution

The rise in U1443 clay Sr isotope compositions coincided with the increase in the gradient of the increase in seawater $^{87}Sr/^{86}Sr$ between 5.5 and 4.5 Ma (Hodell et al., 1989) and between 6.1 and 4.9 Ma recorded at ODP Site 758 (Fig. 4.7; Farrell et al., 1995). This late Miocene/early Pliocene increase in Sr isotope composition was part of the overall increase in marine $^{87}Sr/^{86}Sr$ recorded for the last 40 Myr (Richter et al., 1992). Hodell et al. (1989) related the rise in $^{87}Sr/^{86}Sr$ signature to an increase in dissolved Sr riverine flux to the oceans and/or to an increase in the average Sr isotope composition of river water, which may have been connected to increased chemical denudation rates of the continents and shelves. Derry and France-Lanord (1996) argued for the latter scenario with their record pointing at a decrease in Sr flux and an increase in global mean $^{87}Sr/^{86}Sr$ of rivers due to high weathering intensity. The increase in detrital clay Sr isotope composition in our record as well as in others supports the argument that the change in mean $^{87}Sr/^{86}Sr$ composition of Himalayan river sediments affected the ocean's Sr isotope composition and may therefore at least partly have been responsible for the rise in seawater $^{87}Sr/^{86}Sr$ in the late Miocene/early Pliocene. Since high chemical weathering rates promoted the drawdown of CO_2 and ultimately led to climate cooling, rising Sr isotope compositions in river sediments and in the ocean can also serve as an indicator for a cooling climate, as observed in the time interval between 6 and 5 Ma.

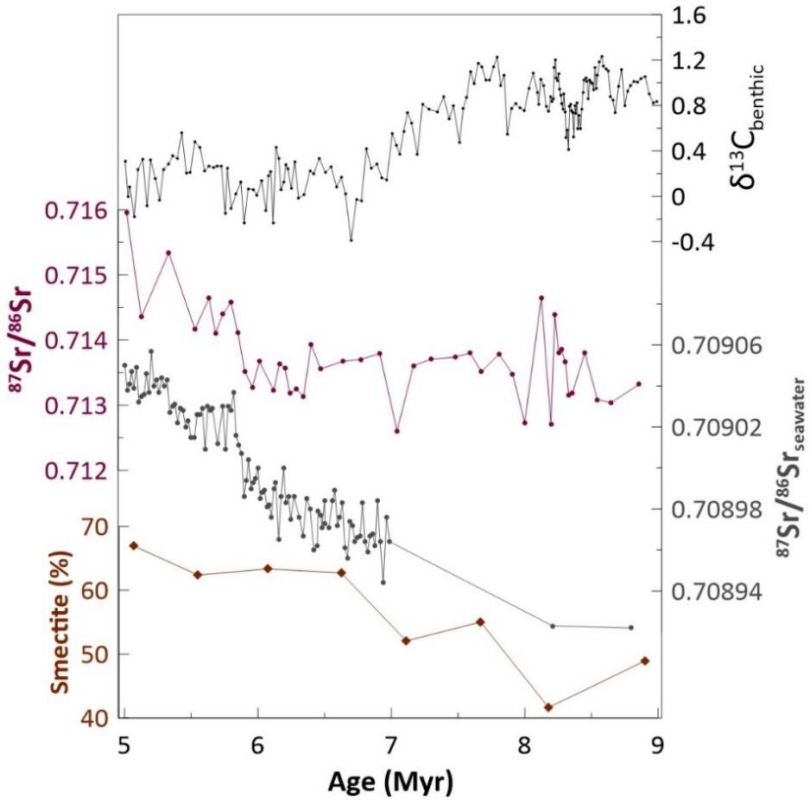

Fig. 4.7: Comparison of benthic $\delta^{13}C$ record (Bolton et al. unpublished; Lübbers et al., 2019), detrital clay Sr isotope composition, seawater Sr isotope evolution from 9 to 5 Ma (Farrell et al., 1995; Hodell et al., 1989) and smectite abundance at ODP Site 758 (Ali et al., 2021). Note the different amplitudes of seawater and clay Sr isotope increases.

4.4 Conclusions

We present a 100 kyr resolution record of radiogenic Sr, Nd, and Pb isotope compositions of detrital clays from IODP Site U1443 in the southern Bay of Bengal. Our record focuses on the late Miocene/early Pliocene from 9 to 5 Ma, a period within the Cenozoic cooling trend marked by extensive environmental changes and intermittent warming. The radiogenic isotopes indicate an overall stable mixture of sources of the Ninetyeast Ridge clays, which include contributions from the High Himalayan Crystalline, the Tethyan Sedimentary Series and the Indo-Burman Ranges. The Himalayan contribution, represented by sediments delivered by the Ganges and Brahmaputra Rivers, became more High Himalayan- or Ganges-dominated than found in earlier Miocene records, which likely reflects an increasing contribution from Lesser Himalayan rocks. A step change in Nd and Pb isotope compositions at ~7.3 Ma, contemporaneous with the global marine benthic $\delta^{13}C$ decline that characterizes global late Miocene carbon cycle changes, reflects higher Irrawaddy contributions connected to a climatically driven eastward shift in precipitation patterns and a more focussed erosion of the Indo-Burman Ranges. The variability of Sr isotope compositions was decoupled from Nd and Pb isotope signatures and rather indicate shifts in the weathering regime. A prominent increase in Sr isotope compositions between 6 and 5 Ma suggests increased chemical weathering in the Ganges-Brahmaputra and Irrawaddy basins as also evident from clay Nd and Pb isotope compositions. The increase in chemical weathering may have resulted from increased exposure of continental shelves due to a lowered sea level and the expansion of C4 grasslands providing a larger mineral surface area for chemical weathering as opposed to an increase in SAM intensity. The rise in the clay $^{87}Sr/^{86}Sr$ signature coincided with the major late Miocene/early Pliocene increase in seawater Sr isotope composition suggesting that the change in the composition of Himalayan riverine inputs due to enhanced chemical weathering intensities may also have affected the global ocean Sr isotope signature between 6 and 5 Ma.

5. Scientific Chapter III

Detrital clay Hf isotope compositions reveal extreme chemical weathering conditions in the drainage basin of the Bay of Bengal during the middle to late Miocene

Abstract

Silicate weathering is a key component in the global carbon cycle and it is crucial to understand its controlling mechanisms and to reconstruct its evolution in the past. This is particularly important during Miocene times, when global climate cooling and Himalayan tectonic events strongly affected the weathering regime of the watersheds feeding into the Bay of Bengal. We applied coupled Nd and Hf isotope compositions of detrital clays from IODP Site U1443 from the southern Bay of Bengal to infer changes in silicate weathering intensities across the middle to late Miocene. Deviations of the ε_{Hf} signatures from the array defined by global clays in ε_{Hf}-ε_{Nd} space ($\Delta\varepsilon_{Hf\ clay}$) of up to 9.78 are the highest values measured to date and suggest prevalence of extreme chemical weathering intensity under tropical warm and wet climate conditions. The preferential release of highly labile mineral phases carrying radiogenic Hf signatures during weathering and the formation of authigenic clays that incorporated highly radiogenic Hf from weathering solutions enriched the clays in radiogenic Hf. Moreover, the extremely high $\Delta\varepsilon_{Hf\ clay}$ signatures are likely related to intense seasonal precipitation brought by the monsoon rains. The evolution of the Hf isotope record over the middle to late Miocene shows a decrease in ε_{Hf} and $\Delta\varepsilon_{Hf\ clay}$ values after ~10 Ma, which is not reflected in the Nd isotopes. This may have resulted from a decrease in monsoon seasonality in response to climate cooling and/or from intensified erosion accompanying global cooling and C4 grassland expansion, which hampered the formation of old, extremely weathered surfaces necessary to generate exceptionally high $\Delta\varepsilon_{Hf\ clay}$ signatures.

5.1 Introduction

Chemical weathering of silicate rocks plays a key role in the Earth's carbon cycle and thus in regulating global climate. Weathering processes in the Himalayas are considered fundamental drivers of Earth's climate because enhanced silicate weathering and the burial of organic carbon in the Bengal Fan sequestered CO_2 and potentially reduced global temperatures during Miocene times (France-Lanord and Derry, 1997; Galy et al., 2007; Galy et al., 2010; Raymo, 1994; Raymo and Ruddiman, 1992). Therefore, reconstructing past variations in silicate weathering is important to understand weathering-climate feedbacks. However, it is difficult to disentangle the silicate weathering intensity signal from changes in source provenance of the weathered material or

physical erosion using geochemical proxies such as radiogenic Sr and Pb isotope compositions (Bayon et al., 2009b).

Over the last decade, the combination of Lu-Hf and Sm-Nd isotope systems has successfully been used to trace silicate weathering. The two isotope systems behave similarly during magmatic processes but there are significant differences on the scale of minerals. Sm and Nd are incorporated in similar proportions in most rock-forming minerals, while Lu and Hf are partitioned differently into mineral phases. This leads to a large degree of fractionation between Lu and Hf during magmatic crystallization and results in minerals exhibiting distinct Hf isotopic compositions. This decoupling between the Lu-Hf and Sm-Nd systems at mineral scale enables the tracing of silicate weathering intensity because different mineral phases with distinct resistance to weathering are affected differently (Bayon et al., 2009b). A large proportion of Hf in crustal rocks is contained in zircons, which are highly resistant to weathering and characterized by very low Lu/Hf ratios. During transport processes, zircons preferentially accumulate in the coarse-grained fractions of sediments (Patchett et al., 1984). This "zircon effect" leads to a significant decoupling between Hf and Nd. If sediments contain large amounts of zircons, their extremely unradiogenic Hf isotope signatures will dominate the Hf isotope composition of the detrital sediment fraction.

On an ε_{Hf} vs. ε_{Nd} diagram, the decoupling between Hf and Nd during surface processes is illustrated by different arrays. The 'terrestrial array' (Vervoort et al., 1999) is the result of the similarity of the Sm/Nd and Lu/Hf systems during magmatic processes. The 'seawater array' (Albarède et al., 1998) reflects the dissolved Hf budget in the ocean and is characterized by more radiogenic Hf isotope compositions for a given Nd isotope composition. These originate from the dissolution of the zircon-free component of continental rocks during weathering and the preferential dissolution of Lu-rich accessory minerals (Bayon et al., 2009b; Bayon et al., 2006; Piotrowski et al., 2000; Van de Flierdt et al., 2007). More recently, Chinese and Mongolian loess and dust records (Chen et al., 2013; Zhao et al., 2014) were combined with world river clay data to define the 'clay array' (Bayon et al., 2016). This array comprises sedimentary rocks mainly composed of weathering products and lies between the terrestrial and the seawater arrays. Incongruent weathering of bulk silicate rocks is the main source of these clays, making the clay array a valuable indicator of terrestrial weathering intensity (Bayon et al., 2016).

Here, we apply the Hf-Nd isotope weathering tracer to middle to late Miocene detrital clays from IODP Site U1443 in the Bay of Bengal to expand the few datasets that exist for tropical environments so far (e.g., Fontanier et al., 2018; Garçon et al., 2013) and to reconstruct past chemical weathering intensity in the Himalayas. The warmer than present Miocene offers a unique window into past South Asian Monsoon (SAM) variability in relation to a changing global climate, weathering and erosion regimes as well as the tectonic evolution of the Himalayas. The detrital clays from the crest of the Ninetyeast Ridge (NER) integrate the weathering and erosion influx from

some of the globally largest rivers draining the Himalayas (Ganges, Brahmaputra, Meghna), the Indo-Burman Ranges (Irrawaddy), and the Indian Peninsula (Godavari, Krishna, Mahanadi) (Fig. 5.1). We base these reconstructions on the existing stratigraphic framework based on benthic $\delta^{18}O$ signatures (Kochhann et al., personal communication; Lübbers et al., 2019; Bolton et al., unpublished) and previously analysed Sr, Nd and Pb isotope compositions of the same clay fractions (Bretschneider et al., submitted; in prep.). These results indicate a generally stable provenance of the clays from the middle to late Miocene, comprising contributions from Himalayan sources like the High Himalayan Crystalline and the Tethyan Sedimentary Series as well as from the Indo-Burman Ranges. A marked change in Sr, Nd, and Pb isotope variability at ~13.5 Ma was related to Himalayan tectonic reorganization and the Miocene global cooling, while transient orbital scale excursions of the radiogenic isotopes reflected changes in both monsoon intensity and weathering regime. The Sr isotope composition served to identify intensified chemical weathering connected to increasingly exposed continental shelves at lowered sea level between 6 and 5 Ma (Bretschneider et al., in prep). With this information already extracted from the clay fraction samples, we now add the Hf isotope system. Coupled to the Nd isotope data we aim to verify the previous interpretations concerning the prevailing weathering processes in the drainage area of the Bay of Bengal and apply the combined detrital clay Hf-Nd isotope compositions as a novel tracer of chemical weathering intensity in warm and humid environments.

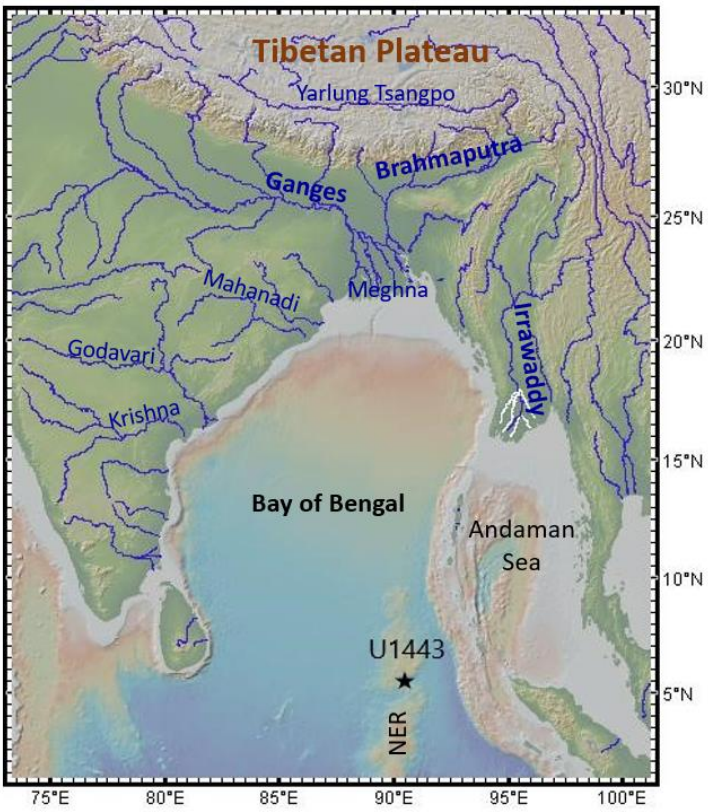

Fig. 5.1: Map of the Bay of Bengal including the major rivers and the location of IODP Site U1443 on the Ninetyeast Ridge (NER)

5.2 Materials & Methods

The sample fractions analyzed in the course of this study are the same as those analyzed and described in Bretschneider et al. (submitted; in prep). The samples originate from IODP Site U1443 on the crest of the NER in the southern Bay of Bengal cored with RV *JOIDES Resolution* during IODP Expedition 353. The age model used in this study is based on astronomically tuned $\delta^{18}O$ and $\delta^{13}C$ measurements of epifaunal benthic foraminifers by Lübbers et al. (2019), K. Kochhann (personal communication) and Bolton et al. (unpublished). The sediment samples were washed over a 63 µm sieve and the fine fraction was collected. While the coarser fraction was used for micropaleontological work, the fine fraction was freeze-dried and leached to remove all authigenic Fe-Mn oxyhydroxides. The leaching procedure was modified from Gutjahr et al. (2007) and the first leach was kept for future analysis of the seawater radiogenic isotope signature. Briefly, ~2 g of fine sediments were washed with deionized water, leached step by step with a 0.05M hydroxylamine hydrochloride–15% distilled acetic acid–0.03M Na-EDTA solution, buffered to pH 4 with analytical grade NaOH, and fully decarbonated with 40% acetic acid. Having been washed again with deionized water, the clay fraction was separated using a centrifuge-based Atterberg method.

For the radiogenic isotope analyses, about 100 mg of the dried silicate clays were completely digested using alkaline fusion ($NaOH$-Na_2O_2), as described in Bayon et al. (2009a) but without addition of TiO_2, Fe_2O_3, or Tm. The use of the alkaline fusion method achieves quantitative dissolution of highly resistant refractory mineral phases such as zircons (Bayon et al., 2009a). After dissolution of the residue in 6 M HCl, standard ion chromatographic procedures were applied to separate and purify Hf. First, HFSEs and REEs were separated using a cation exchange resin (Bio-Rad AG 50W-X8, 200-400 mesh), while most matrix elements were discarded. The Hf was then separated from the other HFSEs. For the first set of samples, Hf was separated using Ln-spec resin following the method of Münker et al. (2001). For most of the remaining samples, the method was then modified and a Bio-Rad AG1-X8 (200-400 mesh) resin was used following the first part of the separation method of Chu et al. (2002).

Hf isotope measurements were performed on a Nu Plasma high-resolution MC-ICP-MS and on a Thermo Scientific Neptune Plus MC-ICP-MS at GEOMAR. Hf isotope ratios were corrected for instrumental mass bias using a $^{179}Hf/^{177}Hf$ of 0.7325. Mass-bias corrected values for $^{176}Hf/^{177}Hf$ were normalized to a JMC 475 value of 0.282163 (Blichert-Toft, 2008; Blichert-Toft and Albarède, 1997). The Hf isotope compositions are provided in the ε_{Hf} notation using $^{176}Hf/^{177}Hf_{CHUR}$ = 0.282785 (Bouvier et al., 2008). Procedural blanks for Hf were 0.3 ng on average and thus below 1 % of the total amount of Hf in the samples. Separate digestions and measurements of USGS reference material STM-1 (n=8) gave a mean ε_{Hf} value of 8.53±0.47, which agrees well with the

mean value (8.36±0.65) reported by the GeoReM database (Jochum et al., 2005). Nd isotope compositions have been determined on the same samples and are discussed in two companion manuscripts (Bretschneider et al., submitted; in prep.). The $\Delta\varepsilon_{Hf\ clay}$ was calculated using ε_{Hf} (clay array) = 0.78 × ε_{Nd} + 5.23 (Bayon et al., 2016).

5.3 Results and Discussion

5.3.1 Hf-Nd isotope composition of U1443 clays in relation to other sediment arrays

The Nd isotope compositions of the samples have already been shown to reflect changes in the relative contributions of the source areas of the sediments supplied by the Ganges, Brahmaputra and Irrawaddy Rivers (Bretschneider et al., submitted; in prep.). The ε_{Hf} signatures vary between 0.59 and 6.21 (Table A7). Combining the Nd and Hf isotope compositions on a cross plot (Fig. 5.2) allows comparison of our results to literature data. Compared to the different sediment arrays described above, our U1443 ε_{Hf} data are significantly more radiogenic than the clay array (Bayon et al., 2016) and for most samples are even more radiogenic than the seawater array (Albarède et al., 1998). Ganges River sediments (Garçon et al., 2013), consisting of both bedload and suspended load show markedly different, less radiogenic Nd and Hf isotope compositions than the clays of our study (Fig. 5.2). The difference in ε_{Nd} values can be explained by different sources: Our clays from the NER only partly consist of Ganges sediments but also contain large contributions from the Brahmaputra and especially the Irrawaddy River, which shift their isotope composition towards more radiogenic Nd isotope compositions (Bretschneider et al., submitted). The large deviation in Hf isotope composition likely results from the different grain sizes of the sediments analyzed. Garçon et al. (2013) analyzed bulk sediments that include coarse-grained, zircon-rich sediments with unradiogenic Hf isotope compositions and thus agree very well with the composition of the terrestrial array (Vervoort et al., 1999). The clay size fraction, as represented by the clay array, reflects the products of incongruent weathering of silicate rocks and contains much smaller amounts of zircons compared to the coarser grained samples, which is enhanced by mineral sorting processes during sediment transport. The more radiogenic Hf isotope composition of the U1443 clays is therefore consistent with grain size and mineral sorting effects. This also implies that Hf isotope signatures of clays are not useful to determine their provenance.

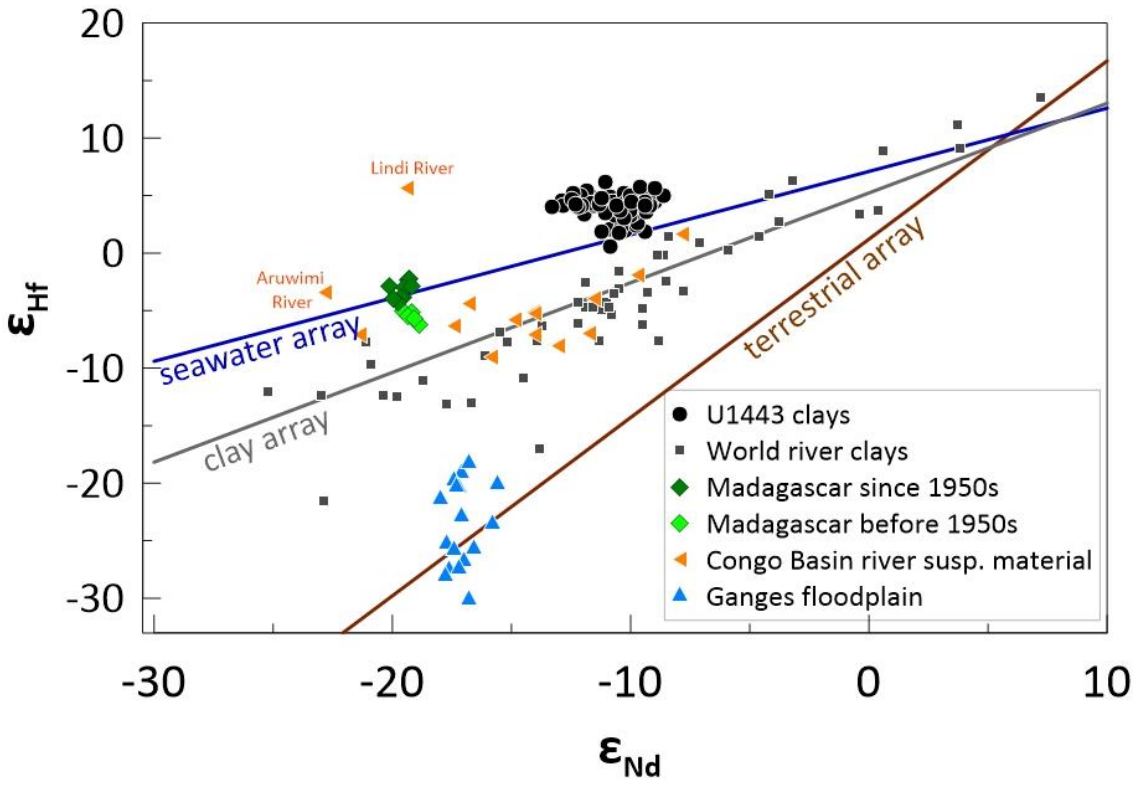

Fig. 5.2: Nd-Hf isotope composition of U1443 clays in relation to the seawater array (Albarède et al., 1998), the clay array (Bayon et al., 2016) and the terrestrial array (Vervoort et al., 1999) as well as records from the Ganges floodplain (Garçon et al., 2013), from Madagascar (Fontanier et al., 2018), from the Congo basin and world river clay data (Bayon et al., 2016).

5.3.2 Factors controlling the Hf isotope composition of river clays

The deviation of the U1443 data from clay array represented by $\Delta\varepsilon_{Hf\ clay}$ values ranges between 3.8 and 9.8. Factors potentially controlling this deviation include the presence of zircons, the lithology of the source rocks, and the climate-driven weathering regime (Bayon et al., 2016).

Even though **zircons** are usually thought to be a minor fraction in clays due to the "zircon effect" (e.g., Patchett et al., 1984; White et al., 1986), the study of Marchandise et al. (2014) inferred an influence even on the Hf isotope composition of finest sediment fractions. However, the presence of zircons in the clays would shift the $\Delta\varepsilon_{Hf\ clay}$ signatures to negative values due to their highly unradiogenic Hf isotope composition. Since our samples all show a positive deviation from the clay array, a significant influence of zircons is highly unlikely.

The **lithology** can also influence the Hf isotope composition by preferentially weathering particular rock types, such as volcanic rocks with high ε_{Hf} signatures or older cratonic rocks with large ingrowth of radiogenic Hf compared to younger rocks. In our study, however, the samples all plot in a tight cluster above the clay array indicating no major changes in source provenance based on

their Nd isotope signatures. Even if some changes in lithologies of the contributing source rocks occurred, this had no major effect on the remarkably high $\Delta\varepsilon_{Hf\ clay}$ values of all U1443 clay samples. The small relative $\Delta\varepsilon_{Hf\ clay}$ variability of our record may indeed reflect some variability in source contributions, which should, however, be reflected by simultaneous changes in the Nd and Hf isotope compositions and will be discussed below.

Weathering regime and climate changes have also been linked to $\Delta\varepsilon_{Hf\ clay}$ variability in a previous study (Bayon et al., 2016). One mechanism frequently observed is that during chemical weathering, labile Lu-rich mineral phases, such as apatite and sphene, are preferentially dissolved and release radiogenic Hf to solution (e.g., Bayon et al., 2016; Bayon et al., 2006; Dausmann et al., 2019). Leaching experiments even showed that this effect persists not only during weak initial stages of chemical weathering but also during advanced stages (Dausmann et al., 2019). The highly radiogenic dissolved Hf signatures are subsequently incorporated into secondary clays, which have been suggested to dominate the NER clay budget (Ali et al., 2021). Consequently, climatic conditions favoring strong chemical weathering would result in more radiogenic Hf isotope compositions of secondary clays and accordingly higher $\Delta\varepsilon_{Hf\ clay}$ values. This relationship is likely a major contributor to the exceptionally high $\Delta\varepsilon_{Hf\ clay}$ values observed in the U1443 clays.

5.3.3 Hf isotopes as paleoenvironmental proxies

Increasing $\Delta\varepsilon_{Hf\ clay}$ values have been shown to be positively correlated to the chemical index of alteration (CIA), mean annual temperature (MAT), and mean annual precipitation (MAP) (Bayon et al., 2016). Especially in warm and humid regions, predicted and observed $\Delta\varepsilon_{Hf\ clay}$ values agree well suggesting that climatic parameters play an important role in controlling Hf and Nd decoupling during clay mineral formation (Bayon et al., 2016). However, in the world river clay data set of Bayon et al. (2016), $\Delta\varepsilon_{Hf\ clay}$ values of up to ~3 represented tropical warm and wet climate conditions (Fig. 5.3). Our results reach $\Delta\varepsilon_{Hf\ clay}$ values of up to 9.78 and are thus markedly higher than any reported modern river data, which, however, did not include any Ganges, Brahmaputra or Irrawaddy River samples. The first order implications therefore are that a very warm and wet climate with strong silicate weathering prevailed in the catchment area of our samples during the Miocene.

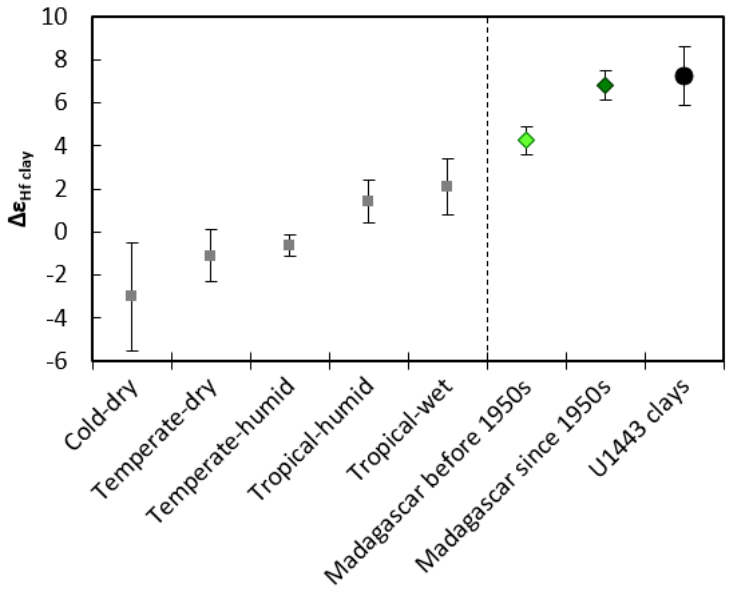

Fig. 5.3: Climate dependence of Hf-Nd isotope decoupling in world river clays (average±1 s.d.) according to Bayon et al. (2016) in comparison to the modern-day Madagascar record before and since the 1950s (Fontanier et al., 2018) and our U1443 clay results.

Ranges of $\Delta\varepsilon_{Hf\ clay}$ values similar to ours have been obtained from a sediment core record just off NW Madagascar (Fig. 5.3; Fontanier et al., 2018). The measured $\Delta\varepsilon_{Hf\ clay}$ signature increased since the 1950s, exhibiting values between ~6 and 7.6, thus also strongly deviating from the clay array to more radiogenic ε_{Hf} values overlapping with the seawater array (Fig. 5.2). While the values of the clays prior to the 1950s were on average only slightly above the typical signatures of world rivers from tropical wet environments, the clays deposited since the 1950s exhibit $\Delta\varepsilon_{Hf\ clay}$ values on the same high level as our U1443 clays (Fig. 5.3). The ε_{Nd} signatures remained constant at the same time suggesting a stable sediment source. The increasing $\Delta\varepsilon_{Hf\ clay}$ values were attributed to significantly enhanced soil erosion associated with increased tropical cyclone intensity and deforestation (Fontanier et al., 2018). The intensified tropical cyclones over NW Madagascar led to heavy rainfall and floods and thus triggered landslides and intense erosion from deforested areas and likely led to an increased frequency of erosional storm surges (Fontanier et al., 2018). From the Congo basin dataset, most river samples plot around the clay array except for two samples, which deviate considerably towards more radiogenic ε_{Hf} values. The Lindi and Aruwimi River clays are characterized by exceptionally high $\Delta\varepsilon_{Hf\ clay}$ signatures of 15.5 and 9.1, respectively (Fig. 5.2). The difference of those two samples compared to the others is their origin in the regions with the highest proportions of metamorphic rocks, with the highest precipitation rates and with soils containing significant proportions of lixisols, which are highly erodible soils typically forming in old landscapes with tropical climate (Bayon et al., 2018). The metamorphic source may indicate multiple cycling of the parent material, which may be a prerequisite for producing the highly weathered sediments enriched in radiogenic Hf isotopes.

Transferring those results from Madagascar and the Congo basin to our record suggests that the generation of such high $\Delta\varepsilon_{Hf\ clay}$ signatures requires the combination of highly weathered sediments and substantial erosion, preferentially in tropical environments with intense, possibly seasonal precipitation. Therefore, the interplay of tropical climate, large floodplains and seasonal monsoon rains promoting intense silicate weathering and erosion likely led to high ε_{Hf} values of the clay fraction on the NER and the resulting high $\Delta\varepsilon_{Hf\ clay}$.

One additional possible mechanism to explain the very high $\Delta\varepsilon_{Hf\ clay}$ values may be the influence of Lu-rich phosphate cycling (Bayon et al., 2016). Weathering of poorly resistant accessory minerals such as allanite and apatite leads to the formation of secondary phosphate minerals in soils. While these minerals are known to sequester REE and Th in soils (Banfield and Eggleton, 1989), Bayon et al. (2016) speculated that they likely also incorporate large fractions of radiogenic Hf released incongruently during incipient chemical weathering. The alteration of these potentially highly radiogenic secondary phosphate minerals under intense weathering conditions may also contribute to the incorporation of highly radiogenic Hf phases into secondary clays, which would subsequently have been eroded and transported to the Bay of Bengal (Bayon et al., 2016). This hypothesis has not been proven so far but would constitute an additional mechanism to enrich the clay mineral phases in radiogenic Hf and help to explain the extremely high $\Delta\varepsilon_{Hf\ clay}$ values of our clay samples.

5.3.4 Hf and Nd isotope evolution in the middle to late Miocene

The evolution of Hf and Nd isotope compositions over the Miocene is displayed in Fig. 5.4. The variability in ε_{Nd} values that is attributed to changes of the sediment sources decreases after 13.5 Ma, which was related to Himalayan tectonic reorganization as well as to global cooling (Bretschneider et al., submitted). The ε_{Hf} signatures were generally high (>3, average 4.42) between 15.8 and 8 Ma and then revealed a step change to lower values between 8 and 5 Ma (Fig. 5.4). Some of the shorter-term variations in the Nd and Hf isotope records appear to have occurred at the same time. This implies at least some source driven control on the Hf isotope composition. Similar to the other radiogenic isotope systems investigated (Sr, Nd, Pb; Bretschneider et al., submitted), the Hf isotopes exhibit the highest variability in the middle Miocene section of the record (Fig. 5.4), which was likely driven by short millennial scale changes in the contributions from different sources. However, it is noted that the resolution of the ε_{Hf} record for the time intervals between 15.8 and 12.8 Ma is much higher than for the younger parts of the record suggesting that some variability in the younger intervals may not have been recorded due to the lower sampling resolution.

With these limitations in mind, it is more instructive to look at the general trends of the Hf and Nd isotope records, which reveal significant differences. The overall decrease in ε_{Hf} signatures between 8 and 5 Ma is not mirrored by the Nd isotopes, which remain at an essentially constant level during the period between 13 and 5 Ma. This decoupling between the Nd and Hf isotopes during the late

Miocene, points to an additional factor controlling the Hf isotope composition apart from the source provenance changes, which are the main factor affecting the Nd isotope compositions. So how can the decrease in ε_{Hf} and $\Delta\varepsilon_{Hf\ clay}$ be explained? Compared to other data such as the world river clays (Bayon et al., 2016), the $\Delta\varepsilon_{Hf\ clay}$ values were still extremely high in the late Miocene, but decreased compared to the middle Miocene values. This implies persistently strong chemical weathering conditions under tropical warm and wet climate conditions but reduced erosion of highly weathered material. The Late Miocene is known to have been a part of the Cenozoic cooling trend accompanied by extensive environmental and ecosystem changes such as aridification and the expansion of C4 plants on land (An et al., 2001; Herbert et al., 2016; Holbourn et al., 2018; Huang et al., 2007; Quade et al., 1989). Various studies have inferred a decrease in South Asian Monsoon intensity and an increase in the strength of physical erosion at that time (Clift et al., 2008; Huang et al., 2007; Lee et al., 2019). Physical erosion is known to promote the disintegration of zircons and other more resistant minerals (e.g., feldspars, biotite) containing unradiogenic Hf isotope compositions. Thus, the release of less radiogenic Hf to solution may form secondary weathering products with less radiogenic Hf isotope compositions. If these processes were indeed enhanced during the late Miocene, they were likely responsible for the overall decrease in both ε_{Hf} and $\Delta\varepsilon_{Hf\ clay}$. However, this mechanism has so far only been described in glaciated regions for sediments that experienced physical erosion by glacier grinding and disaggregation by freeze-thaw processes (e.g., Bayon et al., 2006; Gutjahr et al., 2014; Piotrowski et al., 2000; van de Flierdt et al., 2002). Moreover, records from the Bengal Fan (Derry and France-Lanord, 1996) and the NER (Ali et al., 2021; Bretschneider et al., in prep.) suggest a high chemical weathering intensity persisting even in the late Miocene as inferred from increasing secondary clay abundances (especially smectite) and more radiogenic Sr isotope compositions. We therefore conclude that the disintegration of more resistant minerals releasing unradiogenic Hf was likely not the main process driving the decrease in the Hf isotope composition of the U1443 clays.

The contemporaneous decline in benthic $\delta^{13}C$ and $\Delta\varepsilon_{Hf\ clay}$ and ε_{Hf} values after ~8 Ma (Fig. 5.4) suggests that the two are directly related. The expanding grasslands that were associated with the benthic $\delta^{13}C$ decrease and which led to the development of thick, easily weatherable soil horizons may provide a possible link. As inferred from the Madagascar and Congo basin records, the extremely high $\Delta\varepsilon_{Hf\ clay}$ values likely resulted from the erosion and transport of strongly weathered sediments. When climate cooled and became more arid during the late Miocene, floodplain weathering intensity remained strong but the surfaces eroded may not have become as old anymore. The increasing erosion and the easily erodible soils may have resulted in a landscape that could not produce these old and extremely weathered sediments needed to produce the extreme $\Delta\varepsilon_{Hf\ clay}$ signatures before they were eroded and removed. This process may ultimately have resulted in the decrease in $\Delta\varepsilon_{Hf\ clay}$ and ε_{Hf} values.

Another possible factor responsible for the decrease in $\Delta\varepsilon_{Hf\ clay}$ may be a lower monsoon seasonality, especially when associated with precipitation changes. As suggested with the Madagascar record (Fontanier et al., 2018), the high $\Delta\varepsilon_{Hf\ clay}$ values may also result from extreme seasonality and storm events in a tropical environment eroding material that was intensely chemically weathered. If $\Delta\varepsilon_{Hf\ clay}$ can indeed serve as a proxy for seasonality, this would suggest that the SAM seasonality was more pronounced in the middle Miocene intervals and then decreased after 12.8 Ma and again after 8 Ma. These changes may therefore be connected to global cooling (e.g., Holbourn et al., 2018) and the suggested decrease in SAM intensity (Clift et al., 2008; Huang et al., 2007; Lee et al., 2019).

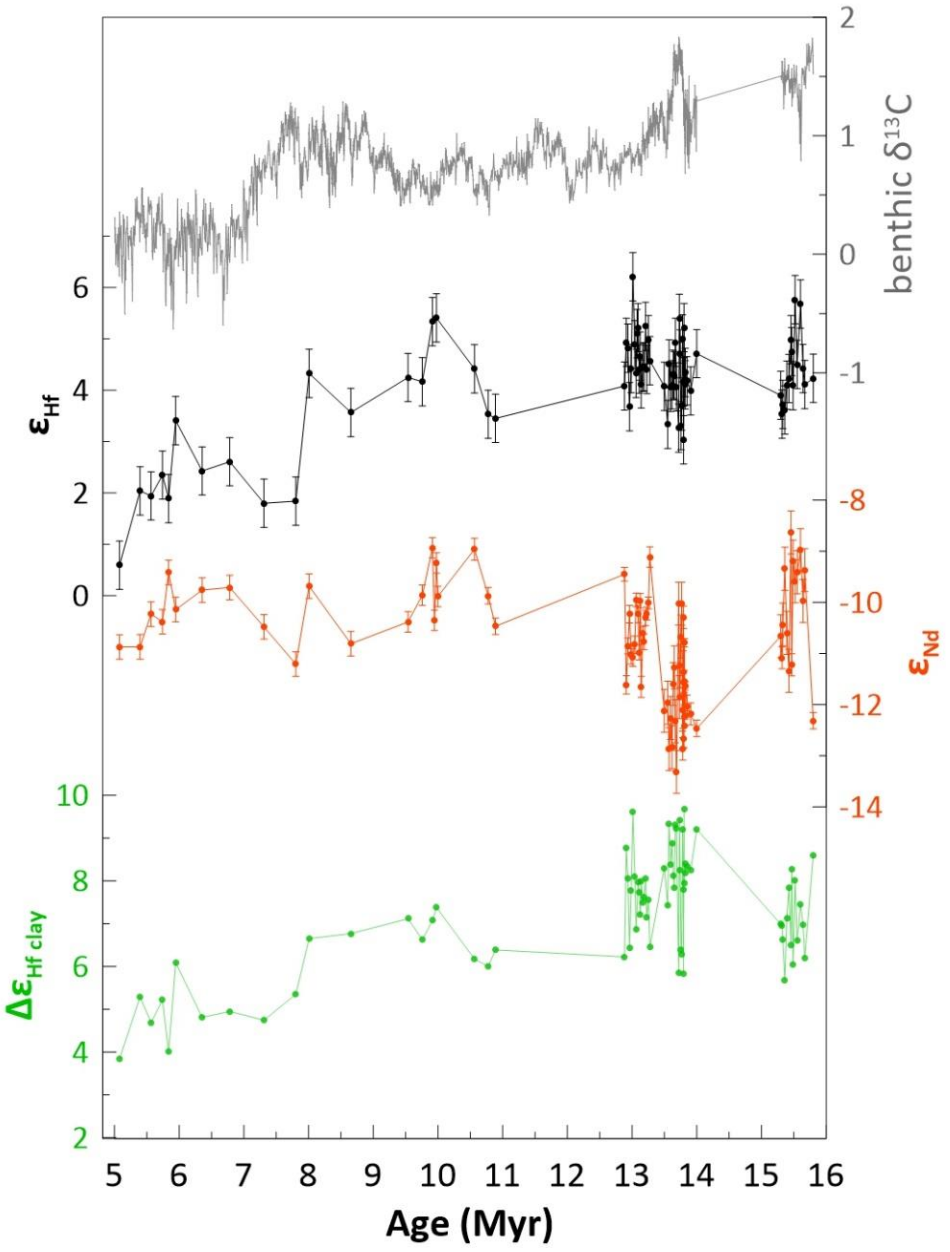

Fig. 5.4: Evolution of benthic $\delta^{13}C$ isotopes (grey; Lübbers et al., 2019; Bolton et al., unpublished; Kochhann et al., personal communication), ε_{Hf} (black) and ε_{Nd} (orange) of U1443 clays over time together with $\Delta\varepsilon_{Hf\ clay}$ (green), which reflects the deviation of individual ε_{Hf} signatures of the samples from the clay array (Bayon et al., 2016).

5.4 Conclusions

The variability of the Hf isotope composition of detrital clays deposited in the Bay of Bengal over the middle to late Miocene period provides important paleo-environmental information on changes in the weathering regime in its catchments. The highest $\Delta\varepsilon_{Hf\ clay}$ values ever recorded to date are interpreted to represent intense chemical weathering in a tropical environment in the catchment area due to the preferential erosion and dissolution of labile mineral phases such as apatite and sphene containing highly radiogenic Hf isotope compositions. Phosphate cycling in the intensely weathered soils potentially contributed to the more radiogenic Hf isotope signatures of authigenic clays. Moreover, comparison with sedimentary data from Madagascar (Fontanier et al., 2018) suggests that the observed extremely high $\Delta\varepsilon_{Hf\ clay}$ values preferentially occur in tropical environments experiencing intense seasonal precipitation like tropical cyclones or, in the case of our study, monsoon rains. Our records of Site U1443 documents highly radiogenic ε_{Hf} and correspondingly high $\Delta\varepsilon_{Hf\ clay}$ values over the entire middle to late Miocene, but also reveals a clear decrease towards the late Miocene. This may have resulted from increased erosion of the floodplains due to global cooling and aridification and the associated expansion of grasslands. The strong erosion impeded the formation of old and extremely weathered material necessary for the unusually high $\Delta\varepsilon_{Hf\ clay}$ signatures in the middle Miocene, because the sediment was eroded too fast. Another possible explanation may be a decreased monsoon seasonality in response to a globally cooling climate.

6. Summary, Conclusions and Outlook

6.1 Summary and Conclusions

This thesis presents a middle to late Miocene record of the radiogenic Sr, Nd, Hf and Pb isotope compositions of detrital clays obtained from IODP Site U1443 in the southern Bay of Bengal. Tectonics, climate and regional monsoon strength controlled weathering and erosion regimes of the watersheds feeding into the Bay of Bengal and these factors played an important role in the global climate evolution via carbon cycle feedbacks. Radiogenic isotope compositions that were used to infer the provenance and the prevailing weathering regime of the sediments supplied to the Ninetyeast Ridge, are affected by all these factors on different timescales. Therefore, the approach of this thesis was to disentangle the roles of climate, tectonics, monsoon strength and weathering and erosion intensity using multiple isotope systems and higher temporal resolution records than in previous studies to advance the understanding of major controls of past SAM intensity. The study of orbital-resolution intervals of the middle Miocene (15.8-9.5 Ma) as well as of a 100 kyr resolution record of the late Miocene (9-5 Ma) now allows to distinguish between tectonic and climatic forcing of changes recorded in the detrital clay radiogenic isotope record. The high resolution of individual intervals even allowed the identification of orbital cycles in radiogenic isotopes in the Miocene for the first time. The use and combination of multiple isotope systems to trace the sources of detrital sediments and the weathering regime provided insights that were not accessible by single isotope systems. The coupling of Nd and Hf isotope systems was applied as a novel tracer of silicate weathering and provides new insights into tropical environmental changes.

Major findings achieved in this doctoral thesis are summarized as follows:

- The combination of Sr, Nd and Pb isotope compositions demonstrated that the mix of clay sources contributing to the Ninetyeast Ridge remained largely invariant throughout the middle to late Miocene despite major tectonic reorganizations in the Himalayas. This mixture consisted of contributions from the High Himalayan Crystalline, the Tethyan Sedimentary Series and the Indo-Burman Ranges.
- A marked decrease in detrital Sr, Nd and Pb isotope variability at ~13.5 Ma right after the middle Miocene global cooling step was attributed to a major restriction in the supply of High Himalayan erosion products. The change in variability coincided with the tectonic reorganization of thrusting, which shifted the main orographic barrier to the south. While tectonic reorganization likely had some background influence, the relatively short period of 200 kyr, in which most of the change happened, argues for global climate cooling being the primary driver for the decrease in radiogenic isotope variability at Site U1443. The cooling likely had a major impact on precipitation patterns, moving peak precipitation towards the

frontal domains of the Himalayas and the Indo-Burman Ranges thereby reducing inputs from the High Himalayas.

- Transient orbital-scale fluctuations of the radiogenic isotope compositions were mainly triggered by climatically-driven changes in the balance of source contributions. The major control on those short-term fluctuations were likely shifts of weathering regimes on land as a consequence of changes of the locus of peak monsoon precipitation between higher and lower elevations. This is supported by the presence of a significant 30 kyr periodicity in the Nd isotope record, a heterodyne typically associated with monsoon variability, whereas the identified 100 kyr eccentricity cycles in the record likely reflect sea level changes controlling the spatial variation of the extent of the floodplains.
- A step change in Nd and Pb isotope compositions at 7.3 Ma indicates a provenance switch of the clays transported to Site U1443. Irrawaddy River contributions became more dominant while Himalayan contributions supplied by the Ganges and Brahmaputra Rivers decreased. The change was simultaneous with the global benthic $\delta^{13}C$ decline, which was mainly driven by C4 plant expansion on land. Global cooling and increasing aridity likely resulted in an eastward shift of precipitation patterns leading to a more focussed erosion of the Indo-Burman Ranges.
- A late Miocene increase in $^{87}Sr/^{86}Sr$ between 6 and 5 Ma was decoupled from Nd and Pb isotope signatures and likely indicates an increase in the chemical weathering intensity in the Ganges-Brahmaputra and Irrawaddy basins. This may have resulted from increased exposure of the continental shelves due to a lowered sea level and the expansion of C4 plants, which generated thick, easily weatherable soils. Given that this change was coincident with the major late Miocene increase in seawater Sr isotope composition, it is likely that the change in the composition of Himalayan riverine inputs due to enhanced chemical weathering may also have affected the global ocean Sr isotope signature.
- To better disentangle the silicate weathering intensity signal from changes in source provenance within the detrital clay material, Nd and Hf isotope compositions were combined, and their deviation from the global clay array (expressed as $\Delta\varepsilon_{Hf\ clay}$) was applied to provide additional important paleo-environmental information on changes in the weathering regime. This relatively new proxy indicated highly intense chemical weathering in the catchment area recorded by some of the highest $\Delta\varepsilon_{Hf\ clay}$ values measured to date. Comparison to similar records from Madagascar and the Congo basin suggests that these extreme values were likely generated by a combination of highly weathered sediments and substantial erosion in tropical environments with intense and seasonal precipitation, in this context represented by seasonal monsoon rains affecting the floodplains surrounding the Bay of Bengal.

The Hf isotope evolution shows a decrease towards the late Miocene, which likely was a result of global cooling and aridification as a consequence of decreasing monsoon seasonality and/or intensified erosion due to associated grassland expansion. Strong erosion may have prevented the formation of these very old and extremely weathered surfaces, which were likely a prerequisite for the exceptionally high $\Delta\varepsilon_{Hf\ clay}$ values found in the Bay of Bengal sediments.

6.2 Outlook

While this thesis provided new insights into the interplay of climate, tectonics, regional monsoon strength and the weathering and erosion regimes surrounding the Bay of Bengal during the middle to late Miocene, it also left important questions to be answered and raised new issues that will need to be addressed in the future.

The key intervals of the middle Miocene studied at high resolution made it possible to detect orbital cyclicity in the radiogenic isotope record, which is an important indicator of clay isotope variability caused by changes in monsoon strength, which in turn is associated with climate. However, this was only possible for one 500 kyr interval at the highest resolution of <10 kyr achieved by our Miocene record. While ~30 kyr and 100 kyr cycles were possible to be detected and are statistically significant, the resolution of the clay isotope data was generally not sufficient to resolve precessional cyclicity, even though there was a hint of such as a signal (>80% confidence level) in the Nd isotope data. A strong precessional signal has been observed in clay mineralogical variations of late Quaternary sediments from the Andaman Sea (e.g., Colin et al., 1999; Colin et al., 2006). It would therefore be interesting to see if precessional cyclicity exists int the clay isotope record at increased resolution of <5 kyr. Moreover, the resolution of the other intervals could be increased in order to be able to check for the presence of orbital periodicities in those intervals as well. For example, it would be interesting to see whether the marked decrease in Sr, Nd and Pb isotope variability at ~13.5 Ma is also associated with a change in cyclicity. Therefore, the second cooling interval between 13.3 to 12.8 Ma would be one interval to investigate at higher resolution. Moreover, the interval between 10 and 9.5 Ma has been recognised to exhibit a shift from dominant precessional to 41 kyr obliquity cycles recorded in the benthic $\delta^{18}O$ record from ODP Site 1146 (Holbourn et al., 2013). The presence or absence of such a change in cyclicity in the detrital clay isotope record would allow new insights into the factors controlling this change. The reasons for the late Miocene increase in $^{87}Sr/^{86}Sr$ between 6 and 5 Ma could also be further constrained applying spectral analysis to a high resolution record. If sea level affecting the spatial variation of floodplain extent was a controlling factor, we would expect to see 100 kyr eccentricity cycles in the record, while 30 kyr periodicity would rather point at monsoon strength being the dominant control. In addition to the individual intervals, it would also be interesting to close the gaps between the time

slices to have a more complete picture of the radiogenic isotope evolution throughout the middle to late Miocene.

Furthermore, the radiogenic isotope record could be extended back to the Oligocene/Miocene boundary. The interval around the Mi-1 glaciation is particularly interesting in terms of timing of monsoon initiation and work on those samples to obtain the radiogenic isotope compositions is already ongoing. If the monsoon did initiate as early as the Eocene as proposed by Licht et al. (2014), we would expect to see similar radiogenic isotope compositions to the intervals already studied, while the signal may have been markedly different prior to monsoon initiation.

First measurements of the authigenic ε_{Nd} signal representing the dissolved bottom water composition have already been conducted on mixed planktic foraminifera as well as on bulk sediment leachates for two intervals, indicating that the authigenic Nd isotope compositions varied with changing detrital clay ε_{Nd}. This comparison can provide information about how the sedimentary flux of Nd to bottom water varied in the past and when the delivery of sediments from the Himalayas initiated glacial-interglacial type variations in the Nd isotope composition of Bay of Bengal bottom waters (Burton and Vance, 2000; Stoll et al., 2007). Thus, the combination of authigenic and detrital clay ε_{Nd} signals of early Miocene deposits may possibly also provide valuable information on monsoon initiation and its linkage to changes in ocean circulation.

We compared our high resolution record from 14 to 13.5 Ma to monsoon strength proxies from the South China Sea (Holbourn et al., 2010), because data from the Bay of Bengal for the Miocene were lacking. To resolve this deficit and to get an idea about the regional climate signal and compare it to the clay radiogenic isotope proxies, it is important to reconstruct sea surface temperature changes of the Bay of Bengal. This is important because the Bay of Bengal is an important source of moisture for the summer monsoon, while salinity changes associated with fresh water input can be directly related to monsoon precipitation. Paired $\delta^{18}O$ and Mg/Ca measurements on planktic foraminifera would provide this information which ultimately serves as a more direct proxy for monsoon strength. These records already exist for the late Miocene (e.g., Jöhnck et al., 2020) and will be difficult to obtain for the middle to late Miocene period of the carbonate crash (~13.2 to ~8.7 Ma; Lübbers et al., 2019) due to strong dissolution of the carbonates. Nevertheless, before and during the Miocene Climatic Optimum, foraminifera are preserved and first results on planktic foraminifera samples look promising in providing some insights into regional climate evolution.

We have compared the radiogenic isotope compositions to low resolution clay mineral data from ODP Site 758 obtained by Ali et al. (2021). The ratio between primary and secondary clay minerals gives important insights into the prevailing weathering regimes of the catchment areas and it thus provides important constraints for the interpretation of the Sr isotope data or $\Delta\varepsilon_{Hf\ clay}$ data, which trace weathering intensities. A high resolution clay mineral record for the same sample suite as our

radiogenic isotope record will be particularly interesting for periods of marked changes in $^{87}Sr/^{86}Sr$ and $\varepsilon_{Hf\ clay}$, such as the late Miocene. A clay mineral record is currently being produced and will hopefully reduce some uncertainties of the weathering regime interpretations. To get additional constraints on the silicate weathering intensities prevailing in the catchment areas, the analysis of further isotope systems is an option. For example, silicon ($\delta^{30}Si$) and lithium ($\delta^{7}Li$) isotope compositions of the silicate fraction have previously been used to as paleo-weathering and paleo-climate proxies (e.g., Bayon et al., 2018; Dellinger et al., 2014).

Coupled Nd and Hf isotope compositions expressed as $\Delta\varepsilon_{Hf\ clay}$ also provided new insights into silicate weathering intensities and are a very promising proxy. Given that it is still relatively new and only few investigations of this proxy so far focused on tropical environments, it would be very helpful to gain further knowledge of how $\Delta\varepsilon_{Hf\ clay}$ behaves in different weathering environments and refine it using samples spanning a range of clay mineralogical compositions. This could then also be used to better constrain whether we are recording the weathering intensity of the latest weathering cycle or rather that of previous weathering cycles forming sedimentary rocks which were repeatedly weathered.

Another important issue to strengthen our results would be to better constrain the river endmembers. We mostly used mostly modern-day bulk river sediments to compare our data to, which is reasonable given that grain size effects are small compared to the isotopic range of the rocks in the source areas. Nevertheless, measuring clay isotope ratios from sediments at the mouth or upstream of those rivers could strengthen our arguments. The availability of this clay isotope information for the Irrawaddy River endmember greatly helped constraining the source contributions. Furthermore, it could be useful to obtain sediment samples from smaller catchments of the Himalaya and to analyse those for radiogenic isotopes. Having a more detailed picture of the smaller river catchments could provide a better understanding of how the locations of rainfall patterns changed over time and thereby also of the variability of regional erosion supplying sediments to the Bay of Bengal.

Danksagung

Als erstes möchte ich meinen beiden Betreuern, Martin Frank und Ed Hathorne danken. Ed, du hast diese Doktorarbeit überhaupt erst ermöglicht und ich danke dir für die vielen Ideen mit denen du das Projekt stets vorangetrieben hast, die wissenschaftlichen Diskussionen und den Enthusiasmus, den du immer wieder an den Tag legst. Martin, auch du hast mir jederzeit mit Rat und Tat zur Seite gestanden, deine Tür war immer offen und ich danke dir für die viele Unterstützung und dass du jederzeit einen guten Überblick über das Projekt bewahrt hast. Außerdem möchte ich euch beiden danken, dass ihr mir die Möglichkeit gegeben habt, so viele Erfahrungen während der Doktorandenzeit zu machen, die mich in die unterschiedlichsten Ecken der Erde gebracht haben.

Merci beaucoup Germain Bayon for agreeing to be the second examiner of this thesis!

Thank you, Clara Bolton, for the collaboration and inviting me to stay in Aix for one month.

Danke auch an Ann, Wolfgang, Karlos, Julia, Janika und Rasmus von der Uni Kiel für angeregte Diskussionen und die Kooperation. Außerdem möchte ich Daniel danken, der mir mit den Spektralanalysen sehr geholfen hat.

Ein großer Dank geht an Jutta, du bist im Labor unersetzlich und ohne dich hätte es auch viel weniger Spaß gemacht. Du bist immer da, wenns irgendwo klemmt und tüftelst mit Begeisterung neue, kreative Ideen aus, um die Laborabläufe noch weiter zu verbessern.

Vielen Dank an Huang, Marcus und Antao, die mir beim Messen an der Neptune sehr geholfen haben, außerdem Chris für die Einweisung an der Nu. Danke Sasha, dass du mich ganz am Anfang im Labor eingearbeitet hast. Außerdem möchte ich natürlich auch den HiWis danken, die an dieser Arbeit beteiligt waren: Vielen Dank Julian, Orlando und Edel.

Weiterhin möchte ich mich bei den vielen Personen bedanken, die die Zeit am GEOMAR so besonders gemacht haben. Allen voran unser großartiger Flur 8C, vielen Dank Jacky, Lara, Sarina, Katriina, Peer, Steini und Stefan für die Gespräche zwischendurch und die ein oder andere Kaffeepause. Großer Dank auch an Steffen, der regelmäßig dafür gesorgt hat, dass ich ein bisschen Wind um die Ohren bekomme. Danke Barbie, für die Schokobon-Versorgung. Danke Anna, Georgi, Kristin, Eleni, Sonja, Yang, Anne, Martina, Guillaume, Zhouling, Meike, Sebi und Felix.

Danke an Lasse und Christin, unsere Harmi-WG hat mich in dieser Zeit immer wieder auf andere Gedanken und zum Lachen gebracht.

Als letztes möchte ich mich bei meinen Eltern und meiner Schwester für die konstante Unterstützung und Motivation und das Vertrauen in mich bedanken.

References

Ahmad, S.M., Anil Babu, G., Padmakumari, V.M., Dayal, A.M., Sukhija, B.S., Nagabhushanam, P., 2005. Sr, Nd isotopic evidence of terrigenous flux variations in the Bay of Bengal: Implications of monsoons during the last ~34,000 years. Geophysical Research Letters 32.

Ahmad, S.M., Padmakumari, V., Babu, G.A., 2009. Strontium and neodymium isotopic compositions in sediments from Godavari, Krishna and Pennar rivers. Current science, 1766-1769.

Albarède, F., Simonetti, A., Vervoort, J.D., Blichert-Toft, J., Abouchami, W., 1998. A Hf-Nd isotopic correlation in ferromanganese nodules. Geophysical Research Letters 25, 3895-3898.

Ali, S., Hathorne, E.C., Frank, M., 2021. Persistent Provenance of South Asian Monsoon induced silicate weathering over the past 27 million years. Paleoceanography and Paleoclimatology, submitted.

Ali, S., Hathorne, E.C., Frank, M., Gebregiorgis, D., Stattegger, K., Sumpf, R., Kutterolf, S., Johnson, J.E., Giosan, L., 2015. South Asian monsoon history over the past 60 kyr recorded by radiogenic isotopes and clay mineral assemblages in the Andaman Sea. Geochemistry, Geophysics, Geosystems 16, 505-521.

Allen, M.B., Armstrong, H.A., 2012. Reconciling the Intertropical Convergence Zone, Himalayan/Tibetan tectonics, and the onset of the Asian monsoon system. Journal of Asian Earth Sciences 44, 36-47.

An, Z., Kutzbach, J.E., Prell, W.L., Porter, S.C., 2001. Evolution of Asian monsoons and phaseduplift oftheHimalaya±Tibetan plateau since Late Miocene times. Nature 411, 62-66.

Awasthi, N., Ray, J.S., Singh, A., K., Band, S., T., Rai, V.K., 2014. Provenance of the Late Quaternary sediments in the Andaman Sea: Implications for monsoon variability and ocean circulation. Geochemistry, Geophysics, Geosystems 15, 3890–3906.

Baker, J., Peate, D., Waight, T., Meyzen, C., 2004. Pb isotopic analysis of standards and samples using a 207Pb–204Pb double spike and thallium to correct for mass bias with a double-focusing MC-ICP-MS. Chemical Geology 211, 275-303.

Banerjee, B., Masood Ahmad, S., Babu, E.V.S.S.K., Padmakumari, V.M., Kumar Beja, S., Satyanarayanan, M., Keshav Krishna, A., 2019. Geochemistry and isotopic study of southern Bay of Bengal sediments: Implications for provenance and paleoenvironment during the middle Miocene. Palaeogeography, Palaeoclimatology, Palaeoecology 514, 156-167.

Banfield, J.F., Eggleton, R.A., 1989. Apatite replacement and rare earth mobilization, fractionation, and fixation during weathering. Clays and Clay Minerals 37, 113-127.

Barker, R., Herdt, R.W., Rose, B., 1985. The Rice Economy of Asia. Modern Asian Studies 21, 201-204.

Bayon, G., Barrat, J.A., Etoubleau, J., Benoit, M., Bollinger, C., Révillon, S., 2009a. Determination of Rare Earth Elements, Sc, Y, Zr, Ba, Hf and Th in Geological Samples by ICP-MS after Tm Addition and Alkaline Fusion. Geostandards and Geoanalytical Research 33, 51-62.

Bayon, G., Burton, K.W., Soulet, G., Vigier, N., Dennielou, B., Etoubleau, J., Ponzevera, E., German, C.R., Nesbitt, R.W., 2009b. Hf and Nd isotopes in marine sediments: Constraints on global silicate weathering. Earth and Planetary Science Letters 277, 318-326.

Bayon, G., Delvigne, C., Ponzevera, E., Borges, A., Darchambeau, F., De Deckker, P., Lambert, T., Monin, L., Toucanne, S., André, L., 2018. The silicon isotopic composition of fine-grained river sediments and its relation to climate and lithology. Geochimica et Cosmochimica Acta 229, 147-161.

Bayon, G., Skonieczny, C., Delvigne, C., Toucanne, S., Bermell, S., Ponzevera, E., André, L., 2016. Environmental Hf–Nd isotopic decoupling in World river clays. Earth and Planetary Science Letters 438, 25-36.

Bayon, G., Toucanne, S., Skonieczny, C., André, L., Bermell, S., Cheron, S., Dennielou, B., Etoubleau, J., Freslon, N., Gauchery, T., Germain, Y., Jorry, S.J., Ménot, G., Monin, L., Ponzevera, E., Rouget, M.L., Tachikawa, K., Barrat, J.A., 2015. Rare earth elements and neodymium isotopes in world river sediments revisited. Geochimica et Cosmochimica Acta 170, 17-38.

Bayon, G., Vigier, N., Burton, K.W., Jean Carignan, A.s.B., Etoubleau, J.l., Chu, N.-C., 2006. The control of weathering processes on riverine and seawater hafnium isotope ratios. Geology 34, 433-436.

Beaufort, L.d., de Garidel-Thoron, T., Linsley, B., Oppo, D., Buchet, N., 2003. Biomass burning and oceanic primary production estimates in the Sulu Sea area over the last 380 kyr and the East Asian monsoon dynamics. Marine Geology 201, 53-65.

Behrensmeyer, A.K., Quade, J., Cerling, T.E., Kappelman, J., Khan, I.A., Copeland, P., Roe, L., Hicks, J., Stubblefield, P., Willis, B.J., 2007. The structure and rate of late Miocene expansion of C4 plants: Evidence from lateral variation in stable isotopes in paleosols of the Siwalik Group, northern Pakistan. Geological Society of America Bulletin 119, 1486-1505.

Belshaw, N., Freedman, P., O'Nions, R., Frank, M., Guo, Y., 1998. A new variable dispersion double-focusing plasma mass spectrometer with performance illustrated for Pb isotopes. International Journal of Mass Spectrometry 181, 51-58.

Blichert-Toft, J., 2008. The Hf isotopic composition of zircon reference material 91500. Chemical Geology 253, 252-257.

Blichert-Toft, J., Albarède, F., 1997. The Lu-Hf isotope geochemistry of chondrites and the evolution of the mantle-crust system. Earth and Planetary Science Letters 148, 243-258.

Blum, J.D., Erel, Y., 1995. A silicate weathering mechanism linking increases in marine 87Sr/ 86Sr with global glaciation. Nature 373, 415-418.

Blum, J.D., Erel, Y., 2003. Radiogenic Isotopes in Weathering and Hydrology. Treatise on Geochemistry 5.

Blum, J.D., Erel, Y., Brown, K., 1993. 87Sr/86Sr ratios of Sierra Nevada stream waters: Implications for relative mineral weathering rates. Geochimica et Cosmochimica Acta 57, 5019-5025.

Bolton, C.T., Chang, L., Clemens, S.C., Kodama, K., Ikehara, M., Medina-Elizalde, M., Paterson, G.A., Roberts, A.P., Rohling, E.J., Yamamoto, Y., Zhao, X., 2013. A 500,000 year record

of Indian summer monsoon dynamics recorded by eastern equatorial Indian Ocean upper water-column structure. Quaternary Science Reviews 77, 167-180.

Bookhagen, B., Fleitmann, D., Nishiizumi, K., Strecker, M.R., Thiede, R.C., 2006. Holocene monsoonal dynamics and fluvial terrace formation in the northwest Himalaya, India. Geology 34, 601.

Bouquillon, A., France-Lanord, C., Michard, A., Tiercelin, J.-J., 1990. Sedimentology and isotopic chemistry of the Bengal Fan sediments: the denudation of the Himalaya. Proceedings of the Ocean Drilling Program, Scientific Results 116, 43-58.

Bouvier, A., Vervoort, J.D., Patchett, P.J., 2008. The Lu–Hf and Sm–Nd isotopic composition of CHUR: constraints from unequilibrated chondrites and implications for the bulk composition of terrestrial planets. Earth and Planetary Science Letters 273, 48-57.

Bretschneider, L., Hathorne, E.C., Huang, H., Lübbers, J., Kochhann, K.G.D., Holbourn, A., Kuhnt, W., Thiede, R.C., Gebregiorgis, D., Giosan, L., Frank, M., 2020. Provenance and weathering of clays in the Bay of Bengal during the Miocene: Linkages to tectonics and monsoonal climate. Submitted to Paleoceanography and Paleoclimatology.

Burbank, D.W., Blythe, A.E., Putkonen, J., Pratt-Sitaula, B., Gabet, E.J., Oskin, M., Barros, A., Ojha, T.P., 2003. Decoupling of erosion and precipitation in the Himalayas. Nature 426, 652-655.

Burchfiel, B.C., Zhiliang, C., Hodges, K.V., Yuping, L., Royden, L.H., Changrong, D., 1992. The South Tibetan detachment system, Himalayan orogen: Extension contemporaneous with and parallel to shortening in a collisional mountain belt. Geological Society of America.

Burton, K.W., Vance, D., 2000. Glacial–interglacial variations in the neodymium isotope composition of seawater in the Bay of Bengal recorded by planktonic foraminifera. Earth and Planetary Science Letters 176, 425-441.

Carrapa, B., Orme, D.A., DeCelles, P.G., Kapp, P., Cosca, M.A., Waldrip, R., 2014. Miocene burial and exhumation of the India-Asia collision zone in southern Tibet: Response to slab dynamics and erosion. Geology 42, 443-446.

Carter, S.C., Griffith, E.M., Clift, P.D., Scher, H.D., Dellapenna, T.M., 2020. Clay-fraction strontium and neodymium isotopes in the Indus Fan: implications for sediment transport and provenance. Geological Magazine 157, 879-894.

Catlos, E.J., Dubey, C.S., Harrison, T.M., Edwards, M.A., 2004. Late Miocene movement within the Himalayan Main Central Thrust shear zone, Sikkim, north-east India. Journal of Metamorphic Geology 22, 207-226.

Cerling, T.E., Harris, J.M., MacFadden, B.J., Leakey, M.G., Quade, J., Eisenmann, V., Ehleringer, J.R., 1997. Global vegetation change through the Miocene/Pliocene boundary. Nature 389, 153-158.

Chen, H., Xu, Z., Lim, D., Clift, P.D., Chang, F., Li, T., Cai, M., Wang, W., Yu, Z., Sun, R., 2020a. Geochemical records of the provenance and silicate weathering/erosion from the eastern Arabian Sea and their responses to the Indian summer monsoon since the Mid-Pleistocene. Paleoceanography and Paleoclimatology 35, e2019PA003732.

Chen, T.Y., Li, G., Frank, M., Ling, H.F., 2013. Hafnium isotope fractionation during continental weathering: Implications for the generation of the seawater Nd-Hf isotope relationships. Geophysical Research Letters 40, 916-920.

Chen, W.-H., Yan, Y., Clift, P.D., Carter, A., Huang, C.-Y., Pickering, K.T., Chemale Jr, F., Shan, Y., Zhang, X., 2020b. Drainage evolution and exhumation history of the eastern Himalaya: Insights from the Nicobar Fan, northeastern Indian Ocean. Earth and Planetary Science Letters 548, 116472.

Chu, N.-C., Taylor, R.N., Chavagnac, V.r., Nesbitt, R.W., Boella, R.M., Milton, J.A., German, C.R., Bayon, G., Burton, K., 2002. Hf isotope ratio analysis using multi-collector inductively coupled plasma mass spectrometry: an evaluation of isobaric interference corrections. Journal of Analytical Atomic Spectrometry 17, 1567-1574.

Clemens, S., Holbourn, A., Kubota, Y., Lee, K., Liu, Z., Chen, G., Nelson, A., Fox-Kemper, B., 2018. Precession-band variance missing from East Asian monsoon runoff. Nature communications 9, 1-12.

Clemens, S., Kuhnt, W., LeVay, L., Anand, P., Ando, T., Bartol, M., Bolton, C., Ding, X., Gariboldi, K., Giosan, L., 2016. Site U1443. Indian Monsoon Rainfall, Proceedings of the international ocean discovery program, 1-41.

Clemens, S.C., Prell, W.L., 1990. Late Pleistocene variability of Arabian Sea summer monsoon winds and continental aridity: Eolian records from the lithogenic component of deep-sea sediments. Paleoceanography 5, 109-145.

Clemens, S.C., Prell, W.L., 2007. The timing of orbital-scale Indian monsoon changes. Quaternary Science Reviews 26, 275-278.

Clift, P.D., Hodges, K.V., Heslop, D., Hannigan, R., Van Long, H., Calves, G., 2008. Correlation of Himalayan exhumation rates and Asian monsoon intensity. Nature Geoscience 1, 875-880.

Clift, P.D., Lee, J.I., Hildebrand, P., Shimizu, N., Layne, G.D., Blusztajn, J., Blum, J.D., Garzanti, E., Khan, A.A., 2002. Nd and Pb isotope variability in the Indus River System: implications for sediment provenance and crustal heterogeneity in the Western Himalaya. Earth and Planetary Science Letters 200, 91-106.

Clift, P.D., Wan, S., Blusztajn, J., 2014. Reconstructing chemical weathering, physical erosion and monsoon intensity since 25Ma in the northern South China Sea: A review of competing proxies. Earth-Science Reviews 130, 86-102.

Clift, P.D., Webb, A.A.G., 2018. A history of the Asian monsoon and its interactions with solid Earth tectonics in Cenozoic South Asia. Geological Society, London, Special Publications 483, 631-652.

Cohen, A.S., O'Nions, R.K., Siegenthaler, R., Griffin, W.L., 1988. Chronology of the pressure-temperature history recorded by a granulite terrain. Contributions to Mineralogy and Petrology 98, 303–311.

Colin, C., Turpin, L., Bertaux, J., Desprairies, A., Kissel, C., 1999. Erosional history of the Himalayan and Burman ranges during the last two glacial-interglacial cycles. Earth and Planetary Science Letters 171, 647-660.

Colin, C., Turpin, L., Blamart, D., Frank, N., Kissel, C., Duchamp, S., 2006. Evolution of weathering patterns in the Indo-Burman Ranges over the last 280 kyr: Effects of sediment provenance on87Sr/86Sr ratios tracer. Geochemistry, Geophysics, Geosystems 7, n/a-n/a.

Colleps, C.L., McKenzie, N.R., Stockli, D.F., Hughes, N.C., Singh, B.P., Webb, A.A.G., Myrow, P.M., Planavsky, N.J., Horton, B.K., 2018. Zircon (U-Th)/He Thermochronometric Constraints on Himalayan Thrust Belt Exhumation, Bedrock Weathering, and Cenozoic Seawater Chemistry. Geochemistry, Geophysics, Geosystems 19, 257-271.

Colleps, C.L., Stockli, D.F., McKenzie, N.R., Webb, A.A.G., Horton, B.K., 2019. Neogene Kinematic Evolution and Exhumation ofthe NW India Himalaya: Zircon Geo- and Thermochronometric Insights From the Fold-Thrust Belt and Foreland Basin. Tectonics 38.

Curray, J.R., Emmel, F.J., Moore, D.G., 2003. The Bengal Fan: morphology, geometry, stratigraphy, history and processes. Marine and Petroleum Geology 19, 1191-1223.

Damodararao, K., Singh, S.K., Rai, V.K., Ramaswamy, V., Rao, P.S., 2016. Lithology, Monsoon and Sea-Surface Current Control on Provenance, Dispersal and Deposition of Sediments over the Andaman Continental Shelf. Frontiers in Marine Science 3.

Dausmann, V., Gutjahr, M., Frank, M., Kouzmanov, K., Schaltegger, U., 2019. Experimental evidence for mineral-controlled release of radiogenic Nd, Hf and Pb isotopes from granitic rocks during progressive chemical weathering. Chemical Geology.

Dellinger, M., Gaillardet, J., Bouchez, J., Calmels, D., Galy, V., Hilton, R.G., Louvat, P., France-Lanord, C., 2014. Lithium isotopes in large rivers reveal the cannibalistic nature of modern continental weathering and erosion. Earth and Planetary Science Letters 401, 359-372.

Deng, T., Wang, X., Wu, F., Wang, Y., Li, Q., Wang, S., Hou, S., 2019. Review: Implications of vertebrate fossils for paleo-elevations of the Tibetan Plateau. Global and Planetary Change 174, 58-69.

DePaolo, D., Wasserburg, G., 1976. Nd isotopic variations and petrogenetic models. Geophysical Research Letters 3, 249-252.

Derry, L.A., France-Lanord, C., 1996. Neogene Himalayan weathering history and river 87Sr, 86Sr: impact on the marine Sr record. Earth and Planetary Science Letters 142, 59-74.

Diester-Haass, L., Billups, K., Emeis, K.C., 2006. Late Miocene carbon isotope records and marine biological productivity: Was there a (dusty) link? Paleoceanography 21.

Ding, L., Spicer, R., Yang, J., Xu, Q., Cai, F., Li, S., Lai, Q., Wang, H., Spicer, T., Yue, Y., 2017. Quantifying the rise of the Himalaya orogen and implications for the South Asian monsoon. Geology 45, 215-218.

Douglas, G.B., Gray, C.M., Hart, B.T., Beckett, R., 1995. A strontium isotopic investigation of the origin of suspended particulate matter (SPM) in the Murray-Darling River system, Australia. Geochimica et Cosmochimica Acta 59, 3799-3815.

Edmond, J., 1992. Himalayan tectonics, weathering processes, and the strontium isotope record in marine limestones. Science 258, 1594-1597.

Eisenhauer, A., Meyer, H., Rachold, V., Hansen, B.T., Spielhagen, R.F., Tütken, T., Lindemann, F., Wiegand, B., Kassens, H., 1999. Grain size separation and sediment mixing in Arctic

Ocean sediments: evidence from the strontium isotope systematic. Chemical Geology 158, 173–188.

Erel, Y., Harlavan, Y., Blum, J.D., 1994. Lead isotope systematics of granitoid weathering. Geochimica et Cosmochimica Acta 58, 5299-5306.

Farrell, J.W., Clemens, S.C., Gromet, L.P., 1995. Improved chronostratigraphic reference curve of late Neogene seawater 87Sr/86Sr. Geology 23, 403–406.

Fontanier, C., Mamo, B., Toucanne, S., Bayon, G., Schmidt, S., Deflandre, B., Dennielou, B., Jouet, G., Garnier, E., Sakai, S., Lamas, R.M., Duros, P., Toyofuku, T., Salé, A., Belleney, D., Bichon, S., Boissier, A., Chéron, S., Pitel, M., Roubi, A., Rovere, M., Grémare, A., Dupré, S., Jorry, S.J., 2018. Are deep-sea ecosystems surrounding Madagascar threatened by land-use or climate change? Deep Sea Research Part I: Oceanographic Research Papers 131, 93-100.

Foster, G.L., Lear, C.H., Rae, J.W.B., 2012. The evolution of pCO2, ice volume and climate during the middle Miocene. Earth and Planetary Science Letters 341-344, 243-254.

France-Lanord, C., Derry, L., Michard, A., 1993. Evolution of the Himalaya since Miocene time: isotopic and sedimentological evidence from the Bengal Fan. Geological Society, London, Special Publications 74, 603-621.

France-Lanord, C., Derry, L.A., 1997. Organic carbon burial forcing of the carbon cycle from Himalayan erosion. Nature 390, 65-67.

France-Lanord, C., Le Fort, P., 1988. Crustal melting and granite genesis during the Himalayan collision orogenesis. Transactions of the Royal Society of Edinburgh: Earth Sciences 79, 183-195.

Frank, M., 2002. Radiogenic isotopes: Tracers of past ocean circulation and erosional input. Reviews of Geophysics 40.

Galer, S.J.G., O'Nions, R.K., 1989. Chemical and Isotopic Studies of Ultramafic Inclusions from the San Carlos Volcanic Field, Arizona: A Bearing on their Petrogenesis. Journal of Petrology 30, 1033-1064.

Galy, A., France-Lanord, C., 2001. Higher erosion rates in the Himalaya: Geochemical constraints on riverine fluxes. Geology 29, 23.

Galy, A., France-Lanord, C., Derry, L.A., 1996. The Late Oligocene-Early Miocene Himalayan belt

Constraints deduced from isotopic compositions of Early Miocene turbidites in the Bengal Fan. Tectonophysics 260, 109-118.

Galy, V., France-Lanord, C., Beyssac, O., Faure, P., Kudrass, H., Palhol, F., 2007. Efficient organic carbon burial in the Bengal fan sustained by the Himalayan erosional system. Nature 450, 407-410.

Galy, V., France-Lanord, C., Peucker-Ehrenbrink, B., Huyghe, P., 2010. Sr–Nd–Os evidence for a stable erosion regime in the Himalaya during the past 12 Myr. Earth and Planetary Science Letters 290, 474-480.

Galy, V., François, L., France-Lanord, C., Faure, P., Kudrass, H., Palhol, F., Singh, S.K., 2008. C4 plants decline in the Himalayan basin since the Last Glacial Maximum. Quaternary Science Reviews 27, 1396-1409.

Gansser, A., 1964. Geology of the Himalayas. Interscience, London.

Garçon, M., Chauvel, C., France-Lanord, C., Huyghe, P., Lavé, J., 2013. Continental sedimentary processes decouple Nd and Hf isotopes. Geochimica et Cosmochimica Acta 121, 177-195.

Garçon, M., Chauvel, C., France-Lanord, C., Limonta, M., Garzanti, E., 2014. Which minerals control the Nd–Hf–Sr–Pb isotopic compositions of river sediments? Chemical Geology 364, 42-55.

Gasparon, M., Varne, R., 1995. Sumatran granitoids and their relationship to Southeast Asian terranes. Tectonophysics 251, 277-299.

Gebregiorgis, D., Hathorne, E.C., Giosan, L., Clemens, S., Nürnberg, D., Frank, M., 2018. Southern Hemisphere forcing of South Asian monsoon precipitation over the past ~1 million years. Nature Communications 9.

Giosan, L., Naing, T., Min Tun, M., Clift, P.D., Filip, F., Constantinescu, S., Khonde, N., Blusztajn, J., Buylaert, J.-P., Stevens, T., Thwin, S., 2018. On the Holocene evolution of the Ayeyawady megadelta. Earth Surface Dynamics 6, 451-466.

Goldstein, S.L., Jacobsen, S.B., 1987. The Nd and Sr isotopic systematics of river-water dissolved material: Implications for the sources of Nd and Sr in seawater. Chemical Geology 66, 245-272.

Gourlan, A.T., Meynadier, L., Allègre, C.J., Tapponnier, P., Birck, J.-L., Joron, J.-L., 2010. Northern Hemisphere climate control of the Bengali rivers discharge during the past 4 Ma. Quaternary Science Reviews 29, 2484-2498.

Gupta, A.K., Yuvaraja, A., Prakasam, M., Clemens, S.C., Velu, A., 2015. Evolution of the South Asian monsoon wind system since the late Middle Miocene. Palaeogeography, palaeoclimatology, palaeoecology 438, 160-167.

Gutjahr, M., Frank, M., Lippold, J., Halliday, A.N., 2014. Peak Last Glacial weathering intensity on the North American continent recorded by the authigenic Hf isotope composition of North Atlantic deep-sea sediments. Quaternary Science Reviews 99, 97-111.

Gutjahr, M., Frank, M., Stirling, C.H., Klemm, V., van de Flierdt, T., Halliday, A.N., 2007. Reliable extraction of a deepwater trace metal isotope signal from Fe–Mn oxyhydroxide coatings of marine sediments. Chemical Geology 242, 351-370.

Hahn, D.G., Manabe, S., 1975. The role of mountains in the south Asian monsoon circulation. Journal of the Atmospheric Sciences 32, 1515-1541.

Hall, R., 2012. Late Jurassic–Cenozoic reconstructions of the Indonesian region and the Indian Ocean. Tectonophysics 570, 1-41.

Halley, E., 1686. An historical account of the trade winds, and monsoons, observable in the seas between and near the Tropicks, with an attempt to assign the physical cause of the said winds. Philosophical Transactions of the Royal Society of London 16, 153-168.

Harlavan, Y., Erel, Y., 2002. The release of Pb and REE from granitoids by the dissolution of accessory phases. Geochimica et Cosmochimica Acta 66, 837–848.

Harrison, T.M., Copeland, P., Kidd, W.S.F., Yin, A., 1992. Raising Tibet. Science 255, 1663-1670.

Hein, C.J., Galy, V., Galy, A., France-Lanord, C., Kudrass, H., Schwenk, T., 2017. Post-glacial climate forcing of surface processes in the Ganges–Brahmaputra river basin and implications for carbon sequestration. Earth and Planetary Science Letters 478, 89-101.

Henrot, A.J., Utescher, T., Erdei, B., Dury, M., Hamon, N., Ramstein, G., Krapp, M., Herold, N., Goldner, A., Favre, E., Munhoven, G., François, L., 2017. Middle Miocene climate and vegetation models and their validation with proxy data. Palaeogeography, Palaeoclimatology, Palaeoecology 467, 95-119.

Herbert, T.D., Lawrence, K.T., Tzanova, A., Peterson, L.C., Caballero-Gill, R., Kelly, C.S., 2016. Late Miocene global cooling and the rise of modern ecosystems. Nature Geoscience 9, 843-847.

Hindshaw, R., Aciego, S., Piotrowski, A., Tipper, E., 2018. Decoupling of dissolved and bedrock neodymium isotopes during sedimentary cycling. Geochemical Perspectives Letters 8, 43-46.

Hodell, D.A., Mueller, P.A., McKenzie, J.A., Mead, G.A., 1989. Strontium isotope stratigraphy and geochemistry of the late Neogene ocean. Earth and Planetary Science Letters 92, 165-178.

Hodges, K., Bowring, S., Davidek, K., Hawkins, D., Krol, M., 1998. Evidence for rapid displacement on Himalayan normal faults and the importance of tectonic denudation in the evolution of mountain ranges. Geology 26, 483.

Hodges, K.V., 2000. Tectonics of the Himalaya and southern Tibet from two perspectives. GSA Bulletin 112, 324-350.

Holbourn, A., Kuhnt, W., Clemens, S., Prell, W., Andersen, N., 2013. Middle to late Miocene stepwise climate cooling: Evidence from a high-resolution deep water isotope curve spanning 8 million years. Paleoceanography 28, 688-699.

Holbourn, A., Kuhnt, W., Regenberg, M., Schulz, M., Mix, A., Andersen, N., 2010. Does Antarctic glaciation force migration of the tropical rain belt? Geology 38, 783-786.

Holbourn, A., Kuhnt, W., Schulz, M., Erlenkeuser, H., 2005. Impacts of orbital forcing and atmospheric carbon dioxide on Miocene ice-sheet expansion. Nature 438, 483-487.

Holbourn, A.E., Kuhnt, W., Clemens, S.C., Kochhann, K.G.D., Johnck, J., Lubbers, J., Andersen, N., 2018. Late Miocene climate cooling and intensification of southeast Asian winter monsoon. Nat Commun 9, 1584.

Horwitz, E.P., Chiarizia, R., Dietz, M.L., 1992. A novel strontium-selective extraction chromatographic resin. Solvent extraction and ion exchange 10, 313-336.

Hovan, S.A., Rea, D.K., 1992. The Cenozoic record of continental mineral deposition on broken and ninetyeast ridges, Indian Ocean: Southern African aridity and sediment delivery from the Himalayas. Paleoceanography 7, 833-860.

Huang, Y., Clemens, S.C., Liu, W., Wang, Y., Prell, W.L., 2007. Large-scale hydrological change drove the late Miocene C4 plant expansion in the Himalayan foreland and Arabian Peninsula. Geology 35, 531.

Huber, M., Goldner, A., 2012. Eocene monsoons. Journal of Asian Earth Sciences 44, 3-23.

Jacobsen, S.B., Wasserburg, G.J., 1980. Sm-Nd Isotopic Evolution of Chondrites Earth and Planetary Science Letters 50, 139-155.

Jochum, K.P., Nohl, U., Herwig, K., Lammel, E., Stoll, B., Hofmann, A.W., 2005. GeoReM: a new geochemical database for reference materials and isotopic standards. Geostandards and Geoanalytical Research 29, 333-338.

Jochum, K.P., Weis, U., Schwager, B., Stoll, B., Wilson, S.A., Haug, G.H., Andreae, M.O., Enzweiler, J., 2016. Reference Values Following ISO Guidelines for Frequently Requested Rock Reference Materials. Geostandards and Geoanalytical Research 40, 333-350.

John, C.M., Karner, G.D., Mutti, M., 2004. δ18O and Marion Plateau backstripping: combining two approaches to constrain late middle Miocene eustatic amplitude. Geology 32, 829-832.

Jöhnck, J., Kuhnt, W., Holbourn, A., Andersen, N., 2020. Variability of the Indian Monsoon in the Andaman Sea across the Miocene-Pliocene transition. Paleoceanography and Paleoclimatology, e2020PA003923.

Joussain, R., Colin, C., Liu, Z., Meynadier, L., Fournier, L., Fauquembergue, K., Zaragosi, S., Schmidt, F., Rojas, V., Bassinot, F., 2016. Climatic control of sediment transport from the Himalayas to the proximal NE Bengal Fan during the last glacial-interglacial cycle. Quaternary Science Reviews 148, 1-16.

Kellett, D.A., Grujic, D., Erdmann, S., 2009. Miocene structural reorganization of the South Tibetan detachment, eastern Himalaya: Implications for continental collision. Lithosphere 1, 259-281.

Kessarkar, P.M., Rao, V.P., Ahmad, S., Patil, S., Kumar, A.A., Babu, G.A., Chakraborty, S., Rajan, R.S., 2005. Changing sedimentary environment during the Late Quaternary: Sedimentological and isotopic evidence from the distal Bengal Fan. Deep Sea Research Part I: Oceanographic Research Papers 52, 1591-1615.

Kominz, M.A., Browning, J.V., Miller, K.G., Sugarman, P.J., Mizintseva, S., Scotese, C.R., 2008. Late Cretaceous to Miocene sea-level estimates from the New Jersey and Delaware coastal plain coreholes: an error analysis. Basin Research 20, 211-226.

Kroon, D., Steens, T., Troelstra, S., R., 1991. Onset of monsoonal related upwelling in the western Arabian Sea as revealed by planktonic foraminifers. Proceedings of the Ocean Drilling Program, Scientific Results 117, 257-263.

Krumm, S., 2006. SediCalc (free geological software). GeoZentrum Nordbayern, Universität Erlangen-Nürnberg http://www. geol. uni-erlangen. de/sedicalc.

Kuhnt, W., Holbourn, A.E., Jöhnck, J., Lübbers, J., 2020. Miocene to Pleistocene Palaeoceanography of the Andaman Region: Evolution of the Indian Monsoon on a Warmer-Than-Present Earth, The Andaman Islands and Adjoining Offshore: Geology, Tectonics and Palaeoclimate. Springer, pp. 261-288.

Kumar, V.S., Pathak, K., Pednekar, P., Raju, N., Gowthaman, R., 2006. Coastal processes along the Indian coastline. Current science, 530-536.

Kutzbach, J., Guetter, P.J., Ruddiman, W.F., Prell, W., 1989. Sensitivity of Climate to Late Cenozoic Uplift in Southern Asia and the American West: Numerical Experiments. Journal of Geophysical Research 94, 393-407.

Lee, J., Kim, S., Lee, J.I., Cho, H.G., Phillips, S.C., Khim, B.-K., 2019. Monsoon-influenced variation of clay mineral compositions and detrital Nd-Sr isotopes in the western Andaman Sea (IODP Site U1447) since the late Miocene. Palaeogeography, Palaeoclimatology, Palaeoecology, 109339.

LeFort, P., 1975. Himalayas-collided range-present knowledge of continental arc. American Journal of Science.

Li, J., Fang, X., Song, C., Pan, B., Ma, Y., Yan, M., 2014. Late Miocene–Quaternary rapid stepwise uplift of the NE Tibetan Plateau and its effects on climatic and environmental changes. Quaternary Research 81, 400-423.

Li, J., Liu, S., Shi, X., Zhang, H., Fang, X., Chen, M.-T., Cao, P., Sun, X., Ye, W., Wu, K., Khokiattiwong, S., Kornkanitnan, N., 2018. Clay minerals and Sr-Nd isotopic composition of the Bay of Bengal sediments: Implications for sediment provenance and climate control since 40 ka. Quaternary International 493, 50-58.

Licht, A., van Cappelle, M., Abels, H.A., Ladant, J.B., Trabucho-Alexandre, J., France-Lanord, C., Donnadieu, Y., Vandenberghe, J., Rigaudier, T., Lecuyer, C., Terry, D., Jr., Adriaens, R., Boura, A., Guo, Z., Soe, A.N., Quade, J., Dupont-Nivet, G., Jaeger, J.J., 2014. Asian monsoons in a late Eocene greenhouse world. Nature 513, 501-506.

Lightfoot, P., Hawkesworth, C., Devey, C.W., Rogers, N., CALSTEREN, P.V., 1990. Source and differentiation of Deccan Trap lavas: implications of geochemical and mineral chemical variations. Journal of Petrology 31, 1165-1200.

Lübbers, J., Kuhnt, W., Holbourn, A.E., Bolton, C.T., Gray, E., Usui, Y., Kochhann, K.G.D., Beil, S., Andersen, N., 2019. The Middle to Late Miocene "Carbonate Crash" in the Equatorial Indian Ocean. Paleoceanography and Paleoclimatology.

Lugmair, G., Marti, K., 1978. Lunar initial 143Nd/144Nd: differential evolution of the lunar crust and mantle. Earth and Planetary Science Letters 39, 349-357.

Mahoney, J., Macdougall, J., Lugmair, G., Murali, A., Das, M.S., Gopalan, K., 1982. Origin of the Deccan Trap flows at Mahabaleshwar inferred from Nd and Sr isotopic and chemical evidence. Earth and Planetary Science Letters 60, 47-60.

Marchandise, S., Robin, E., Ayrault, S., Roy-Barman, M., 2014. U–Th–REE–Hf bearing phases in Mediterranean Sea sediments: Implications for isotope systematics in the ocean. Geochimica et Cosmochimica Acta 131, 47-61.

McNeill, L.C., Dugan, B., Backman, J., Pickering, K.T., Pouderoux, H.F.A., Henstock, T.J., Petronotis, K.E., Carter, A., Chemale, F., Milliken, K.L., Kutterolf, S., Mukoyoshi, H., Chen, W., Kachovich, S., Mitchison, F.L., Bourlange, S., Colson, T.A., Frederik, M.C.G., Guèrin, G., Hamahashi, M., House, B.M., Hüpers, A., Jeppson, T.N., Kenigsberg, A.R., Kuranaga, M., Nair, N., Owari, S., Shan, Y., Song, I., Torres, M.E., Vannucchi, P., Vrolijk, P.J., Yang, T., Zhao, X., Thomas, E., 2017. Understanding Himalayan erosion and the significance of the Nicobar Fan. Earth and Planetary Science Letters 475, 134-142.

Miao, Y., Herrmann, M., Wu, F., Yan, X., Yang, S., 2012. What controlled Mid–Late Miocene long-term aridification in Central Asia? — Global cooling or Tibetan Plateau uplift: A review. Earth-Science Reviews 112, 155-172.

Miller, K.G., Browning, J.V., Schmelz, W.J., Kopp, R.E., Mountain, G.S., Wright, J.D., 2020. Cenozoic sea-level and cryospheric evolution from deep-sea geochemical and continental margin records. Science advances 6, eaaz1346.

Miller, K.G., Kominz, M.A., Browning, J.V., Wright, J.D., Mountain, G.S., Katz, M.E., Sugarman, P.J., Cramer, B.S., Christie-Blick, N., Pekar, S.F., 2005. The Phanerozoic Record of Global Sea-Level Change. Science 310, 1293-1298.

Milliman, J.D., Syvitski, J.P., 1992. Geomorphic/tectonic control of sediment discharge to the ocean: the importance of small mountainous rivers. The Journal of Geology 100, 525-544.

Millot, R., Allègre, C.-J., Gaillardet, J., Roy, S., 2004. Lead isotopic systematics of major river sediments: a new estimate of the Pb isotopic composition of the Upper Continental Crust. Chemical Geology 203, 75-90.

Molnar, P., 2005. Mio-Pliocene Growth of the Tibetan Plateau and Evolution of East Asian Climate. Palaeontologia Electronica 8.

Molnar, P., England, P., Martinod, J., 1993. Mantle dynamics, uplift of the Tibetan Plateau, and the Indian Monsoon. Reviews of Geophysics 31, 357.

Molnar, P., Tapponnier, P., 1978. Active tectonics of Tibet. Journal of Geophysical Research 83, 5361.

Münker, C., Weyer, S., Scherer, E., Mezger, K., 2001. Separation of high field strength elements (Nb, Ta, Zr, Hf) and Lu from rock samples for MC-ICPMS measurements. Geochemistry, Geophysics, Geosystems 2.

Najman, Y., Bickle, M., Garzanti, E., Pringle, M., Barfod, D., Brozovic, N., Burbank, D., Ando, S., 2009. Reconstructing the exhumation history of the Lesser Himalaya, NW India, from a multitechnique provenance study of the foreland basin Siwalik Group. Tectonics 28, n/a-n/a.

Najman, Y., Sobel, E.R., Millar, I., Stockli, D.F., Govin, G., Lisker, F., Garzanti, E., Limonta, M., Vezzoli, G., Copley, A., Zhang, P., Szymanski, E., Kahn, A., 2020. The exhumation of the Indo-Burman Ranges, Myanmar. Earth and Planetary Science Letters 530, 115948.

Nir-El, Y., Lavi, N., 1998. Measurement of the half-life of 176Lu. Applied Radiation and Isotopes 49, 1653-1655.

Oliver, L., Harris, N., Bickle, M., Chapman, H., Dise, N., Horstwood, M., 2003. Silicate weathering rates decoupled from the 87Sr/86Sr ratio of the dissolved load during Himalayan erosion. Chemical Geology 201, 119-139.

Patchett, P., White, W., Feldmann, H., Kielinczuk, S., Hofmann, A., 1984. Hafnium/rare earth element fractionation in the sedimentary system and crustal recycling into the Earth's mantle. Earth and Planetary Science Letters 69, 365-378.

Peucat, J., Vidal, P., Bernard-Griffiths, J., Condie, K., 1989. Sr, Nd, and Pb isotopic systematics in the Archean low-to high-grade transition zone of southern India: syn-accretion vs. post-accretion granulites. The Journal of Geology 97, 537-549.

Pickering, K.T., Carter, A., Andò, S., Garzanti, E., Limonta, M., Vezzoli, G., Milliken, K.L., 2020. Deciphering relationships between the Nicobar and Bengal submarine fans, Indian Ocean. Earth and Planetary Science Letters 544, 116329.

Pin, C., Zalduegui, J.F.S., 1997. Sequential separation of light rare-earth elements, thorium and uranium by miniaturized extraction chromatography: Application to isotopic analyses of silicate rocks. Analytica Chimica Acta 339, 79-89.

Piotrowski, A.M., Lee, D.-C., Christensen, J.N., Burton, K.W., Halliday, A.N., Hein, J.R., Günther, D., 2000. Changes in erosion and ocean circulation recorded in the Hf isotopic compositions of North Atlantic and Indian Ocean ferromanganese crusts. Earth and Planetary Science Letters 181, 315-325.

Pisias, N., Mix, A., 1988. Aliasing of the geologic record and the search for long-period Milankovitch cycles. Paleoceanography 3, 613-619.

Prell, W.L., Kutzbach, J.E., 1992. Sensitivity of the Indian monsoon to forcing parameters and implications for its evolution. Nature 360, 647-652.

Quade, J., Cerling, T.E., Bowman, J.R., 1989. Development of Asian monsoon revealed by marked ecological shift during the latest Miocene in northern Pakistan. Nature 342, 163-166.

Rao, P.S., Ramaswamy, V., Thwin, S., 2005. Sediment texture, distribution and transport on the Ayeyarwady continental shelf, Andaman Sea. Marine Geology 216, 239-247.

Raymo, M.E., 1994. The Himalayas, organic carbon burial, and climate in the Miocene. Paleoceanography 9, 399-404.

Raymo, M.E., Ruddiman, W.F., 1992. Tectonic forcing of late Cenozoic climate. Nature 359, 117-122.

Retallack, G.J., 2001. Cenozoic expansion of grasslands and climatic cooling. The Journal of Geology 109, 407-426.

Richter, F.M., Rowley, D.B., DePaolo, D.J., 1992. Sr isotope evolution of seawater: the role of tectonics. Earth and Planetary Science Letters 109, 11-23.

Robinson, R.A.J., Bird, M., Oo, N.W., Hoey, T., Aye, M.M., Higgitt, D., Swe, A., Tun, T., Win, S.L., 2007. The Irrawaddy river sediment flux to the Indian Ocean: the original nineteenth-century data revisited. The Journal of Geology 115, 629-640.

Ruddiman, W.F., 2006. What is the timing of orbital-scale monsoon changes? Quaternary Science Reviews 25, 657-658.

Ruddiman, W.F., Kutzbach, J.E., 1989. Forcing of late Cenozoic northern hemisphere climate by plateau uplift in southern Asia and the American West. Journal of Geophysical Research: Atmospheres 94, 18409-18427.

Sahoo, Y.V., Nakai, S.i., Ali, A., 2006. Modified ion exchange separation for tungsten isotopic measurements from kimberlite samples using multi-collector inductively coupled plasma mass spectrometry. Analyst 131, 434-439.

Scherer, E., Münker, C., Mezger, K., 2001. Calibration of the lutetium-hafnium clock. Science 293, 683-687.

Schulz, M., Mudelsee, M., 2002. REDFIT: estimating red-noise spectra directly from unevenly spaced paleoclimatic time series. Computers & Geosciences 28, 421-426.

Searle, M.P., Law, R.D., Godin, L., Larson, K.P., Streule, M.J., Cottle, J.M., Jessup, M.J., 2008. Defining the Himalayan Main Central Thrust in Nepal. Journal of the Geological Society 165, 523-534.

Singh, M., Singh, I.B., Müller, G., 2007. Sediment characteristics and transportation dynamics of the Ganga River. Geomorphology 86, 144-175.

Singh, S., Parkash, B., Awasthi, A., Kumar, S., 2011. Late Miocene record of palaeovegetation from Siwalik palaeosols of the Ramnagar sub-basin, India. Current Science, 213-222.

Singh, S.K., France-Lanord, C., 2002. Tracing the distribution of erosion in the Brahmaputra watershed from isotopic compositions of stream sediments. Earth and Planetary Science Letters 202, 645-662.

Srinivas, B., Sarin, M.M., 2013. Atmospheric dry-deposition of mineral dust and anthropogenic trace metals to the Bay of Bengal. Journal of Marine Systems 126, 56-68.

Steiger, R.H., Jäger, E., 1977. Subcommission on Geochronology: Convention on the use of decay constants in geo- and cosmochronology. Earth and Planetary Science Letters 36, 359-362.

Steinke, S., Groeneveld, J., Johnstone, H., Rendle-Bühring, R., 2010. East Asian summer monsoon weakening after 7.5Ma: Evidence from combined planktonic foraminifera Mg/Ca and δ18O (ODP Site 1146; northern South China Sea). Palaeogeography, Palaeoclimatology, Palaeoecology 289, 33-43.

Steinke, S., Hanebuth, T.J., Vogt, C., Stattegger, K., 2008. Sea level induced variations in clay mineral composition in the southwestern South China Sea over the past 17,000 yr. Marine Geology 250, 199-210.

Stoll, H.M., Vance, D., Arevalos, A., 2007. Records of the Nd isotope composition of seawater from the Bay of Bengal: Implications for the impact of Northern Hemisphere cooling on ITCZ movement. Earth and Planetary Science Letters 255, 213-228.

Sun, Y., An, Z., Clemens, S.C., Bloemendal, J., Vandenberghe, J., 2010. Seven million years of wind and precipitation variability on the Chinese Loess Plateau. Earth and Planetary Science Letters 297, 525-535.

Tanaka, T., Togashi, S., Kamioka, H., Amakawa, H., Kagami, H., Hamamoto, T., Masaki Yuhara, M., Orihashi, Y., Yoneda, S., Shimizu, H., Kunimaru, T., Takahashi, K., Yanagi, T., Nakano, T., Fujimaki, H., Shinjo, R., Asahara, Y., Tanimizu, M., Dragusanu, C., 2000. JNdi-1: a neodymium isotopic reference in consistency with LaJolla neodymium. Chemical Geology 168, 279-281.

Thiede, R.C., Bookhagen, B., Arrowsmith, J.R., Sobel, E.R., Strecker, M.R., 2004. Climatic control on rapid exhumation along the Southern Himalayan Front. Earth and Planetary Science Letters 222, 791-806.

Thiede, R.C., Ehlers, T.A., Bookhagen, B., Strecker, M.R., 2009. Erosional variability along the northwest Himalaya. Journal of Geophysical Research: Earth Surface 114.

Tremblay, M.M., Fox, M., Schmidt, J.L., Tripathy-Lang, A., Wielicki, M.M., Harrison, T.M., Zeitler, P.K., Shuster, D.L., 2015. Erosion in southern Tibet shut down at ~10 Ma due to enhanced rock uplift within the Himalaya. PNAS 112, 12030–12035.

Tripathi, S., Tiwari, M., Lee, J., Khim, B.-K., Expedition, I., Pandey, D.K., Clift, P.D., Kulhanek, D.K., Andò, S., Bendle, J.A., 2017. First evidence of denitrification vis-à-vis monsoon in the Arabian Sea since Late Miocene. Scientific reports 7, 43056.

Tripathy, G.R., Singh, S.K., Bhushan, R., Ramaswamy, V., 2011. Sr-Nd isotope composition of the Bay of Bengal sediments: Impact of climate on erosion in the Himalaya. Geochemical Journal 45, 175-186.

Turner, A.G., Annamalai, H., 2012. Climate change and the South Asian summer monsoon. Nature Climate Change 2, 587-595.

Tütken, T., Eisenhauer, A., Wiegand, B., Hansen, B.T., 2002. Glacial-interglacial cycles in Sr and Nd isotopic composition of Arctic marine sediments triggered by the Svalbard/Barents Sea ice sheet. Marine Geology 182, 351-372.

van de Flierdt, T., Frank, M., Lee, D.-C., Halliday, A.N., 2002. Glacial weathering and the hafnium isotope composition of seawater. Earth and Planetary Science Letters 201, 639-647.

Van de Flierdt, T., Goldstein, S.L., Hemming, S.R., Roy, M., Frank, M., Halliday, A.N., 2007. Global neodymium–hafnium isotope systematics—revisited. Earth and Planetary Science Letters 259, 432-441.

Vance, D., Thirlwall, M., 2002. An assessment of mass discrimination in MC-ICPMS using Nd isotopes. Chemical Geology 185, 227-240.

Vannay, J.-C., Grasemann, B., Rahn, M., Frank, W., Carter, A., Baudraz, V., Cosca, M., 2004. Miocene to Holocene exhumation of metamorphic crustal wedges in the NW Himalaya: Evidence for tectonic extrusion coupled to fluvial erosion. Tectonics 23, n/a-n/a.

Vervoort, J.D., Patchett, P.J., Blichert-Toft, J., Albarède, F., 1999. Relationships between Lu–Hf and Sm–Nd isotopic systems in the global sedimentary system. Earth and Planetary Science Letters 168, 79-99.

von Blanckenburg, F., Nägler, T.F., 2001. Weathering versus circulation-controlled changes in radiogenic isotope tracer composition of the Labrador Sea and North Atlantic Deep Water. Paleoceanography 16, 424-434.

Wang, C., Dai, J., Zhao, X., Li, Y., Graham, S.A., He, D., Ran, B., Meng, J., 2014. Outward-growth of the Tibetan Plateau during the Cenozoic: A review. Tectonophysics 621, 1-43.

Wang, P., Clemens, S., Beaufort, L., Braconnot, P., Ganssen, G., Jian, Z., Kershaw, P., Sarnthein, M., 2005. Evolution and variability of the Asian monsoon system: state of the art and outstanding issues. Quaternary Science Reviews 24, 595-629.

Wang, P.X., Wang, B., Cheng, H., Fasullo, J., Guo, Z., Kiefer, T., Liu, Z., 2017. The global monsoon across time scales: Mechanisms and outstanding issues. Earth-Science Reviews 174, 84-121.

White, N.M., Pringle, M., Garzanti, E., Bickle, M.J., Najman, Y., Chapman, H.J., Friend, P., 2002. Constraints on the exhumation and erosion of the High Himalayan Slab, NW India, from foreland basin deposits. Earth and Planetary Science Letters 195, 29-44.

White, W.M., Albarède, F., Télouk, P., 2000. High-precision analysis of Pb isotope ratios by multi-collector ICP-MS. Chemical Geology 167, 257-270.

White, W.M., Patchett, J., BenOthman, D., 1986. Hf isotope ratios of marine sediments and Mn nodules: evidence for a mantle source of Hf in seawater. Earth and Planetary Science Letters 79, 46-54.

Wilson, D.J., Galy, A., Piotrowski, A.M., Banakar, V.K., 2015. Quaternary climate modulation of Pb isotopes in the deep Indian Ocean linked to the Himalayan chemical weathering. Earth and Planetary Science Letters 424, 256-268.

Yin, A., 2006. Cenozoic tectonic evolution of the Himalayan orogen as constrained by along-strike variation of structural geometry, exhumation history, and foreland sedimentation. Earth-Science Reviews 76, 1-131.

You, Y., Huber, M., Müller, R.D., Poulsen, C.J., Ribbe, J., 2009. Simulation of the Middle Miocene Climate Optimum. Geophysical Research Letters 36.

Yu, Z., Robinson, P., McGoldrick, P., 2001. An evaluation of methods for the chemical decomposition of geological materials for trace element determination using ICP-MS. Geostandards Newsletter 25, 199-217.

Zachos, J.C., Dickens, G.R., Zeebe, R.E., 2008. An early Cenozoic perspective on greenhouse warming and carbon-cycle dynamics. Nature 451, 279-283.

Zahirovic, S., Matthews, K.J., Flament, N., Müller, R.D., Hill, K.C., Seton, M., Gurnis, M., 2016. Tectonic evolution and deep mantle structure of the eastern Tethys since the latest Jurassic. Earth-Science Reviews 162, 293-337.

Zhao, W., Sun, Y., Balsam, W., Lu, H., Liu, L., Chen, J., Ji, J., 2014. Hf-Nd isotopic variability in mineral dust from Chinese and Mongolian deserts: implications for sources and dispersal. Scientific Reports 4, 5837.

Appendix

Table A1: Results of Nd and Sr isotope analyses for the intervals between 15.8 and 9.5 Ma

Sample	Age (Ma)	$^{87}Sr/^{86}Sr$	2σ	ε_{Nd}	2σ
B-13H-3 (46-47)	9.498	0.71173	4.65E-05	-9.73	0.22
B-13H-3 (56-57)	9.520	0.71224	4.65E-05	-10.47	0.20
B-13H-3 (64-65)	9.538	0.71305	4.65E-05	-10.38	0.20
B-13H-3 (72-73)	9.556	0.71202	4.65E-05	-9.58	0.22
B-13H-3 (90-91)	9.596	0.71163	4.65E-05	-10.23	0.20
B-13H-3 (96-97)	9.609	0.71198	4.65E-05	-9.79	0.20
B-13H-3 (104-105)	9.627	0.71220	4.65E-05	-10.11	0.22
B-13H-4 (1-2)	9.655	0.71210	4.65E-05	-9.26	0.22
B-13H-4 (13-14)	9.681	0.71167	4.65E-05	-10.23	0.20
B-13H-4 (31-32)	9.722	0.71167	4.65E-05	-10.42	0.20
B-13H-4 (47-48)	9.758	0.71177	4.65E-05	-9.86	0.20
B-13H-4 (61-62)	9.789	0.71202	4.65E-05	-10.19	0.20
B-13H-4 (73-74)	9.816	0.71230	4.65E-05	-10.07	0.20
B-13H-4 (83-84)	9.838	0.71125	4.65E-05	-10.10	0.20
B-13H-4 (93-94)	9.861	0.71128	4.65E-05	-9.88	0.20
B-13H-4 (105-106)	9.887	0.71226	4.65E-05	-10.34	0.20
B-13H-4 (117-118)	9.914	0.71239	4.65E-05	-8.93	0.20
B-13H-4 (131-132)	9.946	0.71170	4.65E-05	-10.35	0.20
B-13H-4 (145-146)	9.977	0.71160	4.65E-05	-9.23	0.20
B-13H-5 (4-5)	9.997	0.71128	4.65E-05	-9.89	0.20
C-16H-3 (91-92)	10.497	0.71120	4.65E-05	-9.66	0.16
C-16H-3 (101-102)	10.519	0.71123	4.65E-05	-10.21	0.16
C-16H-3 (111-112)	10.541	0.71137	4.65E-05	-10.41	0.16
C-16H-3 (121-122)	10.564	0.71165	4.65E-05	-8.96	0.22
C-16H-3 (129-130)	10.582	0.71173	4.65E-05	-10.39	0.16
C-16H-3 (137-138)	10.600	0.71187	4.65E-05	-9.92	0.22
C-16H-3 (147-148)	10.622	0.71199	4.65E-05	-9.53	0.22
C-16H-4 (8-9)	10.647	0.71188	4.65E-05	-9.44	0.22
C-16H-4 (20-21)	10.673	0.71150	4.65E-05	-9.82	0.16
C-16H-4 (28-29)	10.691	0.71118	4.65E-05	-9.53	0.16
C-16H-4 (40-41)	10.718	0.71176	4.65E-05	-9.87	0.16
C-16H-4 (50-51)	10.741	0.71202	4.65E-05	-10.05	0.16
C-16H-4 (58-59)	10.759	0.71191	4.65E-05	-9.94	0.22
C-16H-4 (66-67)	10.777	0.71246	4.65E-05	-9.87	0.16
C-16H-4 (70-71)	10.792	0.71177	4.65E-05	-9.51	0.16
C-16H-4 (80-81)	10.829	0.71167	4.65E-05	-9.73	0.16
C-16H-4 (88-89)	10.859	0.71168	4.65E-05	-10.31	0.16
C-16H-4 (96-97)	10.889	0.71155	4.65E-05	-10.47	0.16
C-16H-4 (108-109)	10.934	0.71194	4.65E-05	-9.69	0.16
C-16H-4 (116-117)	10.964	0.71147	4.65E-05	-9.91	0.16
C-16H-4 (124-125)	10.994	0.71189	4.65E-05	-10.27	0.22

Table A1 (continued): Results of Nd and Sr isotope analyses for the intervals between 15.8 and 9.5 Ma.

Sample	Age (Ma)	$^{87}Sr/^{86}Sr$	2σ	ε_{Nd}	2σ
B-14H-3 (12-13)	12.883	0.71273	3.65E-05	-9.45	0.13
B-14H-3 (28-29)	12.911	0.71317	3.65E-05	-11.61	0.18
B-14H-3 (42-43)	12.936	0.71377	3.65E-05	-10.85	0.15
B-14H-3 (56-57)	12.961	0.71320	2.72E-05	-10.23	0.17
B-14H-3 (70-71)	12.985	0.71384	2.72E-05	-11.02	0.19
B-14H-3 (84-85)	13.013	0.71256	2.72E-05	-11.08	0.17
B-14H-3 (98-99)	13.042	0.71310	2.72E-05	-10.83	0.17
B-14H-3 (112-113)	13.062	0.71315	2.72E-05	-9.95	0.13
B-14H-3 (126-127)	13.078	0.71341	2.72E-05		
B-14H-3 (140-141)	13.094	0.71274	3.65E-05	-10.23	0.17
B-14H-4 (5-6)	13.111	0.71355	3.65E-05	-10.98	0.15
B-14H-4 (19-20)	13.126	0.71292	3.65E-05	-9.97	0.14
B-14H-4 (33-34)	13.142	0.71322	3.65E-05	-11.65	0.21
B-14H-4 (49-50)	13.167	0.71322	2.72E-05	-10.61	0.14
B-14H-4 (61-62)	13.186	0.71291	2.72E-05	-10.77	0.15
B-14H-4 (75-76)	13.209	0.71366	2.72E-05	-10.30	0.15
B-14H-4 (87-88)	13.229	0.71362	2.72E-05	-10.22	0.13
B-14H-4 (101-102)	13.254	0.71306	2.72E-05	-10.01	0.12
B-14H-4 (113-114)	13.276	0.71308	2.72E-05	-9.11	0.20
B-14H-4 (125-126)	13.297	0.71337	2.72E-05	-11.00	0.15
B-14H-5 (98-99)	13.498	0.71525	2.35E-05	-12.12	0.42
B-14H-5 (116-117)	13.523	0.71658	2.35E-05	-12.74	0.42
C-18H-2 (41-42)	13.551	0.71473	2.35E-05	-11.96	0.42
C-18H-2 (63-64)	13.572	0.71505	2.35E-05	-12.87	0.42
C-18H-2 (87-88)	13.596	0.71567	2.35E-05	-12.26	0.42
C-18H-2 (109-110)	13.617	0.71415	2.35E-05	-12.83	0.42
C-18H-2 (131-132)	13.637	0.71502	2.35E-05	-11.60	0.42
C-18H-3 (2-3)	13.654	0.71658	2.35E-05	-11.27	0.42
C-18H-3 (24-25)	13.671	0.71591	2.35E-05	-12.33	0.42
C-18H-3 (46-47)	13.688	0.71515	2.35E-05	-13.32	0.42
C-18H-3 (68-69)	13.705	0.71548	2.35E-05	-12.51	0.42
C-18H-3 (90-91)	13.720	0.71472	2.35E-05	-10.03	0.42
C-18H-3 (112-113)	13.732	0.71560	2.35E-05	-11.85	0.42
C-18H-3 (134-135)	13.744	0.71469	2.35E-05	-11.25	0.42
C-18H-4 (9-10)	13.757	0.71592	2.35E-05	-10.67	0.42
C-18H-4 (31-32)	13.768	0.71506	2.35E-05	-10.03	0.42
B-15H-1 (63-64)	13.780	0.71621	2.35E-05	-12.10	0.42
B-15H-1 (71-72)	13.784	0.71207	4.65E-05	-12.87	0.22
B-15H-1 (79-80)	13.789	0.71267	4.65E-05	-12.66	0.20
B-15H-1 (85-86)	13.792	0.71636	2.35E-05	-11.37	0.42
B-15H-1 (93-94)	13.796	0.71311	4.65E-05	-10.29	0.22
B-15H-1 (99-100)	13.799	0.71252	3.65E-05	-11.56	0.20
B-15H-1 (107-108)	13.803	0.71597	2.35E-05	-12.42	0.42
B-15H-1 (113-114)	13.807	0.71320	4.65E-05	-11.55	0.22

Table A1 (continued): Results of Nd and Sr isotope analyses for the intervals between 15.8 and 9.5 Ma.

Sample	Age (Ma)	$^{87}Sr/^{86}Sr$	2σ	ε_{Nd}	2σ
B-15H-1 (119-120)	13.810	0.71249	4.65E-05	-10.79	0.08
B-15H-1 (125-126)	13.813	0.71209	3.65E-05	-12.23	0.20
B-15H-1 (129-130)	13.815	0.71334	3.65E-05	-12.78	0.22
B-15H-1 (137-138)	13.819	0.71395	4.65E-05	-12.21	0.08
B-15H-1 (143-144)	13.822	0.71338	4.65E-05	-11.63	0.08
B-15H-1 (149-150)	13.826	0.71466	3.65E-05	-12.76	0.16
B-15H-3 (5-6)	13.831	0.71326	2.72E-05	-11.55	0.16
B-15H-3 (11-12)	13.838	0.71280	2.72E-05	-10.93	0.16
B-15H-3 (15-16)	13.843	0.71391	2.72E-05	-11.75	0.16
B-15H-3 (21-22)	13.850	0.71364	2.72E-05	-12.03	0.22
B-15H-3 (23-24)	13.852	0.71396	5.03E-05	-12.01	0.16
B-15H-3 (29-30)	13.859	0.71388	5.03E-05	-10.41	0.16
B-15H-3 (33-34)	13.864	0.71447	5.03E-05	-10.22	0.16
B-15H-3 (41-42)	13.873	0.71384	5.03E-05	-13.16	0.16
B-15H-3 (45-46)	13.878	0.71561	5.03E-05	-12.88	0.16
B-15H-3 (47-48)	13.880	0.71425	5.03E-05	-12.56	0.16
B-15H-3 (59-60)	13.894	0.71340	5.03E-05	-11.90	0.16
B-15H-3 (69-70)	13.906	0.71372	5.03E-05	-12.18	0.22
B-15H-3 (75-76)	13.923	0.71424	5.03E-05	-11.44	0.16
B-15H-3 (79-80)	13.934	0.71230	2.72E-05	-10.78	0.16
B-15H-3 (89-90)	13.961	0.71448	2.72E-05	-12.50	0.16
B-15H-3 (91-92)	13.967	0.71319	2.72E-05	-12.02	0.22
B-15H-3 (93-94)	13.973	0.71369	4.65E-05	-12.53	0.16
B-15H-3 (99-100)	13.989	0.71322	4.65E-05	-12.32	0.16
B-15H-3 (103-104)	13.997	0.71469	4.65E-05	-12.87	0.16
B-15H-3 (105-106)	14.000	0.71448	4.65E-05	-12.46	0.16
C-19H-3 (45-46)	15.298	0.71310	2.50E-05	-10.66	0.42
C-19H-3 (53-54)	15.319	0.71231	2.72E-05	-11.08	0.22
C-19H-3 (57-58)	15.330	0.71416	2.50E-05	-10.43	0.42
C-19H-3 (69-70)	15.362	0.71333	2.50E-05	-9.35	0.42
C-19H-3 (81-82)	15.393	0.71272	2.50E-05	-10.60	0.42
C-19H-3 (93-94)	15.425	0.71254	2.50E-05	-11.34	0.42
C-19H-3 (105-106)	15.457	0.71384	2.50E-05	-8.64	0.42
C-19H-3 (109-110)	15.467	0.71270	2.72E-05	-11.22	0.22
C-19H-3 (117-118)	15.488	0.71365	2.50E-05	-9.20	0.42
C-19H-3 (123-124)	15.504	0.71209	3.65E-05	-10.66	0.16
C-19H-3 (129-130)	15.520	0.71443	2.50E-05	-9.59	0.42
C-19H-3 (135-136)	15.536	0.71280	3.65E-05	-10.72	0.22
B-16H-1 (147-148)	15.552	0.71458	2.50E-05	-9.41	0.42
B-16H-2 (13-14)	15.594	0.71243	3.65E-05	-12.01	0.16
B-16H-2 (17-18)	15.604	0.71461	2.50E-05	-8.98	0.42
B-16H-2 (19-20)	15.610	0.71199	2.72E-05	-11.65	0.16
B-16H-2 (29-30)	15.643	0.71577	2.50E-05	-9.97	0.42
B-16H-2 (37-38)	15.669	0.71343	2.50E-05	-9.37	0.42
B-16H-2 (47-48)	15.702	0.71276	2.72E-05	-12.26	0.22

Table A1 (continued): Results of Nd and Sr isotope analyses for the intervals between 15.8 and 9.5 Ma.

Sample	Age (Ma)	$^{87}Sr/^{86}Sr$	2σ	ε_{Nd}	2σ
B-16H-2 (57-58)	15.736	0.71518	2.72E-05	-12.48	0.16
B-16H-2 (69-70)	15.775	0.71528	2.72E-05	-11.94	0.16
B-16H-2 (77-78)	15.802	0.71496	2.72E-05	-12.31	0.16

Table A2: Nd and Sr isotope results for the Irrawaddy River endmember, measured on the <2µm (clay) and >2µm fractions of the samples.

Sample	Age (Ma)	$^{87}Sr/^{86}Sr$	2σ	ε_{Nd}	2σ
IR1 12,5 (<2µm)	Holocene	0.71678	3.38E-05	-6.79	0.18
IR1 2-1 (<2µm)	Holocene	0.71696	3.38E-05	-6.08	0.18
IR1 2-4 (<2µm)	Holocene	0.71670	3.38E-05	-6.28	0.18
IR1 2-5 (<2µm)	Holocene	0.71726	3.38E-05	-6.34	0.18
IR1 3-2 (<2µm)	Holocene	0.71724	3.38E-05	-6.57	0.18
IR1 3-4 (<2µm)	Holocene	0.71459	3.38E-05	-6.53	0.18
IR1 5-4 (<2µm)	Holocene	0.71701	3.38E-05	-6.30	0.18
IR1 8-1 (<2µm)	Holocene	0.71780	3.38E-05	-6.53	0.18
IR1 9-2 (<2µm)	Holocene	0.71640	3.38E-05	-6.76	0.18
IR2 3-2 (<2µm)	Holocene	0.71459	3.38E-05	-6.95	0.18
IR2 4-5 (<2µm)	Holocene	0.71639	3.38E-05	-5.84	0.18
IR1 12,5 (>2µm)	Holocene	0.71590	3.38E-05	-8.97	0.18
IR1 2-1 (>2µm)	Holocene	0.71442	3.38E-05	-8.58	0.18
IR1 2-4 (>2µm)	Holocene	0.71424	3.38E-05	-8.42	0.18
IR1 2-5 (>2µm)	Holocene	0.71352	3.38E-05	-8.91	0.18
IR1 3-2 (>2µm)	Holocene	0.71158	3.38E-05	n.a.	0.18
IR1 3-4 (>2µm)	Holocene	0.71319	3.38E-05	-8.52	0.18
IR1 5-4 (>2µm)	Holocene	0.71445	3.38E-05	-8.46	0.18
IR1 8-1 (>2µm)	Holocene	0.71522	3.38E-05	-8.13	0.18
IR1 9-2 (>2µm)	Holocene	0.71380	3.38E-05	-8.46	0.18
IR2 3-2 (>2µm)	Holocene	0.71436	3.38E-05	-8.50	0.18
IR2 4-5 (>2µm)	Holocene	0.71663	3.38E-05	-7.94	0.18

Table A3: Pb isotope results for the intervals between 15.8 and 9.5 Ma.

Sample	Age (Ma)	$^{206}Pb/^{204}Pb$	2σ	$^{207}Pb/^{204}Pb$	2σ	$^{208}Pb/^{204}Pb$	2σ
C-19H-3 (45-46)	15.298	18.948	0.0006	15.775	0.0005	39.399	0.0013
C-19H-3 (53-54)	15.319	18.928	0.0007	15.762	0.0006	39.319	0.0014
C-19H-3 (57-58)	15.330	18.962	0.0005	15.781	0.0005	39.434	0.0014
C-19H-3 (69-70)	15.362	18.891	0.0005	15.753	0.0004	39.308	0.0012
C-19H-3 (81-82)	15.393	18.942	0.0005	15.774	0.0004	39.394	0.0014
C-19H-3 (93-94)	15.425	18.898	0.0005	15.762	0.0006	39.340	0.0016
C-19H-3 (105-106)	15.457	18.879	0.0005	15.755	0.0005	39.317	0.0012
C-19H-3 (109-110)	15.467	18.893	0.0007	15.757	0.0006	39.311	0.0019
C-19H-3 (117-118)	15.488	18.901	0.0006	15.761	0.0006	39.338	0.0016
C-19H-3 (123-124)	15.504	18.858	0.0008	15.749	0.0007	39.275	0.0019
C-19H-3 (129-130)	15.520	18.898	0.0005	15.762	0.0005	39.344	0.0014
C-19H-3 (135-136)	15.536	18.861	0.0010	15.746	0.0008	39.267	0.0024
B-16H-1 (147-148)	15.552	18.916	0.0005	15.771	0.0005	39.376	0.0014
B-16H-2 (13-14)	15.594	18.885	0.0007	15.759	0.0007	39.318	0.0019
B-16H-2 (17-18)	15.604	18.884	0.0005	15.761	0.0004	39.344	0.0012
B-16H-2 (19-20)	15.610	18.870	0.0009	15.754	0.0008	39.304	0.0022
B-16H-2 (29-30)	15.643	18.872	0.0006	15.761	0.0005	39.339	0.0015
B-16H-2 (37-38)	15.669	18.878	0.0006	15.759	0.0006	39.338	0.0014
B-16H-2 (47-48)	15.702	18.866	0.0007	15.750	0.0006	39.292	0.0016
B-16H-2 (57-58)	15.736	18.870	0.0008	15.751	0.0006	39.291	0.0017
B-16H-2 (69-70)	15.775	18.860	0.0009	15.754	0.0009	39.299	0.0026
B-16H-2 (77-78)	15.802	18.887	0.0007	15.759	0.0006	39.315	0.0015
B-14H-5 (98-99)	13.498	18.930	0.0006	15.764	0.0005	39.334	0.0013
B-14H-5 (116-117)	13.523	19.001	0.0006	15.774	0.0006	39.369	0.0017
C-18H-2 (41-42)	13.551	18.963	0.0005	15.771	0.0004	39.359	0.0014
C-18H-2 (63-64)	13.572	18.969	0.0007	15.781	0.0006	39.413	0.0018
C-18H-2 (87-88)	13.596	18.960	0.0006	15.774	0.0006	39.393	0.0016
C-18H-2 (109-110)	13.617	18.997	0.0007	15.778	0.0006	39.407	0.0017
C-18H-2 (131-132)	13.637	18.907	0.0014	15.760	0.0010	39.318	0.0026
C-18H-3 (2-3)	13.654	18.928	0.0010	15.765	0.0009	39.355	0.0021
C-18H-3 (24-25)	13.671	18.960	0.0008	15.777	0.0010	39.414	0.0025
C-18H-3 (46-47)	13.688	18.965	0.0011	15.784	0.0008	39.416	0.0024
C-18H-3 (68-69)	13.705	18.939	0.0010	15.781	0.0010	39.400	0.0023
C-18H-3 (90-91)	13.720	18.871	0.0010	15.741	0.0008	39.256	0.0021
C-18H-3 (112-113)	13.732	18.941	0.0007	15.774	0.0006	39.379	0.0016
C-18H-3 (134-135)	13.744	18.926	0.0008	15.765	0.0007	39.346	0.0021
C-18H-4 (9-10)	13.757	18.906	0.0009	15.754	0.0007	39.302	0.0022
C-18H-4 (31-32)	13.768	18.973	0.0009	15.786	0.0010	39.424	0.0022
B-15H-1 (63-64)	13.780	18.918	0.0005	15.757	0.0005	39.306	0.0013
B-15H-1 (71-72)	13.784	19.022	0.0005	15.799	0.0005	39.476	0.0014
B-15H-1 (79-80)	13.789	19.048	0.0005	15.799	0.0006	39.477	0.0017
B-15H-1 (85-86)	13.792	18.986	0.0006	15.776	0.0005	39.389	0.0013
B-15H-1 (93-94)	13.796	18.929	0.0007	15.761	0.0008	39.321	0.0022
B-15H-1 (99-100)	13.799	18.985	0.0010	15.783	0.0008	39.402	0.0023
B-15H-1 (107-108)	13.803	19.055	0.0009	15.803	0.0010	39.505	0.0020

Table A3 (continued): Pb isotope results for the intervals between 15.8 and 9.5 Ma.

Sample	Age (Ma)	$^{206}Pb/^{204}Pb$	2σ	$^{207}Pb/^{204}Pb$	2σ	$^{208}Pb/^{204}Pb$	2σ
B-15H-1 (113-114)	13.807	18.866	0.0008	15.759	0.0008	39.211	0.0021
B-15H-1 (119-120)	13.810	18.931	0.0007	15.764	0.0007	39.327	0.0017
B-15H-1 (125-126)	13.813	18.987	0.0006	15.784	0.0006	39.399	0.0018
B-15H-1 (129-130)	13.815	19.048	0.0010	15.801	0.0010	39.476	0.0020
B-15H-1 (137-138)	13.819	19.044	0.0008	15.796	0.0007	39.468	0.0020
B-15H-1 (143-144)	13.822	18.969	0.0008	15.778	0.0007	39.406	0.0020
B-15H-1 (149-150)	13.826	18.990	0.0010	15.788	0.0010	39.452	0.0020
B-15H-3 (5-6)	13.831	18.936	0.0010	15.769	0.0010	39.369	0.0020
B-15H-3 (11-12)	13.838	18.942	0.0010	15.764	0.0010	39.342	0.0020
B-15H-3 (15-16)	13.843	18.977	0.0010	15.776	0.0010	39.389	0.0010
B-15H-3 (21-22)	13.850	19.013	0.0010	15.788	0.0010	39.446	0.0020
B-15H-3 (23-24)	13.852	18.996	0.0010	15.779	0.0010	39.418	0.0020
B-15H-3 (29-30)	13.859	18.939	0.0010	15.758	0.0010	39.324	0.0020
B-15H-3 (33-34)	13.864	18.949	0.0010	15.757	0.0010	39.316	0.0020
B-15H-3 (41-42)	13.873	19.009	0.0010	15.798	0.0010	39.483	0.0020
B-15H-3 (45-46)	13.878	19.096	0.0010	15.807	0.0010	39.528	0.0020
B-15H-3 (47-48)	13.880	19.038	0.0010	15.792	0.0010	39.473	0.0020
B-15H-3 (59-60)	13.894	19.011	0.0010	15.785	0.0010	39.435	0.0020
B-15H-3 (69-70)	13.906	19.022	0.0010	15.787	0.0010	39.440	0.0020
B-15H-3 (75-76)	13.923	18.978	0.0010	15.775	0.0010	39.393	0.0010
B-15H-3 (79-80)	13.934	18.917	0.0010	15.760	0.0010	39.333	0.0020
B-15H-3 (89-90)	13.961	18.989	0.0010	15.778	0.0010	39.418	0.0020
B-15H-3 (91-92)	13.967	18.967	0.0011	15.774	0.0011	39.401	0.0033
B-15H-3 (93-94)	13.973	18.956	0.0010	15.781	0.0010	39.425	0.0020
B-15H-3 (99-100)	13.989	18.974	0.0010	15.783	0.0010	39.422	0.0020
B-15H-3 (103-104)	13.997	18.969	0.0010	15.784	0.0010	39.436	0.0020
B-15H-3 (105-106)	14.000	18.977	0.0010	15.777	0.0010	39.396	0.0020
B-14H-3 (12-13)	12.883	18.888	0.0010	15.752	0.0010	39.317	0.0020
B-14H-3 (28-29)	12.911	18.929	0.0010	15.764	0.0010	39.376	0.0020
B-14H-3 (42-43)	12.936	18.920	0.0010	15.754	0.0010	39.319	0.0030
B-14H-3 (56-57)	12.961	18.902	0.0010	15.747	0.0010	39.294	0.0020
B-14H-3 (70-71)	12.985	18.908	0.0010	15.761	0.0010	39.352	0.0030
B-14H-3 (84-85)	13.013	18.906	0.0010	15.761	0.0010	39.351	0.0020
B-14H-3 (98-99)	13.042	18.908	0.0010	15.757	0.0010	39.340	0.0020
B-14H-3 (112-113)	13.062	18.892	0.0010	15.757	0.0010	39.331	0.0020
B-14H-3 (126-127)	13.078	18.901	0.0000	15.760	0.0000	39.337	0.0010
B-14H-3 (140-141)	13.094	18.888	0.0010	15.758	0.0010	39.320	0.0020
B-14H-4 (5-6)	13.111	18.895	0.0010	15.756	0.0010	39.321	0.0020
B-14H-4 (19-20)	13.126	18.901	0.0010	15.756	0.0010	39.319	0.0020
B-14H-4 (33-34)	13.142	18.922	0.0010	15.763	0.0010	39.351	0.0020
B-14H-4 (49-50)	13.167	18.876	0.0010	15.753	0.0010	39.302	0.0020
B-14H-4 (61-62)	13.186	18.878	0.0010	15.755	0.0010	39.313	0.0020
B-14H-4 (75-76)	13.209	18.888	0.0010	15.755	0.0010	39.312	0.0020
B-14H-4 (87-88)	13.229	18.910	0.0010	15.764	0.0010	39.355	0.0020

Table A3 (continued): Pb isotope results for the intervals between 15.8 and 9.5 Ma.

Sample	Age (Ma)	$^{206}Pb/^{204}Pb$	2σ	$^{207}Pb/^{204}Pb$	2σ	$^{208}Pb/^{204}Pb$	2σ
B-14H-4 (101-102)	13.254	18.911	0.0010	15.763	0.0010	39.339	0.0020
B-14H-4 (113-114)	13.276	18.888	0.0010	15.754	0.0010	39.308	0.0020
B-14H-4 (125-126)	13.297	18.890	0.0010	15.750	0.0010	39.294	0.0020
C-16H-3 (91-92)	10.497	18.838	0.0007	15.729	0.0007	39.240	0.0017
C-16H-3 (101-102)	10.519	18.853	0.0007	15.726	0.0006	39.233	0.0018
C-16H-3 (111-112)	10.541	18.873	0.0006	15.743	0.0004	39.302	0.0013
C-16H-3 (121-122)	10.564	18.863	0.0009	15.738	0.0007	39.282	0.0021
C-16H-3 (129-130)	10.582	18.865	0.0007	15.736	0.0007	39.280	0.0019
C-16H-3 (137-138)	10.600	18.861	0.0005	15.735	0.0007	39.278	0.0019
C-16H-3 (147-148)	10.622	18.873	0.0008	15.744	0.0008	39.309	0.0019
C-16H-4 (8-9)	10.647	18.864	0.0007	15.739	0.0007	39.286	0.0019
C-16H-4 (20-21)	10.673	18.857	0.0007	15.741	0.0008	39.284	0.0021
C-16H-4 (28-29)	10.691	18.855	0.0006	15.735	0.0005	39.269	0.0015
C-16H-4 (40-41)	10.718	18.880	0.0007	15.742	0.0006	39.301	0.0017
C-16H-4 (50-51)	10.741	18.873	0.0009	15.745	0.0008	39.314	0.0023
C-16H-4 (58-59)	10.759	18.880	0.0006	15.746	0.0007	39.314	0.0017
C-16H-4 (66-67)	10.777	18.870	0.0008	15.736	0.0007	39.284	0.0018
C-16H-4 (70-71)	10.792	18.850	0.0007	15.737	0.0007	39.280	0.0019
C-16H-4 (80-81)	10.829	18.862	0.0007	15.739	0.0006	39.287	0.0017
C-16H-4 (88-89)	10.859	18.868	0.0007	15.737	0.0006	39.283	0.0016
C-16H-4 (96-97)	10.889	18.890	0.0007	15.741	0.0007	39.294	0.0020
C-16H-4 (108-109)	10.934	18.862	0.0008	15.742	0.0007	39.301	0.0019
C-16H-4 (116-117)	10.964	18.863	0.0008	15.742	0.0007	39.299	0.0021
C-16H-4 (124-125)	10.994	18.875	0.0006	15.748	0.0006	39.318	0.0015
B-13H-3 (46-47)	9.498	18.864	0.0007	15.742	0.0006	39.303	0.0017
B-13H-3 (56-57)	9.520	18.881	0.0006	15.740	0.0006	39.299	0.0023
B-13H-3 (64-65)	9.538	18.889	0.0008	15.742	0.0007	39.307	0.0019
B-13H-3 (72-73)	9.556	18.864	0.0008	15.739	0.0007	39.291	0.0019
B-13H-3 (90-91)	9.596	18.877	0.0009	15.741	0.0008	39.299	0.0021
B-13H-3 (96-97)	9.609	18.864	0.0009	15.728	0.0009	39.250	0.0022
B-13H-3 (104-105)	9.627	18.885	0.0007	15.740	0.0008	39.302	0.0023
B-13H-4 (1-2)	9.655	18.879	0.0008	15.739	0.0008	39.291	0.0020
B-13H-4 (13-14)	9.681	18.892	0.0008	15.743	0.0008	39.309	0.0022
B-13H-4 (31-32)	9.722	18.882	0.0007	15.737	0.0007	39.291	0.0019
B-13H-4 (47-48)	9.758	18.889	0.0010	15.740	0.0010	39.303	0.0028
B-13H-4 (61-62)	9.789	18.899	0.0006	15.745	0.0006	39.319	0.0016
B-13H-4 (73-74)	9.816	18.901	0.0006	15.747	0.0006	39.325	0.0016
B-13H-4 (83-84)	9.838	18.897	0.0009	15.745	0.0009	39.317	0.0022
B-13H-4 (93-94)	9.861	18.881	0.0009	15.736	0.0009	39.279	0.0024
B-13H-4 (105-106)	9.887	18.887	0.0007	15.742	0.0007	39.305	0.0020
B-13H-4 (117-118)	9.914	18.867	0.0008	15.741	0.0007	39.298	0.0019
B-13H-4 (131-132)	9.946	18.890	0.0009	15.743	0.0007	39.303	0.0019
B-13H-4 (145-146)	9.977	18.863	0.0008	15.739	0.0008	39.288	0.0023
B-13H-5 (4-5)	9.997	18.853	0.0017	15.731	0.0013	39.255	0.0038

Table A4: Pb isotope results for the Irrawaddy River endmember, measured on the <2µm (clay) and >2µm fractions of the samples.

Sample	Age (Ma)	$^{206}Pb/^{204}Pb$	2σ	$^{207}Pb/^{204}Pb$	2σ	$^{208}Pb/^{204}Pb$	2σ
IR1 12,5 (<2µm)	Holocene	18.733	0.0010	15.695	0.0010	39.151	0.0026
IR1 2-1 (<2µm)	Holocene	18.710	0.0007	15.679	0.0007	39.051	0.0018
IR1 2-4 (<2µm)	Holocene	18.714	0.0006	15.680	0.0006	39.064	0.0016
IR1 2-5 (<2µm)	Holocene	18.769	0.0007	15.665	0.0008	39.078	0.0023
IR1 3-2 (<2µm)	Holocene	18.786	0.0008	15.673	0.0008	39.116	0.0020
IR1 3-4 (<2µm)	Holocene	18.700	0.0006	15.672	0.0006	39.034	0.0015
IR1 5-4 (<2µm)	Holocene	18.807	0.0006	15.679	0.0006	39.150	0.0016
IR1 8-1 (<2µm)	Holocene	18.793	0.0007	15.679	0.0007	39.135	0.0019
IR1 9-2 (<2µm)	Holocene	n.a.		n.a.		n.a.	
IR2 3-2 (<2µm)	Holocene	18.757	0.0005	15.684	0.0004	39.117	0.0014
IR2 4-5 (<2µm)	Holocene	18.737	0.0006	15.677	0.0007	39.082	0.0019
IR1 12,5 (>2µm)	Holocene	18.936	0.0005	15.717	0.0005	39.464	0.0014
IR1 2-1 (>2µm)	Holocene	18.869	0.0007	15.710	0.0006	39.283	0.0016
IR1 2-4 (>2µm)	Holocene	18.842	0.0009	15.705	0.0009	39.243	0.0023
IR1 2-5 (>2µm)	Holocene	19.191	0.0007	15.741	0.0007	39.575	0.0017
IR1 3-2 (>2µm)	Holocene	18.998	0.0005	15.724	0.0004	39.880	0.0013
IR1 3-4 (>2µm)	Holocene	18.888	0.0006	15.703	0.0007	39.244	0.0018
IR1 5-4 (>2µm)	Holocene	18.971	0.0008	15.720	0.0007	39.427	0.0021
IR1 8-1 (>2µm)	Holocene	18.952	0.0010	15.715	0.0008	39.382	0.0022
IR1 9-2 (>2µm)	Holocene	18.936	0.0007	15.712	0.0007	39.303	0.0020
IR2 3-2 (>2µm)	Holocene	18.946	0.0007	15.719	0.0006	39.383	0.0017
IR2 4-5 (>2µm)	Holocene	18.881	0.0007	15.709	0.0006	39.324	0.0015

Table A5: Nd and Sr isotope results for the late Miocene interval from 9 to 5 Ma.

Sample	Age (Ma)	$^{87}Sr/^{86}Sr$	2σ	ε_{Nd}	2σ
C-9H-2 (118-119)	5.016	0.71595	1.72E-05	-10.87	0.24
C-9H-4 (16-17)	5.126	0.71436	1.72E-05	-9.49	0.24
C-9H-5 (127-128)	5.332	0.71534	1.72E-05	-10.87	0.24
B-8H-3 (142-143)	5.528	0.71417	1.72E-05	-10.23	0.24
B-8H-4 (123-124)	5.633	0.71464	1.72E-05	-10.03	0.24
B-8H-5 (32-33)	5.682	0.71411	1.72E-05	-9.81	0.24
B-8H-5 (99-100)	5.738	0.71440	1.72E-05	-10.38	0.24
C-10H-3 (33-34)	5.797	0.71458	1.72E-05	-10.46	0.24
C-10H-4 (9-10)	5.850	0.71411	1.72E-05	-9.42	0.24
C-10H-4 (81-82)	5.903	0.71352	1.72E-05	-10.09	0.24
C-10H-5 (7-8)	5.958	0.71328	1.72E-05	-10.14	0.24
C-10H-5 (79-80)	6.011	0.71367	1.72E-05	-10.18	0.24
C-10H-6 (71-72)	6.118	0.71323	1.72E-05	-10.62	0.24
C-10H-6 (143-144)	6.162	0.71364	1.72E-05	-10.76	0.24
C-10H-7 (61-62)	6.203	0.71357	1.72E-05	-10.66	0.24

Table A5 (continued): Nd and Sr isotope results for the late Miocene interval from 9 to 5 Ma.

Sample	Age (Ma)	$^{87}Sr/^{86}Sr$	2σ	ε_{Nd}	2σ
B-9H-3 (68-69)	6.239	0.71318	1.72E-05	-9.58	0.24
B-9H-3 (148-149)	6.288	0.71325	1.72E-05	-9.13	0.24
B-9H-4 (73-74)	6.342	0.71313	1.72E-05	-9.76	0.24
C-11H-1 (53-54)	6.399	0.71393	1.72E-05	-9.85	0.24
C-11H-1 (142-143)	6.470	0.71356	1.72E-05	-10.56	0.24
C-11H-3 (9-10)	6.635	0.71367	1.72E-05	-9.76	0.24
A-10H-2 (69-70)	6.770	0.71370	1.72E-05	-9.71	0.24
A-10H-3 (98-99)	6.913	0.71379	1.72E-05	-10.35	0.24
A-10H-4 (117-118)	7.043	0.71261	1.72E-05	-9.38	0.24
A-10H-5 (142-143)	7.166	0.71361	1.72E-05	-10.21	0.24
C-12H-3 (17-18)	7.300	0.71371	1.72E-05	-10.48	0.24
B-11H-2 (39-40)	7.481	0.71374	1.72E-05	-11.39	0.24
B-11H-3 (106-107)	7.591	0.71380	1.72E-05	-10.12	0.24
B-11H-4 (127-128)	7.674	0.71351	1.72E-05	-10.23	0.24
B-11H-5 (148-149)	7.807	0.71378	1.72E-05	-11.21	0.24
A-11H-6 (13-14)	7.909	0.71348	1.72E-05	-11.16	0.24
C-13H-4 (95-96)	8.000	0.71273	1.72E-05	-9.68	0.24
B-12H-1 (132-133)	8.124	0.71465	1.72E-05	-10.81	0.24
B-12H-2 (91-92)	8.196	0.71271	1.72E-05	-10.91	0.24
B-12H-2 (137-138)	8.226	0.71439	1.72E-05	-10.93	0.24
B-12H-3 (30-31)	8.254	0.71381	1.72E-05	-11.14	0.24
B-12H-3 (62-63)	8.275	0.71385	1.72E-05	-11.16	0.24
B-12H-3 (106-107)	8.304	0.71367	1.72E-05	-11.44	0.24
B-12H-3 (144-145)	8.330	0.71316	1.72E-05	-10.64	0.24
B-12H-4 (34-35)	8.356	0.71319	1.72E-05	-9.25	0.24
B-12H-5 (16-17)	8.449	0.71380	1.72E-05	-10.91	0.24
B-12H-5 (144-145)	8.545	0.71309	1.72E-05	-10.37	0.24
C-15H-3 (78-79)	8.647	0.71304	1.72E-05	-10.81	0.24
C-15H-4 (58-59)	8.857	0.71332	1.72E-05	-10.75	0.24

Table A6: Pb isotope results for the late Miocene interval from 9 to 5 Ma.

Sample	Age (Ma)	$^{206}Pb/^{204}Pb$	2σ	$^{207}Pb/^{204}Pb$	2σ	$^{208}Pb/^{204}Pb$	2σ
C-9H-2 (118-119)	5.016	19.035	0.001	15.757	0.001	39.451	0.003
C-9H-4 (16-17)	5.126	18.972	0.001	15.740	0.001	39.344	0.003
C-9H-5 (127-128)	5.332	19.015	0.001	15.758	0.001	39.440	0.004
B-8H-3 (142-143)	5.528	19.014	0.001	15.753	0.001	39.424	0.003
B-8H-4 (123-124)	5.633	18.973	0.001	15.747	0.001	39.363	0.003
B-8H-5 (32-33)	5.682	19.003	0.001	15.754	0.001	39.409	0.002
B-8H-5 (99-100)	5.738	19.000	0.001	15.750	0.001	39.409	0.003
C-10H-3 (33-34)	5.797	18.980	0.001	15.746	0.001	39.375	0.003
C-10H-4 (9-10)	5.850	18.959	0.001	15.741	0.001	39.342	0.003
C-10H-4 (81-82)	5.903	19.012	0.001	15.757	0.001	39.423	0.003
C-10H-5 (7-8)	5.958	19.028	0.001	15.764	0.001	39.464	0.003
C-10H-5 (79-80)	6.011	19.013	0.001	15.758	0.001	39.429	0.002
C-10H-6 (71-72)	6.118	19.026	0.001	15.761	0.001	39.445	0.003
C-10H-6 (143-144)	6.162	18.957	0.002	15.753	0.001	39.340	0.003
C-10H-7 (61-62)	6.203	19.044	0.001	15.763	0.001	39.463	0.003
B-9H-3 (68-69)	6.239	18.960	0.001	15.744	0.001	39.359	0.004
B-9H-3 (148-149)	6.288	18.945	0.001	15.741	0.001	39.334	0.002
B-9H-4 (73-74)	6.342	18.973	0.002	15.749	0.001	39.376	0.003
C-11H-1 (53-54)	6.399	18.995	0.001	15.751	0.001	39.393	0.003
C-11H-1 (142-143)	6.470	18.986	0.001	15.753	0.001	39.404	0.003
C-11H-3 (9-10)	6.635	18.995	0.001	15.750	0.001	39.390	0.003
A-10H-2 (69-70)	6.770	18.975	0.001	15.742	0.001	39.346	0.003
A-10H-3 (98-99)	6.913	18.996	0.001	15.754	0.001	39.400	0.003
A-10H-4 (117-118)	7.043	18.974	0.001	15.746	0.001	39.357	0.003
A-10H-5 (142-143)	7.166	18.973	0.001	15.747	0.001	39.357	0.003
C-12H-3 (17-18)	7.300	18.992	0.001	15.754	0.001	39.415	0.003
B-11H-2 (39-40)	7.481	19.037	0.001	15.767	0.001	39.493	0.003
B-11H-3 (106-107)	7.591	18.987	0.002	15.751	0.001	39.404	0.004
B-11H-4 (127-128)	7.674	18.984	0.001	15.752	0.001	39.413	0.003
B-11H-5 (148-149)	7.807	19.017	0.001	15.765	0.001	39.471	0.003
A-11H-6 (13-14)	7.909	19.067	0.001	15.770	0.001	39.489	0.003
C-13H-4 (95-96)	8.000	18.957	0.001	15.743	0.001	39.343	0.003
B-12H-1 (132-133)	8.124	19.009	0.001	15.754	0.001	39.412	0.003
B-12H-2 (91-92)	8.196	19.051	0.001	15.767	0.001	39.468	0.003
B-12H-2 (137-138)	8.226	19.033	0.001	15.766	0.001	39.448	0.004
B-12H-3 (30-31)	8.254	19.055	0.001	15.772	0.001	39.470	0.003
B-12H-3 (62-63)	8.275	19.066	0.001	15.770	0.001	39.474	0.003
B-12H-3 (106-107)	8.304	19.084	0.001	15.781	0.001	39.517	0.004
B-12H-3 (144-145)	8.330	19.026	0.001	15.766	0.001	39.447	0.003
B-12H-4 (34-35)	8.356	18.966	0.001	15.744	0.001	39.328	0.003
B-12H-5 (16-17)	8.449	19.000	0.001	15.756	0.001	39.409	0.004
B-12H-5 (144-145)	8.545	18.973	0.001	15.755	0.001	39.395	0.003
C-15H-3 (78-79)	8.647	19.040	0.001	15.767	0.001	39.452	0.002
C-15H-4 (58-59)	8.857	18.973	0.001	15.761	0.001	39.426	0.003

Table A7: Hf and Nd isotope results for selected samples across all intervals (15.8-5 Ma). The ε_{Hf} (clay array) was calculated after Bayon et al. (2016) using ε_{Hf} (clay array) = 0.78 × εNd + 5.23.

Sample	Age (Ma)	ε_{Hf}	2σ	ε_{Nd}	ε_{Hf} (clay array)	$\Delta\varepsilon_{Hf\ clay}$
C-9H-2 (118-119)	5.016	0.59	0.47	-10.87	-3.25	3.84
C-9H-5 (127-128)	5.332	2.04	0.47	-10.87	-3.25	5.29
B-8H-3 (142-143)	5.528	1.94	0.47	-10.23	-2.75	4.69
B-8H-5 (99-100)	5.738	2.35	0.47	-10.38	-2.87	5.21
C-10H-4 (9-10)	5.850	1.89	0.47	-9.42	-2.11	4.00
C-10H-5 (7-8)	5.958	3.41	0.47	-10.14	-2.68	6.09
B-9H-4 (73-74)	6.342	2.43	0.47	-9.76	-2.38	4.81
A-10H-2 (69-70)	6.770	2.61	0.47	-9.71	-2.34	4.95
C-12H-3 (17-18)	7.300	1.80	0.47	-10.48	-2.94	4.74
B-11H-5 (148-149)	7.807	1.84	0.47	-11.21	-3.51	5.35
C-13H-4 (95-96)	8.000	4.33	0.47	-9.68	-2.32	6.65
C-15H-3 (78-79)	8.647	3.56	0.47	-10.81	-3.20	6.77
B-13H-3 (64-65)	9.538	4.25	0.47	-10.38	-2.87	7.11
B-13H-4 (47-48)	9.758	4.16	0.47	-9.86	-2.46	6.62
B-13H-4 (117-118)	9.914	5.33	0.47	-8.93	-1.74	7.07
B-13H-4 (145-146)	9.977	5.40	0.47	-9.23	-1.97	7.38
C-16H-3 (121-122)	10.564	4.41	0.47	-8.96	-1.76	6.18
C-16H-4 (66-67)	10.777	3.53	0.47	-9.87	-2.47	6.00
C-16H-4 (96-97)	10.889	3.45	0.47	-10.47	-2.94	6.39
B-14H-3 (12-13)	12.883	4.08	0.47	-9.45	-2.14	6.22
B-14H-3 (28-29)	12.911	4.93	0.47	-11.61	-3.83	8.76
B-14H-3 (42-43)	12.936	4.82	0.47	-10.85	-3.24	8.05
B-14H-3 (56-57)	12.961	3.68	0.47	-10.23	-2.75	6.43
B-14H-3 (70-71)	12.985	4.42	0.47	-11.02	-3.36	7.78
B-14H-3 (84-85)	13.013	6.21	0.47	-11.08	-3.41	9.62
B-14H-3 (98-99)	13.042	4.88	0.47	-10.83	-3.22	8.10
B-14H-3 (112-113)	13.062	4.32	0.47	-9.95	-2.53	6.86
B-14H-3 (126-127)	13.078	5.10	0.47			
B-14H-3 (140-141)	13.094	5.22	0.47	-10.23	-2.75	7.97
B-14H-4 (5-6)	13.111	4.41	0.47	-10.98	-3.33	7.74
B-14H-4 (19-20)	13.126	4.66	0.47	-9.97	-2.55	7.21
B-14H-4 (33-34)	13.142	4.12	0.47	-11.65	-3.86	7.98
B-14H-4 (49-50)	13.167	4.45	0.47	-10.61	-3.04	7.49
B-14H-4 (61-62)	13.186	4.45	0.47	-10.77	-3.17	7.63
B-14H-4 (75-76)	13.209	5.24	0.47	-10.30	-2.81	8.05
B-14H-4 (87-88)	13.229	4.40	0.47	-10.22	-2.74	7.14
B-14H-4 (101-102)	13.254	4.98	0.47	-10.01	-2.58	7.56
B-14H-4 (113-114)	13.276	4.57	0.47	-9.11	-1.88	6.45
B-14H-5 (98-99)	13.498	4.18	0.47	-12.12	-4.23	8.41
C-18H-2 (41-42)	13.551	3.44	0.47	-11.96	-4.10	7.54
C-18H-2 (63-64)	13.572	4.51	0.47	-12.87	-4.81	9.32
C-18H-2 (87-88)	13.596	4.16	0.47	-12.26	-4.33	8.49
C-18H-2 (109-110)	13.617	4.21	0.47	-12.83	-4.78	8.99
C-18H-2 (131-132)	13.637	4.42	0.47	-11.60	-3.81	8.23
C-18H-3 (2-3)	13.654	4.28	0.47	-11.27	-3.56	7.84

Table A7 (continued): Hf and Nd isotope results for selected samples across all intervals (15.8-5 Ma). The ε_{Hf} (clay array) was calculated after Bayon et al. (2016) using ε_{Hf} (clay array) = 0.78 × εNd + 5.23.

Sample	Age (Ma)	ε_{Hf}	2σ	ε_{Nd}	ε_{Hf} (clay array)	$\Delta\varepsilon_{Hf\ clay}$
C-18H-3 (24-25)	13.671	4.93	0.47	-12.33	-4.38	9.32
C-18H-3 (46-47)	13.688	4.07	0.47	-13.32	-5.16	9.22
C-18H-3 (90-91)	13.720	3.37	0.47	-10.03	-2.59	5.96
C-18H-3 (112-113)	13.732	5.51	0.47	-11.85	-4.01	9.52
C-18H-3 (134-135)	13.744	4.71	0.47	-11.25	-3.54	8.25
C-18H-4 (9-10)	13.757	3.42	0.47	-10.67	-3.09	6.51
C-18H-4 (31-32)	13.768	3.69	0.47	-10.03	-2.59	6.28
B-15H-1 (63-64)	13.780	5.00	0.47	-12.10	-4.21	9.20
B-15H-1 (85-86)	13.792	4.27	0.47	-11.37	-3.64	7.91
B-15H-1 (93-94)	13.796	3.03	0.47	-10.29	-2.80	5.83
B-15H-1 (107-108)	13.803	5.32	0.47	-12.42	-4.46	9.78
B-15H-1 (113-114)	13.807	4.16	0.47	-11.55	-3.78	7.94
B-15H-1 (137-138)	13.819	4.11	0.47	-12.21	-4.29	8.40
B-15H-1 (143-144)	13.822	4.34	0.47	-11.63	-3.84	8.19
B-15H-3 (21-22)	13.850	4.18	0.47	-12.03	-4.15	8.34
B-15H-3 (69-70)	13.906	3.99	0.47	-12.18	-4.27	8.26
B-15H-3 (105-106)	14.000	4.71	0.47	-12.46	-4.49	9.20
C-19H-3 (45-46)	15.298	4.01	0.47	-10.66	-3.09	7.09
C-19H-3 (53-54)	15.319	3.53	0.47	-11.08	-3.42	6.95
C-19H-3 (57-58)	15.330	3.83	0.47	-10.43	-2.91	6.74
C-19H-3 (69-70)	15.362	3.72	0.47	-9.35	-2.06	5.78
C-19H-3 (81-82)	15.393	4.20	0.47	-10.60	-3.04	7.24
C-19H-3 (93-94)	15.425	4.33	0.47	-11.34	-3.61	7.95
C-19H-3 (105-106)	15.457	5.09	0.47	-8.64	-1.51	6.59
C-19H-3 (109-110)	15.467	4.75	0.47	-11.22	-3.52	8.27
C-19H-3 (117-118)	15.488	4.19	0.47	-9.20	-1.95	6.14
C-19H-3 (129-130)	15.520	5.76	0.47	-9.59	-2.25	8.01
B-16H-1 (147-148)	15.552	4.61	0.47	-9.41	-2.11	6.72
B-16H-2 (17-18)	15.604	5.78	0.47	-8.98	-1.77	7.56
B-16H-2 (29-30)	15.643	4.53	0.47	-9.97	-2.55	7.08
B-16H-2 (37-38)	15.669	4.21	0.47	-9.37	-2.08	6.29
B-16H-2 (77-78)	15.802	4.23	0.47	-12.31	-4.38	8.61